PALACKÝ UNIVERSITY OLOMOUC

DOCTORAL THESIS

Distance measurements with mode-filtered frequency comb and analysis of fluorescence from trapped ion at modulated dark state

Author:
Mgr. Adam LEŠUNDÁK

Supervisor:
Ing. Ondřej ČÍP, Ph.D.

A thesis submitted in fulfillment of the requirements for the degree of Doctor of Philosophy

in the

Department of Optics
&
Institute of Scientific Instruments of the CAS

Olomouc, May 6, 2019

Declaration of Authorship

I, Mgr. Adam LEŠUNDÁK, declare that this thesis titled, "Distance measurements with mode-filtered frequency comb and analysis of fluorescence from trapped ion at modulated dark state" is entirely my own work. I confirm that:

- Where any part of this thesis has previously been submitted for a degree or any other qualification, this has been clearly stated.
- Where I have quoted from the work of others, the source is always given.
- I have acknowledged all main sources of help.

Signed: _____

Date: _____

"Imagination is the power of creation."

Anonymous scientist

PALACKÝ UNIVERSITY OLOMOUC

Abstract

Faculty of Science
&
Institute of Scientific Instruments of the CAS

Doctor of Philosophy

Distance measurements with mode-filtered frequency comb and analysis of fluorescence from trapped ion at modulated dark state

by Mgr. Adam LEŠUNDÁK

This thesis deals with applications of an optical frequency comb to two fields of fundamental metrology: distance measurements and optical frequency measurements. The first part of the thesis presents homodyne interferometry with a mode filtered frequency comb as a powerful method to measure long distances with high accuracy and absolute scale. The measurement principle requires that individual comb modes are spectrally resolved. For this reason the method cannot be applied directly to frequency combs with a low repetition rate (e.g. 100 MHz), since the modes are too close to each other to be resolved. Cavity mode filtering is used to increase the pulse repetition rate of a comb and the filtered comb is applied for mode-resolved absolute distance measurement. Mode-filtering takes place with a single Fabry-Pérot cavity in a Vernier configuration, allowing to set mode spacing ranging from tens of GHz to more than 100 GHz. It is demonstrated that large mode-spacing significantly reduce the requirements on the resolution of the spectrometer and enables absolute distance measurement with a mode-filtered frequency comb using a simple array spectrometer for detection. Here a 1 GHz comb is used, that is converted into a 56 GHz comb by mode-filtering. It is shown that in comparison to a conventional counting interferometer an agreement within 0.5 μm for distances up to 50 m is found. The second part of this thesis presents an original method using a single trapped $^{40}Ca^{+}$ ion as convertor from optical frequency domain to fluorescence intensity for optical frequency analysis of lasers interacting with the ion. It is based on analysis of fluorescence emitted from the ion at a dark state excited by two laser fields with modulated mutual frequency detuning. The response of detected photon rate to relative laser frequency deviations is recorded within the slope of a dark resonance formed in the lambda-like energy level structure corresponding to two optical dipole transitions. Both employed lasers are phase locked to an optical frequency comb, which allows precise calibration of the method by deterministic modulation of the frequency modulated laser beam with respect to the beam with fixed optical frequency. Measured fluorescence responses are evaluated using the Fourier analysis and the results are compared with theoretical model for achievable signal-to-noise ratios in a range of modulation frequencies and amplitudes. The results shows the limits of this method in terms attainable modulation frequencies and detectable laser frequency deviations.

Acknowledgements

Many people stands behind the experiments presented in this thesis. Without their help and cooperation non of the results would be possible to achieve. My thanks goes to all of them and in special I thank my supervisor Ondřej Číp for giving my the opportunity to work on such extraordinary projects.

Also many thanks goes to Lukáš Slodička who was the main driving force and source of knowledge in the realization of the ion experimental setup and to Minh Tuan Pham, Peter Obšil and Martin Čížek for their scrupulous and consistent work on the preparation of the vacuum apparatus, ion trap and all the electronics.

Furthermore, I thank Steven van den Berg who has given me the chance to do my research at VSL and also Sjoerd van Eldik and Dirk Voigt for their endeavor on setting up the distance measurement interferometer and the spectrometers.

Finally, I am very grateful for generous support of my charming fiancée Petra Pokorná. I thank Petra for her encouragement, patience, strength and genuine love.

Contents

Declaration of Authorship i

Abstract iii

1 Introduction 1
1.1 Distance measurements with mode-filtered comb . . . 1
1.2 Fluorescence analysis . . . 2

2 Optical frequency comb 4
2.1 Principle of optical frequency comb . . . 4
2.1.1 Types of frequency comb lasers . . . 6

I Long Distance Measurements with Mode Filtered Frequency Comb 9

3 Measurement principles 10
3.1 Interferometric distance measurements . . . 10
3.1.1 Homodyne interferometry . . . 11
3.1.2 Multiple wavelength interferometry . . . 11
3.1.3 Spectral interferometry . . . 12
3.2 Spectral analysis . . . 14
3.2.1 Diffraction grating spectrometer . . . 14
3.2.2 VIPA spectrometer . . . 15

4 Cavity filtering of frequency comb modes 18
4.1 Filtration cavity design . . . 18
4.1.1 Fabry Perot cavity . . . 18
4.1.2 Cavity comb interaction . . . 20
4.2 Frequency comb mode filtering . . . 23

5 Experimental setup for distance measurements 25
5.1 Filter cavity setup . . . 26
5.1.1 Cavity mirrors . . . 26
5.1.2 Cavity mode matching . . . 27
5.1.3 Cavity-comb locking . . . 29
5.2 Interferometer and spectrometer . . . 31
5.2.1 Interferometer . . . 31
5.2.2 Spectrometers . . . 33

6 Measurements 35
6.1 Cavity filtration performance . . . 35
6.1.1 Filtered comb VIPA spectra . . . 36
6.1.2 Locking performance . . . 37
6.2 Distance measurements . . . 39

6.2.1 Cavity setting . . . 39
6.2.2 Measurement procedure . . . 39
6.2.3 Results . . . 40

7 All fiber filter cavity approach 43
7.1 Fiber cavity design . . . 43
7.1.1 Optical design . . . 44
7.1.2 Electro-mechanical design . . . 45
7.2 Results . . . 46

II Analysis of fluorescence from single trapped ion at frequency modulated dark state 47

8 Ion trapping and interaction of an ion with external fields 48
8.1 $^{40}Ca^{+}$ ion and its interaction with external fields . . . 48
8.1.1 Zeeman splitting and dark resonances . . . 52
8.2 Ion trapping with Paul trap . . . 53
8.3 Ion cooling . . . 55

9 Ion experimental setup 56
9.1 Vacuum apparatus with linear Paul trap . . . 56
9.1.1 Ion fluorescence detection . . . 57
9.2 Laser setup . . . 58

10 Analysis of fluorescence of ion at modulated dark state 62
10.1 Features of the measurements . . . 62
10.1.1 Measurement configuration . . . 62
10.1.2 Fluorescence spectra with phase locked ECDLs . . . 63
10.1.3 Fluorescence signal-to-noise ratio . . . 65
10.2 Measurements of fluorescence response . . . 67
10.2.1 Modulation frequency . . . 68
10.2.2 Frequency deviation . . . 68
10.2.3 Measurement time . . . 69
10.2.4 Measurement point . . . 70
10.3 Results and discussion . . . 71

11 Conclusion 73

A Distance measurement data 75

References 77

List of Figures

2.1 Time and frequency representation of frequency comb 5
2.2 Ti:Sapphire optical frequency comb laser 6
2.3 Ti:Sapphire laser cavity – scheme 7
2.4 Fiber frequency comb cavity – scheme 8
2.5 Fiber frequency comb laser units 8

3.1 Michelson interferometer – scheme 10
3.2 Diffraction grating spectrometer – scheme 14
3.3 VIPA spectrometer – scheme 15
3.4 Vipa etalon – scheme 16

4.1 Cavity transmission 19
4.2 Cavity transmission of the frequency comb 21
4.3 Origin of transmission lateral peaks 22
4.4 Cavity transmission as function of length 22
4.5 Mode filtration by cavity 23
4.6 Vernier mode filtration by cavity 23
4.7 Frequency comb mode suppression 24

5.1 Scheme of experimental setup for distance measurements 25
5.2 Cavity mirror properties 26
5.3 Filter cavity – scheme 27
5.4 Cavity mirror mounts 27
5.5 Scheme of modematching optics 29
5.6 Cavity transmission - measured 30
5.7 Cavity locking on transmission peak – scheme 30
5.8 Scheme of cavity locking electronics 31
5.9 Michelson interferometer and long bench at VSL 32
5.10 Filter cavity with spectrometers 33

6.1 Scan of the cavity transmission 35
6.2 VIPA spectrum with reference laser 36
6.3 VIPA spectra of the filtered frequency comb 37
6.4 VIPA spectrum for 3 transmission peaks 38
6.5 Cavity locking voltage 38
6.6 Distance measurement interferogram 40
6.7 Distance measurement result 41

7.1 Fiber cavity setup 43
7.2 Fiber cavity transmission – calculated 44
7.3 Fiber cavity patchcords 44
7.4 Fiber cavity reflective coating 45
7.5 Fiber cavity piezo holder – scheme 45
7.6 Fiber cavity transmission – measured 46

7.7 Fiber cavity filtration VIPA spectrum 46

8.1 $^{40}Ca^{+}$ energy level scheme 49
8.2 Zeeman splitted level scheme 52
8.3 Resonance fluorescence spectrum 53
8.4 Paul trap – scheme 54

9.1 Vacuum chamber and detection optics 56
9.2 Ion trapp in the vacuum chamber. 57
9.3 Optical table with ion lasers. 59
9.4 Scheme of phase locking setup and picture of optics 60
9.5 Scheme of ion experimental setup 61

10.1 Dark resonance measurement scheme 63
10.2 Fluorescence spectra with stabilized lasers 64
10.3 Photon count rate 66
10.4 SNR for variable modulation frequency 68
10.5 SNR for variable frequency deviation 69
10.6 SNR for variable measurement time 70
10.7 SNR for variable measurement point 71

Chapter 1

Introduction

Before the beginning of the 20^{th} century light itself was mainly a subject of observation. Newton performed his famous experiment on dispersion while discovering that white light consists of all colors, and interestingly he considered light to be a stream of particles. Later on, measurements of the speed of light and an amazing match of the constant c derived from Maxwell's equations proved electromagnetic-wave nature of light. However, in 1900 Planck solved the problem of the black body radiation by hypothesis that those electro-magnetic waves can be emitted only as quanta of energy. The quantum character of light was proved by Compton when he observed scattering of single photons. During 20^{th} century the properties of light were studied in connection with the light sources. The explanation of spectral lines of natural elements was the first approach to a quantum mechanical description of atoms. Deep understanding of the atomic structure together with earlier discoveries in the field of interferometry and spectroscopy led to the invention of lasers.

Today light in the form of laser fields is used as indispensable tool in wide range of applications. Two of them are presented in this thesis. They both uses the optical frequency comb – form of light consisting of many coherent and tied waves within one optical beam. However, both applications are distinct in their nature and in the field of use, they both profit from the unique properties of the frequency comb laser. The thesis is thus divided into two parts, while a chapter describing frequency comb lasers stands before those parts.

1.1 Distance measurements with mode-filtered comb

In the first part of this thesis the optical frequency comb serves as a light source for optical distance measurements, while its properties are enhanced by a mode filtering optical cavity. This research have been carried out during my stay at Netherlands national metrology institute VSL in Delft as a part of the European Metrology Research Programme (EMRP) project "Metrology for long distance surveying".

In the field of optical distance measurements a frequency comb can serve as a frequency reference to a continuous wave (CW) laser, which is then used as a light source for a displacement measurement. Other indirect methods for absolute distance measurement use the optical beat of two CW lasers, whose phase shift of the synthetic wavelength determines the distance [1, 2]. Many schemes have been developed using the frequency comb itself as a light source for length metrology. One pioneering method was based on the heterodyne beat between longitudinal modes of a mode-locked laser [3]. An approach based on a time of flight of femtosecond pulses

was later proposed [4], followed by several experimental demonstrations of cross-correlation based measurements [5, 6, 7, 8]. Homodyne and heterodyne interferometric schemes utilizing one frequency comb [9, 10] and two frequency combs [11, 12], respectively, have also been demonstrated.

In 2012, Van den Berg established absolute distance measurements with a frequency comb laser, based on homodyne mode-resolved many-wavelength interferometry [10, 13]. The laser illuminates a Michelson interferometer, whose output is then spectrally resolved with a virtually imaged phased array (VIPA) spectrometer. The method allows for accurate measurements with a single frequency comb and a wide range of distance non-ambiguity. However it cannot be directly used with fiber frequency combs, which are better suited for potential field applications because of their ease of operation, robustness and smaller sensitivity to environmental disturbances. The reason for this is their small mode spacing of a few 100 Mhz, which cannot be resolved even with a VIPA spectrometer.

To enable the application of the method for low repetition rate frequency combs and also to enable the use of a simple grating-based spectrometer for detection, cavity mode filtering can be applied to increase the repetition rate of the laser source. The first implementation of external Fabry-Pérot cavity to a frequency comb was used for cavity-enhanced spectroscopy [14]. However, cavity filtering of frequency comb modes found its application soon after in astro-combs for calibration of high-resolution astronomical spectrographs [15, 16, 17]. Experimental work published on this topic describes in details the cavity filtering model with an effect of cavity-comb offset [18], selection of optimal cavity mirrors radius of curvature [19] or cavity dispersion [20].

A cavity mode filtering method, which uses the Vernier effect to enhance its performance, is presented here. The mode filtered comb is then used for 50 m long distance measurements in laboratory conditions and the results are compared with a commercial fringe counting interferometer. The distance measurement principles together with two methods for spectral analysis are explained in chapter 3. Then a theory of frequency comb mode filtering with a free space cavity is introduced in chapter 4. The optical setups for cavity mode filtering and for distance measurement interferometry and spectrometry are described in chapter 5. Measurements of cavity filtration performance and the distance measurements are presented in chapter 6. The last chapter 7 of this part describes an all fiber approach for frequency comb mode filtering, which is being developed at ISI Brno.

1.2 Fluorescence analysis

The second part of this thesis describes measurements carried out at my home Institute of Scientific Instruments of the CAS in Brno. Here a frequency comb is employed as a single optical reference for another lasers utilizing its stable frequency properties. The lasers are then used for interaction with a single calcium ion trapped in a Paul trap. The goal of presented measurements is to characterize ion fluorescence response to laser frequency deviations of two lasers driving appropriate atomic transitions. The ion serves as a convertor of optical frequency detuning of two interrogating lasers to photon fluorescence intensity. This approach is explored as a method of optical frequency analysis of optical fields separated by hundreds of THz, however within limited spectral range. The sensitivity of the fluorescence to

relative frequency detuning of interrogating lasers is enhanced in the vicinity of a dark resonance.

Atoms with lambda-like energy level system are ideal for observations of this phenomenon. In such system destructive interference of amplitudes between two excitation paths from two ground states to an excited state leads to atom fluorescence quenching. Fluorescence spectrum of the atom close to the two-photon resonance is manifested with high photon count rate dependence on the mutual frequency detuning of the two excitation laser fields. These features called dark resonances have been found useful in many applications since their discovery by Alzetta et al. [21]. Various schemes of their use in laser cooling can be found [22, 23, 24, 25]. They can serve as a probe for motional state of single ion [26], or as a thermometer for trapped ions or ultracold atom cloud [27, 28].

To reveal possible applications and limits of the effect of optical two-photon interference with single atom as a tool for frequency metrology, we implemented a continuous measurement scheme on a single Doppler cooled calcium ion $^{40}Ca^{+}$ excited by two lasers at wavelengths 397 nm and 866 nm. The lasers are phase locked to common optical reference – the fiber frequency comb. Properties of the presented scheme are analyzed in terms of the fluorescence response to imposed laser frequency characteristics and measurement time. For this purpose, one of the lasers is frequency modulated, while the other has fixed frequency. Measured fluorescence responses are evaluated using the Fourier analysis and the results are compared with theoretical model for achievable signal-to-noise ratios (SNR) in a range of modulation frequencies and amplitudes. Finally we estimate the limits of the presented method and discuss comparison of measured data with simulations.

This part is divides to tree chapters: Chapter 8 describes interaction of an ion with external fields, ion trapping mechanism and ion laser cooling principles. The experimental setup is described in chapter 9 and the final chapter 10 explains the measurement principles and presents measured results.

Chapter 2

Optical frequency comb

This chapter describes basic principles of optical frequency combs and distinguishes two types of frequency comb lasers, which are used in two experiments presented in this thesis. As such, the chapter stands before two main parts of this thesis, since a frequency comb application in the experiments is a conjunctive element for both parts.

An optical frequency comb (FC) is the spectrum of a laser whose optical modes are phase locked in such way, that they interfere together to form a train of pulses with a repetition rate frequency f_{rep} which directly represents spacing between neighboring modes in the frequency domain [29]. Its development in 1999 [30, 31] caused a revolution in optical metrology. Frequency chains [32] previously used for absolute frequency measurements has been rapidly replaced by much simpler systems based on self-referenced frequency combs capable of covering large spectral ranges of hundreds of terahertz [33]. They provide direct traceability to a stable frequency reference such as a maser or an atomic clock [34]. In the past decades a wide variety of frequency comb applications has emerged, ranging from ultra-fast physics [35, 36], precise spectroscopy [14, 37] and astronomy [16, 38] to length metrology [3, 4].

2.1 Principle of optical frequency comb

Optical output of a frequency comb laser cavity is a train of pulses with a time delay τ. In the time domain, it is described by the time varying electric field

$$E(t) = \sum_m \hat{E}(t - m\tau) e^{i(\omega_c t + m(\Delta_\Phi - \omega_c \tau) + \Phi_0)} \tag{2.1}$$

where $\hat{E}(t)$ is the pulse Gaussian shaped envelope, Φ_0 is a constant phase offset between the pulse envelope and underlying carrier wave. Δ_Φ is the phase shift between two consecutive pulses with respect to the pulse envelope and m is the number of round trips in the cavity. The pulse delay $\tau = l_c / v_g$ is determined by the laser cavity length l_c and the phase shift is the result of difference between phase v_p and group v_g velocities

$$\Delta_\Phi = \left(\frac{1}{v_g} - \frac{1}{v_p} \right) l_c \omega_c \tag{2.2}$$

where ω_c is the center frequency of the comb spectrum [39]. This spectrum can be derived by application of the Fourier transform to the train of pulses

$$E(\omega) = \sum_m e^{i(m(\Delta_\Phi - \omega_c \tau) + \Phi_0)} \int \hat{E}(t - m\tau) e^{-i[(\omega - \omega_c)t]} \mathrm{d}t. \tag{2.3}$$

Using the identity $\int f(x-a)e^{-i\alpha x}\mathrm{d}x = e^{-i\alpha a}\int f(x)e^{-i\alpha x}\mathrm{d}x$ and substitution $\tilde{E}(\omega) = \int \hat{E}(t)e^{i\omega t}\mathrm{d}t$ evaluation of the Fourier integral leads to

$$E(\omega) = e^{i\Phi_0}\sum_m e^{im(\Delta_\Phi - \omega\tau)}\tilde{E}(\omega_c - \omega). \tag{2.4}$$

The therms which are in phase between pulses i.e. for which the phase difference is an integer multiple of 2π, $\Delta_\Phi - \omega\tau = 2\pi n$ will adds in the sum coherently and result in sharp spectral components. This is the mode-locking condition which is required for the formation of ultra-short laser pulse. Rewriting this condition in frequency terms results in the standard equation for the comb mode frequency

$$f_n = nf_{rep} + f_0 \tag{2.5}$$

where $f_n = \omega_n/2\pi$ is frequency of nth mode and $f_{rep} = 1/\tau$ is the repetition rate frequency. The carrier-envelope offset frequency f_0 represents the common phase relationship for all longitudinal laser cavity modes nf_{rep} and defines the phase of the electric field with respect to the pulse envelope. Its result is a spectral shift of all frequency comb modes by the relation

$$f_0 = \frac{\Delta_\Phi}{\tau 2\pi}. \tag{2.6}$$

The time and frequency domain representation of an optical frequency comb is shown in Fig. 2.1.

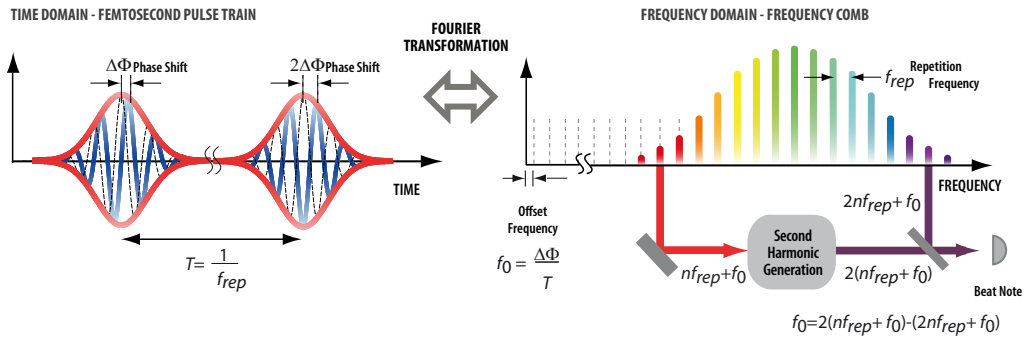

FIGURE 2.1: Time and frequency representation of an optical frequency comb and scheme of the f-to-$2f$ interferometry for f_0 detection [40].

Stabilizing the frequency comb

The beauty of the frequency comb is hidden in equation 2.5, which tells that by stabilizing just two radio-frequencies f_{rep} and f_0 we get accordingly stable and equally spaced n optical frequencies. Before giving any stabilization feedback to the laser cavity, f_{rep} and f_0 needs to be measured. For f_{rep} it is done by a fast photodiode illuminated by small part of the frequency comb laser beam. Measuring f_0 requires a nonlinear self-referencing technique which compares individual comb components to each other. This is done by so-called "f to $2f$ interferometer" [41, 42]. Here an octave spanning comb called supercontinuum is generated by a highly nonlinear optical fiber. Propagation through the fiber broadens the spectrum of the laser by the nonlinear process of self-phase modulation [43, 44]. Then the high-frequency component of the supercontinuum with frequency f_{2n} is compared to the

low-frequency component f_n, using another nonlinear process of second harmonic generation (SHG), which doubles the low frequency to $2f_n$. An optical beat frequency $f_0 = f_{2n} - 2f_n$ is then measured by a fast photodiode as is shown schematically in Fig. 2.1.

2.1.1 Types of frequency comb lasers

There are two common types of optical frequency comb lasers distinct by the type of a laser gain medium and a passive mode locking mechanism. As representative of the first type, the early developed combs were based on titanium doped sapphire crystal (Ti:Sa) in a free space laser cavity. Later on a more robust and much less fragile second type – fiber frequency combs were introduced, where the gain medium is an optical fiber doped with Ytterbium or Erbium [45, 46]. Comb mode spacings are typically from tens to 250 MHz for fiber combs and roughly 80 MHz to 1 GHz for Ti:Sapphire combs. For distance measurements presented in this thesis a Ti:Sapphire comb with $f_{rep} = 1\ GHz$ and emission spectrum in region 810–830 nm is used. In measurements with trapped ions an Erbium doped fiber laser with $f_{rep} = 250\ MHz$ and emmision spectrum around 1560 nm, however frequency doubled and broadened to bandwidth ranging from 600 to 900 nm, has found its application .

Ti:Sapphire frequency comb

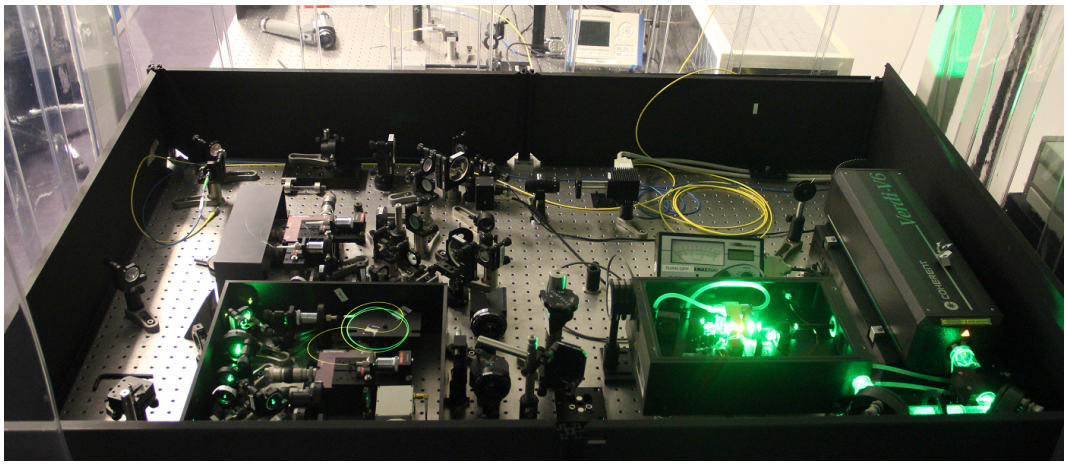

FIGURE 2.2: TiSa comb used for the distance measurements operating around 820 nm. Bright green spot is the laser cavity with pumped Ti:Sa crystal. Glowing optical fiber generates a supercontinuum for f to $2f$ interferometer.

The Ti:Sapphire frequency comb consist of the pump Nd:YAG laser at 532 nm, the laser cavity with Ti:Sapphire crystal and the stabilization unit, see Fig. 2.2. The intensity of the pump light is controlled by diffracting a small amount of light out of the laser cavity input beam with an acousto-optic modulator (AOM). The crystal is placed in a double bow tie cavity where it is pumped by tightly focused green light and its nonlinear index of refraction allows for Kerr lens mode-locked generation of ultrashort pulses [47], see Fig. 2.3. The crystal also introduces normal spectral dispersion, where the long wavelengths travel faster than the short ones, therefore two of the cavity mirrors are chirped mirrors with negative dispersion. The chirped mirrors are formed by a stack of dielectric coatings where the penetration depth of

the light depends on the wavelength thus compensates for the normal dispersion in the cavity [48]. The Kerr-effect causes the change in the refractive index of a material as a function of intensity of the light thus invoking the self-focusing and self-phase modulation. Light with Gaussian profile sent through the crystal results in the formation of an intensity-dependent lens (Kerr lens) in the nonlinear medium and self-focusing of the light. The mode-locked operation with high intensity pulses has a better spatial overlap with the pump beam as compared to the continuous wave (CW) operation, thus pulsed mode is preferred by the cavity over the continuous situation [49]. The temporal effect of a high-intensity laser pulse is a time change in the refractive index leading to a self-phase modulation at the pulse edges, which coherently generates new frequency components and together with the dispersion compensation yields a shorter pulse [50]. The Ti:Sa crystal needs a critical misalignment to advance from continuous to pulsed regime. This is introduced by knocking on one of the cavity mirrors to start mode-locking by the formation of a weak pulse which is then amplified by the nonlinear effect. One of the cavity mirrors is partially transparent an serves as an output coupler. The stabilization of f_{rep} is introduced by a movable cavity mirror mounted on a piezelectric transducer, the f_0 is stabilized by the pump laser intensity control provided by the AOM. The phase shift between the pulses Δ_Φ is also adjusted by a movable prism pair (PP) placed inside the cavity, which introduces an adjustable ratio of v_g/v_p.

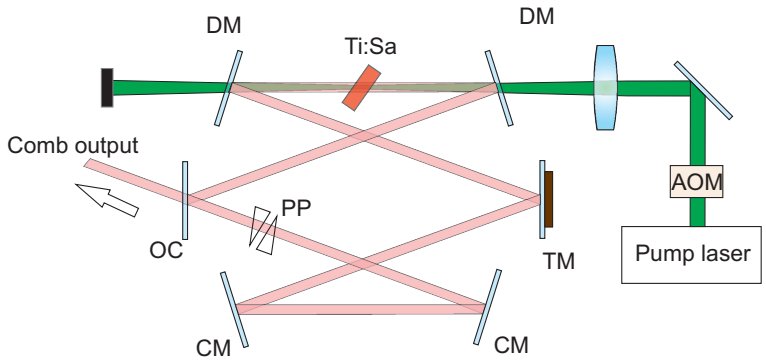

FIGURE 2.3: Scheme of a Ti:Sa laser double bow tie cavity. The repetition rate is adjusted my means of translation mirror (TM). The offset frequency is adjusted by prism pair (PP) and acousto-optic modulator (AOM).

Fiber frequency comb

The Erbium doped fiber frequency comb laser consists of the laser cavity with Er^{+3} doped fiber pumped with diode laser at 980 nm, and the laser amplifier and stabilization units pictured in Fig. 2.5. The laser is mode-locked using a technique called polarization additive pulse mode locking (P-APM) [51, 52]. Er^{+3} doped fiber has a nonlinear index of refraction. The phase shifts of the laser light caused by the optical Kerr effect inside the fiber induces a polarization selective and intensity dependent rotation of the laser polarization. Linearly and circularly polarized light experiences no rotation, only elliptically polarized light experiences the rotation which depends on the intensity and the ellipticity of the beam. Inside the laser cavity are used polarization controllers and polarizing beamsplitter (PBS) to create high intra-cavity loss for CW operation and low loss for pulsed operation.

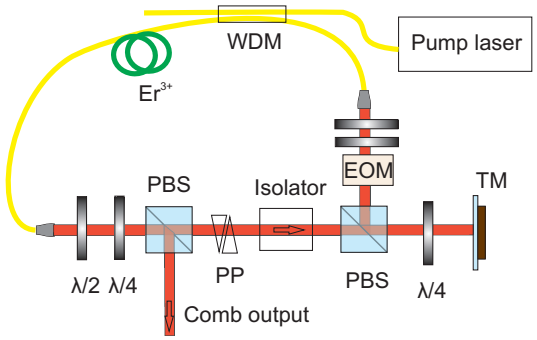

FIGURE 2.4: Scheme of the fiber laser cavity. Pump laser is coupled to the cavity with wavelength division multiplexer (WDM).The repetition rate is adjusted by means of translation mirror (TM) and electro-optic modulator (EOM). The offset frequency is adjusted by prism pair (PP).

A scheme of the fiber comb laser cavity is shown in Figure 2.4. The PBS transmits linearly polarized light incident into the cavity. Quarter and half wave plates changes the linear state of the light to an arbitrary elliptical polarization state. The light then enters the nonlinear fiber where the Kerr effect causes the polarization ellipsis to rotate more for the more intense part of the pulse, than for the weaker edges of the pulse. Correct angle setting of the wave plates with respect to the PBS can ensure that only the intense part of the pulse is rotated in such amount that it can be effectively recoupled into the laser cavity, and the laser will passively mode-locks. The weak parts of the pulse are coupled out of the cavity by the same PBS and are used as the output laser beam. A translation mirror mounted on a piezochip together with an electro-optic modulator (EOM) are used for stabilization of f_{rep} and an intra-cavity prism pair is used for control of the f_0.

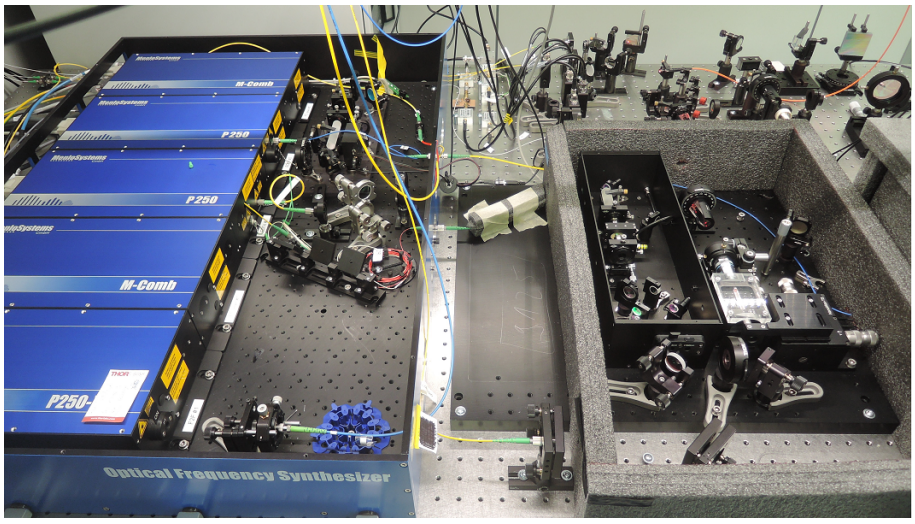

FIGURE 2.5: Two fiber comb units *M-Comb* operating at center wavelength 1550 nm, together with amplifiers and stabilization units with f-to-2f interferometers (on the left side). Only one comb is used for the experiment. Output of the middle *P*250 amplifier unit is free-space coupled into the setup on the right side, where a supercontinuum centered at 780 nm is generated.

Part I

Long Distance Measurements with Mode Filtered Frequency Comb

Chapter 3

Measurement principles

3.1 Interferometric distance measurements

Optical interferometry is used in the field of distance measurements in many ways. Generally, they are based on the principle of superposition of electromagnetic waves. Usually measurement waves are added to reference waves resulting in the sum of all contributing waves with phase information about measured distance. To obtain this kind of information, interferometers of many types can be used. The most common interferometer is the Michelson interferometer. Its simple schematic diaga is shown with use of a non-polarizing (BS) and a polarizing beam splitter (PBS) in Fig. 3.1.

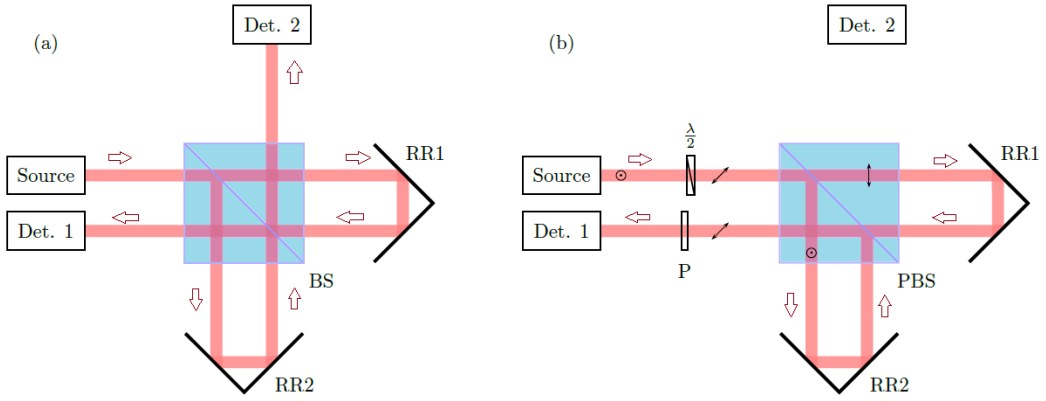

FIGURE 3.1: Scheme of two Michelson interferometers with non-polarizing beamsplitter BS – left , with polarizing beam splitter PBS – right. Polarization planes are signed as p – arrow and s – point.

For the first case, a coherent light source emits light towards the BS, which divides the light into the measurement and reference beams. Each beam travels into one arm of the interferometer and towards a retroreflector where it is reflected back. The reference arm has a fixed position and the measurement arm can be moved to a requisite position. The beams are recombined at the BS and split again towards detectors 1 and 2. Both detectors measures identical signals. In the second case, the source emits s-polarized light, which is rotated by 45° in a half-wave plate before it hits the PBS. Here equal decomposition to p-polarized and s-polarized beams is done by the PBS transmitting only the p and reflecting the s part. This also holds for reflected beams and results in sending the recombined beam only towards detector 1. Because orthogonal polarizations do not interfere a polarizer is placed right

before the detector. Both type of interferometers are used in the experiment, however the polarization one is only used with a commercial helium–neon (He-Ne) laser based system for a comparison distance measurement method. Further explanations are thus made using the interferometer in Figure 3.1*a*) and only one detector.

3.1.1 Homodyne interferometry

In homodyne interferometry both the measurement and reference arm uses the same wavelength. Lets suppose that there is a light source emitting coherent wave

$$E(r,t) = 2E_0 e^{-i(\omega t - 2\mathbf{k}\cdot\mathbf{r} + \Phi_0)}, \tag{3.1}$$

where E_0 is one half of the initial amplitude, $\mathbf{k}$ is the wavevector, ω is the angular frequency and Φ_0 is the initial phase. Factor 2 multiplying the position vector $\mathbf{r}$ is convenient for beam traveling the same distance twice. Now the laser beam enters the interferometer, where it is split into two beams and after traveling back and forth in the corresponding arms, they are recombined. The beams have traveled different paths according to the length of the interferometer arm, leading to two beams in the same optical path after the recombination

$$\begin{aligned} E_{meas}(l_{meas},t) &= 2E_0 e^{-i(\omega t - 2kl_{meas} + \Phi_0)} \\ E_{ref}(l_{ref},t) &= 2E_0 e^{-i(\omega t - 2kl_{ref} + \Phi_0)}. \end{aligned} \tag{3.2}$$

The propagation can be considered as one dimensional. This simplifies the wavevector $\mathbf{k}$ to the wavenumber $k = 2\pi/\lambda$ and instead of the position vector $\mathbf{r}$ we can write the distances, l_{meas} and l_{ref} propagated by each beam in one direction. The optical path difference L between the measurement and reference arms $L = l_{meas} - l_{ref}$ is the distance to be measured. Intensity of the interfering beams measured by the detector is

$$I(L) = \left|E_{meas} + E_{ref}\right|^2 = 2\left|E_0\right|^2 (1 + \cos(\Phi)) \tag{3.3}$$

where

$$\Phi = 2k(l_{meas} - l_{ref}) = 2kL. \tag{3.4}$$

The intensity depends only on the relative phase or the optical path difference. The interference pattern repeats itself every distance corresponding to a multiple of $\lambda/2$, which is the range of non-ambiguity for homodyne measurements. When distances longer than the range of non-ambiguity needs to be measured, common way is to do the incremental measurement. The measurement arm is moved from zero or l_{ref} to the measurement position l_{meas} while number of interference fringes is counted. Due to the nanometer scale of visible light wavelengths, this type of measurements is not convenient for long distance measurements. On the other hand it is useful in applications where precision in the sub–*nm* range is required, such as precise control of optical surfaces or as in the ultimate case of interferometry for gravitational waves detection [53].

3.1.2 Multiple wavelength interferometry

The non-ambiguity range can be greatly enhanced by interferometry with many waves with different wavelengths [54]. Considering the most simple case of light

fields with two wavelengths λ_1 and λ_2, we have

$$\begin{aligned} E_1(l_1,t) &= 2E_1 e^{-i(\omega_1 t - 2k_1 l + \Phi_1)} \\ E_2(l_2,t) &= 2E_2 e^{-i(\omega_2 t - 2k_2 l + \Phi_2)}. \end{aligned} \tag{3.5}$$

By letting the both beams E_1 and E_2 to enter the interferometer and to propagate through the measurement and reference arm as described above, the signal at the detector consists of four waves

$$\begin{aligned} I =& \left\langle \left| E_{1,meas} + E_{1,ref} + E_{2,meas} + E_{1,ref} \right|^2 \right\rangle \\ =& 2\left|E_1\right|^2 (1+\cos(\Phi_1)) + 2\left|E_2\right|^2 (1+\cos(\Phi_2)). \end{aligned} \tag{3.6}$$

where the time average $\langle\rangle$ leads to zero for all cross terms containing both wavelengths $|E_1 E_2|$ and the phases for remaining terms are $\Phi_1 = 2k_1 L$ and $\Phi_2 = 2k_2 L$. Assuming that amplitudes for both waves are equal $|E_1| = |E_2| = |E|$ and using $\cos(a) + cos(b) = 2\cos\left(\frac{a+b}{2}\right)\cos\left(\frac{a-b}{2}\right)$, equation 3.6 can be written as

$$I(L) = 4\left|E\right|^2 \left[1 + \cos\left(L\frac{k_1+k_2}{2}\right)\cos\left(L\frac{k_1-k_2}{2}\right)\right]. \tag{3.7}$$

This result shows that the intensity now depends on two synthetic wavelengths

$$\frac{k_1 \pm k_2}{2} = \frac{2\pi}{2}\left(\frac{1}{\lambda_1} \pm \frac{1}{\lambda_1}\right) = \frac{2\pi}{\lambda_{S\pm}} \tag{3.8}$$

$$\lambda_{S\pm} = 2\frac{\lambda_1 \lambda_2}{\lambda_1 \pm \lambda_2}. \tag{3.9}$$

Supposing that the initial wavelengths λ_1 and λ_2 are close to each other, then the synthetic wavelengths are $\lambda_{S+} \approx \lambda_{1,2} \ll \lambda_{S-}$. The intensity is thus sensitive to the long synthetic wavelength rather then to the optical ones and the non-ambiguity range is hence increased to $\lambda_{S-}/2$.

The non-ambiguity range can be further increased by utilizing even more wavelengths [55]. Adding more optical wavelengths interestingly still results to one longest synthetic wavelength, since each pair of newly created synthetic waves will produce another longer synthetic wavelength and so on, until there is the only one. Obtaining a distance from longer synthetic wavelengths is always less accurate, then from the shorter ones, simply because there is smaller sensitivity to the phase change. A solution to this problem is to determine roughly the distance with a longer synthetic wavelength and then step down and determine it more accurately with a shorter wavelength. The intensity of light consisting of n different wavelengths passing through the interferometer is then

$$I(L) = 2\sum_n \left|E_n\right|^2 \left[1 + \cos(\Phi_n)\right]. \tag{3.10}$$

3.1.3 Spectral interferometry

The principle of distance measurements presented in this thesis is based on spectral interferometry, which is a parallel homodyne interferometry with many spectrally resolved wavelengths [56]. A frequency comb with a multiplied repetition rate mf_{rep} is used as a light source. The multiplication factor m originates from a frequency

comb mode filtering, as will be explained in the next chapter. The distance is obtained from frequency dependent phase change of an interference signal, recorded by a spectrometer, that has distance-unique shape in the non-ambiguity range. The interference written as a function of the laser optical frequency f for a measurement of the distance L is

$$I(f) = 2\left|E_0\right|^2\left[1+\cos\left(\frac{2\pi\cdot 2L\cdot n_r\cdot f}{c}\right)\right]. \tag{3.11}$$

The accumulated phase difference Φ between the interferometer arms for one optical frequency can be expressed as

$$\Phi = \frac{4\pi L n_r}{c} f. \tag{3.12}$$

where n_r is the refractive index of the medium and c is the speed of light. To employ the advantage of many optical frequencies in acquiring the distance, we can utilize the phase change as a function of frequency with the group refractive index $n_g = n_r + f\frac{dn_r}{df}$

$$\frac{d\Phi}{df} = \frac{4\pi L}{c}\left[n_r + f\frac{dn_r}{df}\right] = \frac{4\pi L}{c} n_g. \tag{3.13}$$

The distance L can be thus expressed as

$$L = \frac{d\Phi}{df}\frac{c}{4\pi n_g}. \tag{3.14}$$

In practice, the information about the phase change with frequency $d\Phi/df$ is obtained from the measured spectrum $I(f)$ by a cosine fit with $\Phi = C\cdot p + C_2$. In this equation C and C_2 are fitting parameters and p is a comb mode label associated to comb mode frequency $f_p = mf_{rep}(Q+p) + f_0$, where Q is a large integer number. The distance L can be then expressed as

$$L = \frac{C}{mf_{rep}}\frac{c}{4\pi n_g}. \tag{3.15}$$

Since the frequency comb is a periodic pulse train repeating itself with a pulse to pulse distance L_{pp}, the interference patterns will also repeat themselves with half the distance

$$\frac{L_{pp}}{2} = \frac{c}{mf_{rep}n_g}. \tag{3.16}$$

The distance L is defined in a range of non-ambiguity $-\frac{1}{2}L_{pp} < L < \frac{1}{2}L_{pp}$. Note that the L_{pp} corresponds to a many-wavelength case of the synthetic wavelength defined in Eq. (3.9). Since the sign of L cannot by determined from the cosine fit, it is necessary to obtain it otherwise. One method is based on observing interference fringe density with change of measurement arm length. When the length is increasing, increasing fringe density is equivalent to positive L, decreasing fringe density corresponds to negative L. When pulses from both interferometer arms are overlapping, all comb modes interfere constructively – there is no fringe and L equals zero. This holds for distances

$$L_t = \frac{1}{2}jL_{pp}, \tag{3.17}$$

where j is an integer and L_t is total single path length difference of both arms. Integer j has to be obtained by approximate distance measurement. This can be done by any

method with accuracy better then $L_{pp}/2$. Then a random distance is given by

$$L_t = \frac{1}{2} j L_{pp} + L. \tag{3.18}$$

3.2 Spectral analysis

To perform long distance measurements using the spectral interferometry, all optical waves has to share common optical path in the Michelson interferometer. After they leave it with acquired phase information, they need to be spatially separated for the intensity measurements. This was already performed with a spectrometer based on VIPA etalon and the Ti:Sa frequency comb as the light source [13]. However, in the case of a mode-filtered frequency comb, the waves can be analyzed with much simpler spectrometer based on a diffraction grating. A short description is given for both spectrometer types. The grating based one is used for the distance measurements and the VIPA based is used for measurements of filtering performances of a free space cavity utilized in the distance measurements and also of a fiber cavity, which is explored as an alternative mode-filtering approach.

3.2.1 Diffraction grating spectrometer

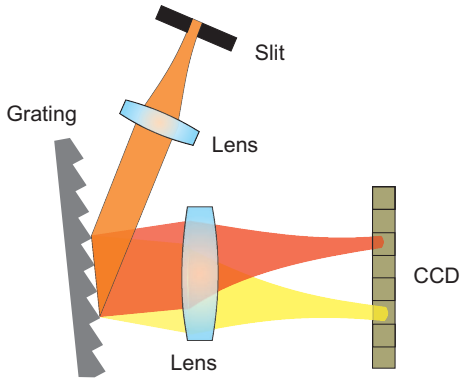

FIGURE 3.2: Scheme of a diffraction grating spectrometer. Laser source is through the slit and lens collimated on the grating where it is dispersed and then refocused on the CCD array.

A reflective diffraction grating is an optical element with a periodic structure of N reflective slits spaced by distance d. Typical setup consists of a slit from which the light is collimated by an input lens onto the grating where the light is angularly dispersed and focused by an output lens onto a linear array camera as shown in Figure 3.2. The relation between incident light angle α, output angle β and light wavelength λ is given by the diffraction equation

$$\sin\beta = \sin\alpha + m\frac{\lambda}{d}, \tag{3.19}$$

where $m = 0, 1, 2, 3, ...$ is the diffraction order. The resolution of the grating spectrometer is determined by three factors [57]. The first is the limit of diffraction grating itself, which is determined by the total number N of diffraction grooves or reflective

slits

$$\frac{\lambda}{d\lambda} = N \cdot m. \tag{3.20}$$

The larger amount of diffraction grooves is illuminated, the better resolution can be obtained, since more reflecting elements constructively contributes to the resulting diffraction. The focusing lens of the spectrometer contributes to its resolution by lateral dispersion. It is a measure of lateral dispersion for different wavelengths in the focal plane of the lens with focal length f,

$$\frac{d\lambda}{dy} = d \cdot \frac{\cos\beta}{f}, \tag{3.21}$$

where dy can be in practice replaced by length of one pixel on the line camera. The same equation holds also for the resolution contribution from the input slit size, which determines the bandwidth of a single input wavelength. The spectrometer can then resolve only frequencies which difference is greater than the bandwidth. In this case dy corresponds to the slit size and f to the focal length of the input lens. The total resolution of the spectrometer is then

$$\delta\lambda = \sqrt{\delta\lambda^2_{grating} + \delta\lambda^2_{camera} + \delta\lambda^2_{slit}}. \tag{3.22}$$

3.2.2 VIPA spectrometer

A high resolution VIPA spectrometer is based on a VIPA etalon [58]. It is an angular dispersive element with a high resolution but relatively small free spectral range (FSR), which results in an overlap of orders of transmission in the output dispersed spectrum [59, 60, 61]. To separate the overlapped parts of the spectrum, a low-resolution high-FSR element such us the diffraction grating, is used to disperse the spectrum perpendicularly to the VIPA dispersion direction. The resulting 2D angular displacement is then imaged with a lens onto a camera as is shown in Fig. 3.3.

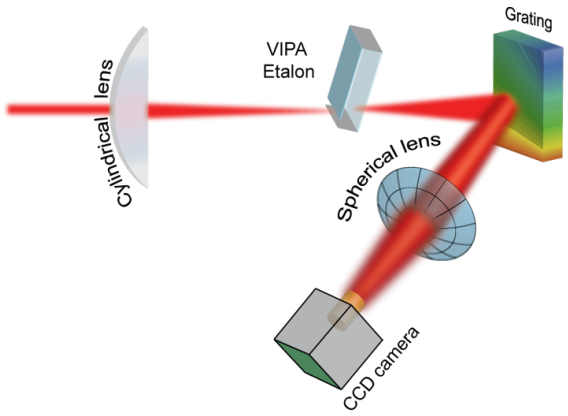

FIGURE 3.3: Scheme of VIPA spectrometer consisting of cylindrical lens, VIPA etalon, diffraction grating, imaging lens and CCD camera [10].

The VIPA etalon is a thin glass plate with a reflectivity $R_1 \approx 100\%$ reflective entrance side, with a small window left uncoated for the incoming light. The light is with a cylindrical lens focused through the window onto the output side of the etalon, see

Fig. 3.4. The output side is covered with a high reflective coating having the reflectivity $R_2 \approx 99\%$. The angle of incidence on the entrance side θ_i is about few degrees with respect to VIPA normal. The small angle causes that the light bounces back and forth up the etalon. The transmitted light appears to originate from a set of virtual sources along the VIPA normal. The line generated by the set of phased-array sources extends the VIPA etalon. The interference of these sources, due to the phase difference at the output, forms collimated beams with wavelength dependent output angles, .

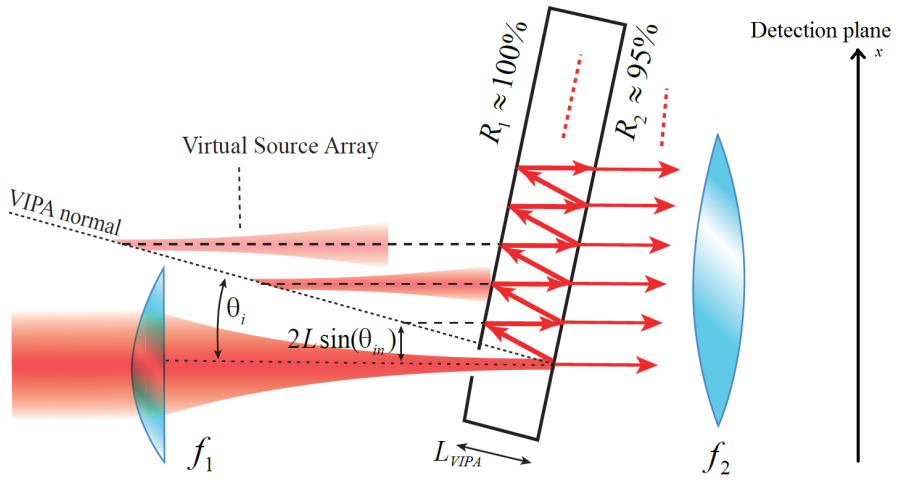

FIGURE 3.4: An overview of light propagation through VIPA etalon [62].

The spatial dispersion of the VIPA etalon at the detection plane can be described by

$$\frac{\delta\lambda}{\delta x} = -\frac{2L_{VIPA}}{mf_2}\left[\tan\theta_{in}\cos\theta_i + \frac{x}{n_{in}f_2}\cos\theta_{in}\right], \tag{3.23}$$

where n_{in} is the index of refraction, θ_{in} is the propagation angle inside the VIPA, f_2 is the focal length of the output lens and m is the mode order of the VIPA transmission

$$m \approx \frac{2L_{VIPA}n_{in}}{\lambda_{central}}\cos\theta_{in}. \tag{3.24}$$

Each mode order of the etalon covers a frequency range that is equal to the free spectral range FSR of the etalon

$$FSR = \frac{c}{2L_{VIPA}}\left[\frac{n_{in}}{\cos\theta_{in}} - \tan\theta_{in}\sin(\theta_i + \theta_{out})\right]^{-1}, \tag{3.25}$$

where θ_{out} is the output angle from the etalon defined as $\theta_{out} = 0°$ if the output direction is the same as the input direction. The VIPA spectrometer is able to disperse an optical spectrum if the VIPA etalon is paired with a diffraction grating whose resolving power is better than the FSR of the etalon. The spectral resolution of the VIPA spectrometer, defined as double the frequency interval between two positions at the detection plane corresponding to intensities I_{max} and $I_{max}/2$, can be approximated by

$$\delta\nu \approx \frac{c(1-R_1R_2)}{2\pi L_{VIPA}n_{in}\cos\theta_{in}\sqrt{R_1R_2}}. \tag{3.26}$$

A more detialed description of the VIPA spectrometer theory and design concepts can be found in [63, 64].

Chapter 4

Cavity filtering of frequency comb modes

Distance measurement based on the homodyne mode-resolved many-wavelength interferometry allows for accurate measurements with a single frequency comb and a wide range of non-ambiguity. This method uses an optical frequency comb as a many-wavelength laser source. The laser illuminates the Michelson interferometer, whose output is then spectrally resolved to individual comb modes. The comb mode spacing is given by a laser cavity length and typical values are a few hundred MHz for fiber combs and roughly 80 MHz to 1 GHz for Ti:Sapphire combs. To resolve the individual comb modes a high resolution VIPA spectrometer has been used [10, 13]. However, its resolution is still insufficient to resolve mode-spacings of a few 100 MHz. Thus the method can not be easily exploited by the commonly used fiber combs, which are better suited for potential field applications (e.g. geodesy and surveying) because of their ease of operation, robustness and smaller sensitivity to environmental disturbances.

To enable the application of the mode-resolved method for low repetition rate combs, cavity mode filtering is theoretically explored in this chapter, in order to increase the repetition rate of the frequency comb laser [65]. The mode filtering overcomes the limitation of the low repetition rate comb sources and also enables the use of a simple grating-based spectrometer for detection, instead of the rather complex VIPA spectrometer. The first section of this chapter describes properties of a symmetrical Fabry-Pérot cavity and its interaction with an optical frequency comb. The second section describes an unique cavity configuration at a non-integer filter ratio, which allows for achieving large range of filter ratios with only minor adjustment of the cavity length.

4.1 Filtration cavity design

This section describes ideal properties of a free space optical cavity consisting of two dielectric mirrors and its interaction with an optical frequency comb.

4.1.1 Fabry Perot cavity

High reflectivity mirrors are essential for sufficient spectral filtering. Dielectric mirrors, constructed from dielectric materials with alternating layers of high n_h and low n_l index of refraction, offer a very high reflectivity over a reasonable bandwidth with a negligible absorption and scattering losses. The ratio n_h/n_l determines the spectral bandwidth of the mirror reflectivity, larger ratios leads to broader spectral bandwidths. Such mirrors are also called quarter-wave stack reflectors since the optical thickness of the dielectric layers is $1/4$ of the wavelength that has to be reflected.

The reflectivity R defines the most general parameter for sufficient suppression of unwanted comb modes – the cavity finesse.

To develop the theory of cavity transmission and consequently cavity-comb interaction we start with approach of two plane mirrors separated by distance L interacting with one comb mode or continuous wave (CW) [57]. The incident electric field is

$$E_{in} = E_0 e^{i\omega t} \tag{4.1}$$

where E_0 is the incidence amplitude. Next we approximate no mirror loss, thus sum of reflectivity $R = r^2$ and transmissivity $T = t^2$ equals one $T + R = 1$. The field transmitted by the first mirror $E_1 = tE_0 e^{i\omega t}$ will undergo two reflection before it travels in the same direction again $E_2 = tr^2 E_0 e^{i\omega t}$ and so on up till the n^{th} field inside the cavity $E_n = tr^{2n} E_0 e^{i\omega t}$. All the fields inside cavity form a geometric series which can be summed to

$$E_{inside} = E_0 e^{i\omega t} \left[\frac{t}{1 - r^2 e^{-i\phi}} \right] \tag{4.2}$$

where $\phi = 2L\omega/c$ is the phase accumulated on each round trip. The electric field transmitted through the cavity is then

$$E_t = te^{i\omega t} E_{inside}. \tag{4.3}$$

The cavity transmission function defined as the ratio of transmitted and incident intensities can be after some algebra written as

$$T(\omega, R, L) = \frac{(1-R)^2}{(1-R)^2 + 4R\sin^2(L\omega/c)} = \frac{1}{1 + \mathbf{F}\sin^2(\phi/2)} \tag{4.4}$$

where the coefficient of finesse $\mathbf{F}$ gathers the reflectivity part of the equation, $\mathbf{F} = 4R/(1-R)^2$. Scanning the frequency of incident light leads to series of transmission peaks with linewidth $\Delta\nu$. The peaks correspond to cavity longitudinal modes, for which the number of light field oscillations within the cavity optical path is an integer. Their linewidth is reciprocal to $\mathbf{F}$ and their number is limited only by the reflectivity bandwidth of the mirrors. The frequency spacing between two adjacent transmission peaks is known as the free spectral range

$$FSR = \frac{c}{2L}. \tag{4.5}$$

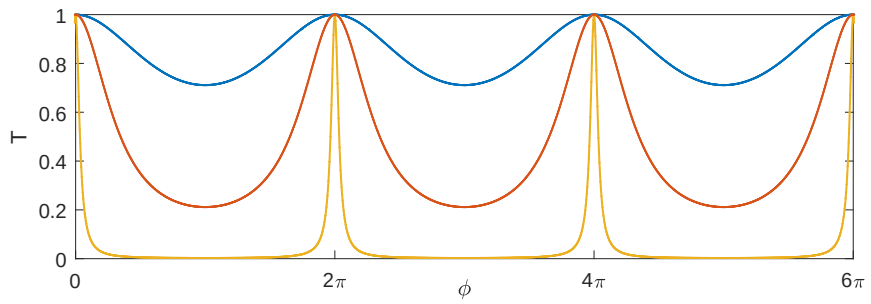

FIGURE 4.1: The cavity transmission as a function of the phase ϕ for 3 values of the finesse F= 1, 3, 30 (blue, red, yellow).

The most common measure of the cavity performance is the ratio of the cavity mode spacing to the cavity mode linewidth known as the finesse

$$F = \frac{FSR}{\Delta\nu} = \frac{\pi\sqrt{R}}{1-R}. \tag{4.6}$$

It also corresponds to maximal achievable cavity filtering ratio $2m$ for which all unwanted comb modes are suppressed at least by $1/2$. In practice $1/2$ suppression is not sufficient, but it is a nice analogy of cavity performance. The cavity transmission as a function of phase ϕ for 3 values of finesse is plotted in Fig. 4.1. Note that the same transmission pattern will appear either by scanning the cavity length or the laser frequency.

4.1.2 Cavity comb interaction

To describe the behavior of a frequency comb in an external cavity, firstly, we suppose that the cavity length is arranged to match the length of the laser cavity or that $FSR = f_{rep}$. This would ideally leads to the transmission of all comb modes. In practice we have to consider another mirror property – the chromatic dispersion. Any dispersion originating in the mirror coatings or intracavity matter will cause cavity FSR to vary across the spectrum and affects the transmitted bandwidth [66]. Overlapping of evenly spaced comb modes with cavity modes that are now (because of the dispersion) spaced frequency-dependently will be thus bandwidth–limited. If the cavity and the comb are well overlapped in one region, they walk off one another in other regions [64]. Phase shifts associated with the dispersion $\Phi_d(\omega)$ can be included into the cavity round trip phase shift

$$\phi = \frac{2L\omega}{c} + \Phi_d(\omega). \tag{4.7}$$

A Taylor series expansion of the dispersion phase shift around a center frequency ω_c, which is assumed to be exactly resonant with the cavity, yields

$$\Phi_d(\omega) = \Phi_{d0} + \Phi_{d1}(\omega - \omega_c) + \frac{1}{2}\Phi_{d2}(\omega - \omega_c)^2 + ... \tag{4.8}$$

The first term gives an overall offset to the cavity modes and the second term uniformly changes the cavity FSR. Both terms can be easily compensated by changing the comb offset frequency f_0 for the overall offset and the comb f_{rep} for the second term. Quadratic and higher order terms have limiting effect on the transmission bandwidth since they describe how the FSR changes with frequency. By writing the group delay $T_g = \frac{d\Phi_d}{d\omega}$ of the pulse in one cavity round-trip, which is the reciprocal of FSR, we can define the group delay dispersion (GDD) of the cavity as

$$GDD = 2\pi\frac{d}{d\omega}\frac{1}{FSR(\omega)}. \tag{4.9}$$

With this equation we can calculate limit values of GDD corresponding to the allowed mode mismatch in the frequency comb bandwidth when selecting the ideal filter cavity mirrors. A criterion for the cavity bandwidth can be given by setting maximum value of the mismatch between the cavity and the comb mode to $\Delta\nu$ [20].

Another important property of the mirrors is their radius of curvature. The radius of the curvature of mirror r is essential for the cavity stability and the suppression of higher order transverse modes. A stable cavity must fulfill the stability criterion $0 < g_1 g_2 < 1$, where $g_i = (1 - L/r_i)$ and indexes 1, 2 correspond to two mirrors. With an imperfect coupling of the frequency comb to the TEM_{00} mode of the cavity, high order transverse modes can be close to or coincide with comb modes which we want to suppress. With appropriate choice of r, resonant frequencies of the cavity can be arranged such that they are located out of the FC modes [18]. The resonance frequencies of the cavity are given by

$$\nu_{k,i,j} = \frac{c}{2L}\left(k + \frac{1+i+j}{\pi}\frac{1}{\cos(\sqrt{g_1 g_2})}\right) \tag{4.10}$$

with longitudinal and transversal mode numbers k, i, j.

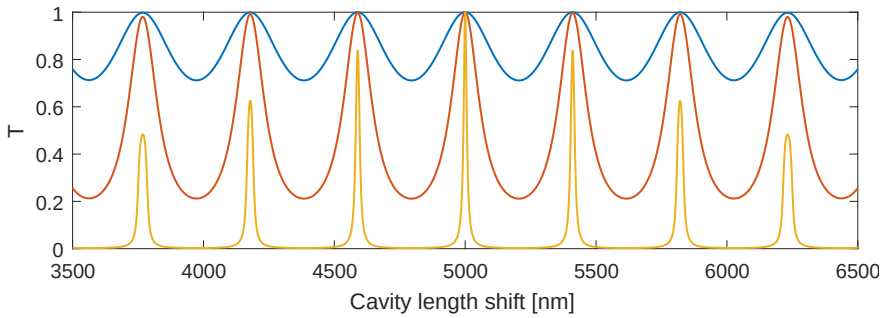

FIGURE 4.2: The cavity transmission of the frequency comb with central wavelength λ=820 nm, $f_{rep} = 1$ GHz and $f_0 = 0$ GHz as a function of the cavity length shift around length corresponding to FSR=1 GHz for 3 values of finesse F= 1, 3, 30 (blue, red, yellow).

With premise that the cavity dispersion is negligible and the comb is coupled to the TEM_{00} cavity mode, we compute the cavity transmission of the frequency comb as a function of cavity length L around value $L = \frac{c}{2FSR}$ for which

$$FSR = f_{rep}. \tag{4.11}$$

This corresponds to searching for a correct cavity length when parameters of the frequency comb are fixed. At this positions all comb modes are in resonance with cavity modes. The computation is done individually for each comb mode and then the sum of 10^4 modes is plotted in Fig. 4.2. The cavity transmission occurs at cavity length

$$L_c = \frac{c}{2f_{rep}}. \tag{4.12}$$

Since the cavity finesse is finite, non-exact solutions of Eq. (4.11) can be found. These solutions will result in a set of lateral transmission peaks. The comb spectrum transmitted through a lateral peak will have decreased spectral bandwidth, which is inversely proportional to the finesse and the cavity length detuning. The clocest lateral peaks on each side of the central one occur when a certain cavity mode n_{cav}, that is at the cavity length L_c in resonance with a comb mode n_{FC}, will be in resonance with mode $n_{FC} \pm 1$, see Fig. 4.3. At this point $FSR \neq f_{rep}$, but nonzero linewidth $\Delta\nu$ of cavity modes allows for transmission of many comb modes. Higher order lateral

peaks have a greater $FSR - f_{rep}$ mismatch and consequently are shorter and broader. The cavity length can be unintentionally tuned into one of the lateral transmissions because their corresponding cavity lengths differ from L_c only in a nanometer range. This cavity length difference ΔL_c is given by

$$\Delta L_c = \frac{c}{2\nu}\frac{f_{rep}}{FSR} = \frac{\lambda}{2}. \tag{4.13}$$

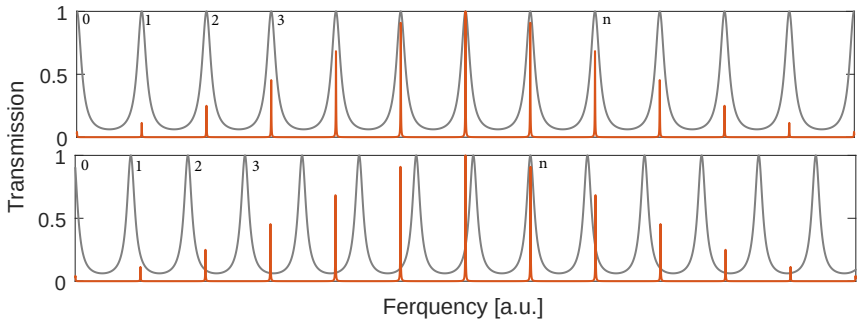

FIGURE 4.3: Origin of lateral peaks. Scheme of matching a low finesse (F=30) cavity modes (gray) to FC modes (red) for the central transmission peak – up and for a lateral peak – down.

Up until now we did not consider the effect of the nonzero offset frequency f_0. In the most extreme case, where $f_0 = f_{rep}/2$ there is an offset between cavity and comb modes such that at L_c the comb modes just overlap with cavity transmission minima, the comb is largely reflected and no light is transmitted. By scanning the length of the cavity, thereby very narrowly changing the cavity mode spacing, as in the previous case in Fig. 4.2, we can find symmetrical lateral peaks around L_c. The change in L compensates for f_0 by aligning the cavity modes to the FC modes, however with a slightly different FSR and therefore a lower transmission bandwidth. Values of f_0 in between 0 and f_{rep} will lead to unsymmetrical peaks around L_c. It can be said that nonzero f_0 will shift all transmission peaks, the central one will become the lateral peak, eventually with an identical twin for $f_0 = f_{rep}/2$. The peaks height follows a transmission envelope shape, so the overall transmission of all peaks remains the same.

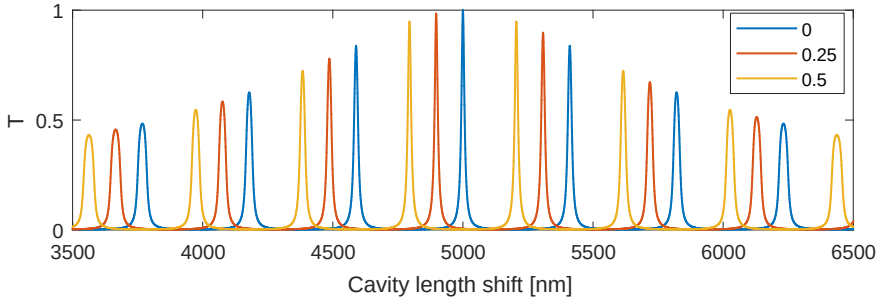

FIGURE 4.4: The cavity transmission as a function of length L for 3 values of f_0= (0, 0.25, 0.5)$\cdot f_{rep}$.

Since Eq. (4.12) holds only if the offset frequency f_0 equals zero, any offset frequency has to be compensated by slightly detuning the cavity by changing the cavity length by

$$\Delta L_{f_0} \approx \frac{\lambda}{2}\frac{f_0}{FSR}. \tag{4.14}$$

An example of the cavity transmission as a function of the cavity length and the effect of the offset frequency is shown in figure 4.4.

4.2 Frequency comb mode filtering

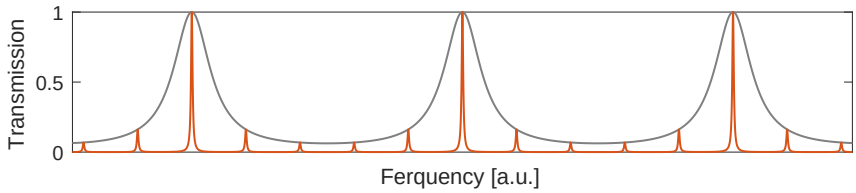

FIGURE 4.5: Example of low finesse $F = 6$ Fabry-Pérot cavity transmission (gray) of 1 GHz spaced FC modes (red). The cavity is set to "normal" configuration $FSR = 5 \cdot f_{rep}$.

The desired values of frequency comb mode spacing, comfortably resolvable by a diffraction grating spectrometer is above 30 GHz. Such values can be achieved by setting the cavity FSR to an integer multiple m of f_{rep}, $FSR = m \cdot f_{rep}$, see Fig. 4.5. To obtain FSR of 30 GHz, the cavity length has to by set to $L_c \approx 0.5$ cm. Such cavity arrangement is technologically very challenging, considering dimensions of common optomechanical components such as mirror kinematic mounts and piezoelectric actuators, together with the mirror radius of curvature. A better solution to achieve such filter ratios m has been found and it is presented in this section.

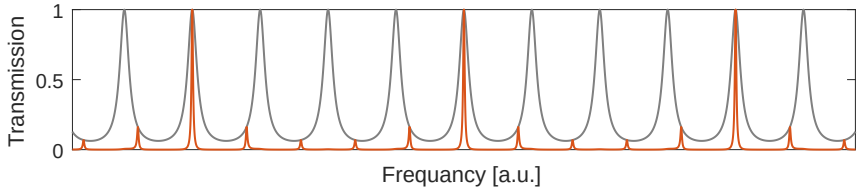

FIGURE 4.6: Example of low finesse $F = 6$ Fabry-Pérot cavity transmission (gray) with 1 GHz spaced FC modes (red). The cavity is set to Vernier configuration $4 \cdot FSR = 5 \cdot f_{rep}$. The $FSR = 1.25$ GHz, however 5 GHz spaced comb modes are transmitted.

This filtering method is based on the Vernier effect, with the cavity FSR set to a non-integer multiple of the f_{rep}

$$iFSR = mf_{rep}, \tag{4.15}$$

where i and m are integers. This is a scheme that is similar to frequency comb Vernier spectroscopy, see e.g. [38]. As a result we obtain a spectrum consisting of modes spaced by the lowest common multiple of the FSR and f_{rep}. Rewriting equation 4.12

in the Vernier configuration, the cavity transmission occurs at cavity length

$$L_c = \frac{i}{m}\frac{c}{2f_{rep}}. \tag{4.16}$$

Similarly the distance between transmission peaks ΔL_c is given by

$$\Delta L_c \approx \frac{c}{2f}\frac{f_{rep}}{iFSR} = \frac{\lambda}{2m}. \tag{4.17}$$

An interesting result is that the peak to peak distance ΔL_c is given only by the wavelength λ and the multiplication factor m. Thus a measurement of ΔL_c can be used for checking the factor m respectively the cavity length L_c. An example of the cavity transmission as a function of frequency is shown in Fig. 4.6.

The advantage of the Vernier method is that the filter ratio is not inversely proportional to the cavity length and high filter ratios m can be obtained, via high values of the factor i, with a large mirror to mirror distance. This allows to build such a cavity with common optomechanical components and also to adjust the filter ratio ranging from 10 to infinity with small change of the cavity length. In practice, the largest filter ratio sufficiently filtering unwanted modes is proportional to the cavity finesse. For the distance measurements presented in this thesis, we used filter ratio of $m = 56$ and factor $i = 3$ corresponding to $FSR = 18.\bar{6}f_{rep}$. A simulation of the comb mode suppression for such parameters is in Fig. 4.7. The slight detuning of the cavity to account for nonzero f_0 leads to a small mismatch between the cavity resonance and the comb wavelengths. However, for an optical bandwidth of 14 nm, which is the spectral width of the Ti:Sapphire laser used in this thesis, it only leads to a 0.1 dB decrease of the transmitted signal in the wings of the spectrum.

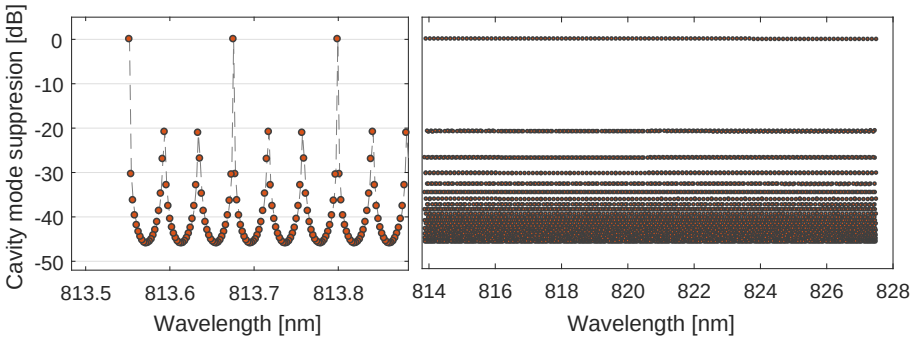

FIGURE 4.7: Simulation of frequency comb mode suppression by filter cavity with $FSR = 18.\bar{6}$ GHz. The comb repetition rate is $f_{rep} = 1$ GHz, the offset frequency $f_0 = 180$ MHz and the bandwidth of 14 nm is centered at 820 nm. With a cavity finesse $F = 313$ (mirror reflection 99%), the suppression of unwanted modes remains below -20 dB. The transmission of wanted modes is suppressed at the edges of the spectrum due to the offset frequency only by 0.1 dB. On the left side a small zoomed part of the spectrum is shown, to visualize individual modes. On the right side the mode suppression is shown for the full spectrum.

Chapter 5

Experimental setup for distance measurements

The experimental setup for the distance measurements can be divided into three main parts: a light source, a Michelson interferometer and a grating spectrometer, see Fig. 5.1. The light source is a Ti:Sapphire pulsed laser with the pulse repetition rate $f_{rep} = 1.012$ GHz and the offset frequency $f_{ceo} = 180$ MHz. The emitted optical spectrum is an optical frequency comb centered at wavelength $\lambda_c \approx 820$ nm with bandwidth of 14 nm.

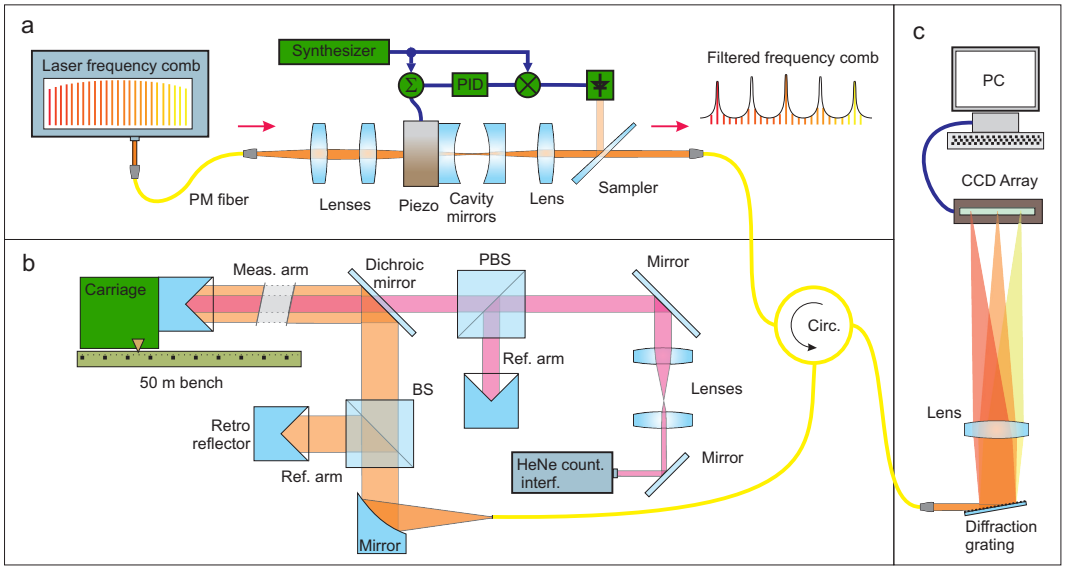

FIGURE 5.1: Experimental setup of the relevant parts for the distance measurement split into 3 sections. *a*) Filtering part showing the frequency comb laser, cavity mode-matching optics, cavity with piezo actuator, collimation lens and beam sampler. The green parts are the detector and electronics for locking the cavity length. The filtered frequency comb is led through an optical circulator towards the 50 m bench part. *b*) This part shows two Michelson interferometers with a common measurement arm for the filtered frequency comb and the He-Ne laser. *c*) Spectral analysis of the interferometer output with a diffraction grating and linear CCD camera.

The filter cavity based on two dielectric mirrors is used to increase the repetition rate of the frequency comb. The interferometer consist of two combined Michelson interferometers with common measurement arm, one is dedicated to frequency comb measurements and the other serves for comparison measurements utilizing a He-Ne

continuous wave laser and interference fringe counting method. The spectral analysis is done with the grating spectrometer, however the VIPA spectrometer is also implemented into the setup for investigation of the filter cavity performance.

5.1 Filter cavity setup

The filter cavity setup consists of a symmetrical Fabry-Perot cavity, cavity mode-matching optics and cavity-comb locking optics and electronics.

5.1.1 Cavity mirrors

Optical criteria for the mirror parameters in spectral region $810 - 830$ nm can be summarized as:

- Mirror reflectivity of the first surface $R \approx 99\%$
- Group delay dispersion for one reflection below 20 fs^2
- Mirror radius of curvature of the first surface 15 $mm \leq r \leq \infty$
- Antireflection coating on the second surface

The cavity finesse is the most important criterion for sufficient spectral filtering of unwanted comb modes. We have chosen the suppression ratio of the closest neighboring comb mode to be at least 20 dB. From Eq. (4.4) we estimated the mirror criteria for sufficient spectral filtering. To obtain this suppression consistently in the whole region a walk-off between the comb and the cavity modes caused by mirrors dispersion has to be minimized. A symmetric cavity was built with two concave dielectric mirrors (*Layertec*). Both having a reflecting side radius of curvature r = 50 mm, diameter 12.7 mm and thickness 6.35 mm. The reflecting side has a coating with reflectivity of $R = 99.0\%$ and GDD below 20 fs^2 in the relevant spectral region, see Fig. 5.2. The flat side of the mirror has an antireflection coating with $R_{ar} < 0.2\%$.

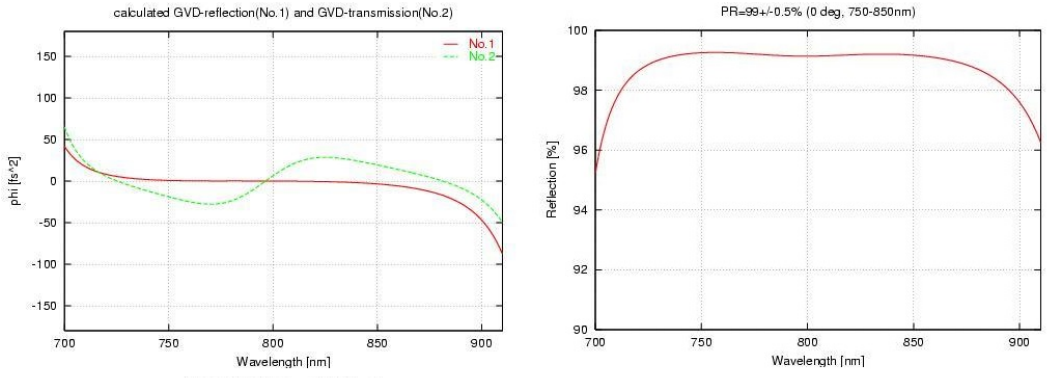

FIGURE 5.2: Spectral properties of mirror surfaces. Left, GDD for the reflectrion and transmission. Right, the reflection of the curved surface [*Layertec datasheet*].

Each cavity mirror is attached to ring piezoelectric actuators (*Piezomechanik*). One piezochip *PCh150/12-6/2* with stroke 2 μm works as a cavity length modulator for cavity length dithering with a few kHz frequency and a nanometer amplitude and

the second piezostack *HPSt150/14-10/12VS22* with stroke 12 μm ensures fine tuning of the cavity length and control. The piezostack has already incorporated mirror mount, for the piezochip a mirror mount was manufactured at the VSL workshop. The mount consists of a hollow metal body with three copper leaf springs which press a metal ring against the mirror placed on the piezochip, see Fig. 5.3. Both mirror mounts are attached to standard commercial kinematic mounts with use of VSL–made adapters. One of the kinematic mounts is a x-y translation mount and the other is an angle adjustment mount placed on a z axis translation stage, see Fig. 5.4.

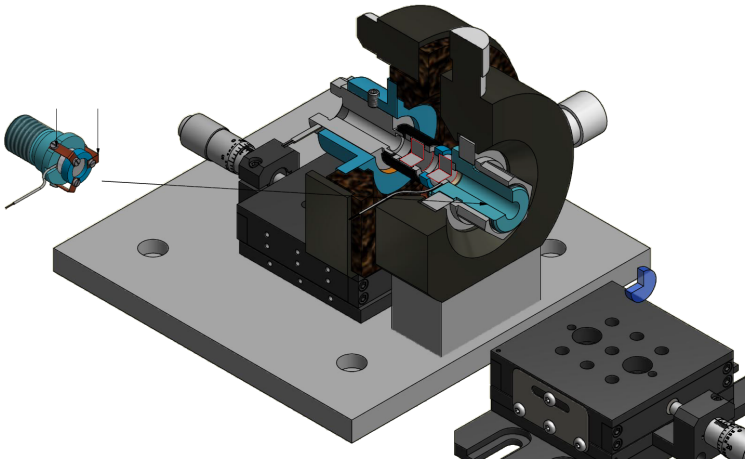

FIGURE 5.3: A cut view of the 3D model of the cavity with mirrors attached to piezoactuators and mounted onto kinematic mounts. The custom made mirror-piezo mount is shown also separately. The mirrors have red contours.

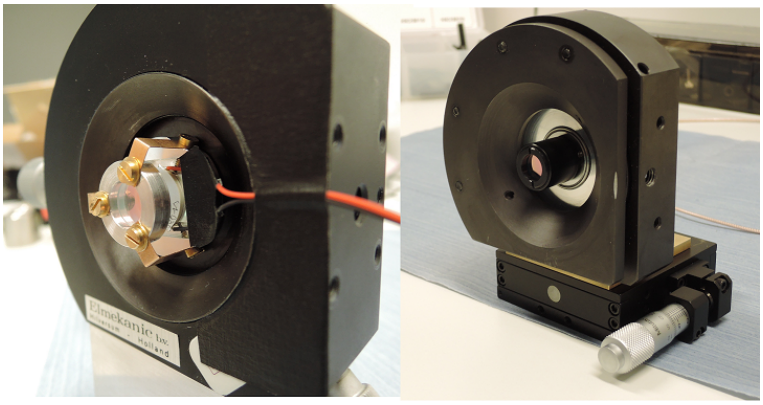

FIGURE 5.4: The filter cavity mirrors attached to piezoactuators and mounted onto kinematic mounts. Left – x-y translation mount, right — angle mount on z axis translation stage.

5.1.2 Cavity mode matching

For successful coupling of a laser beam to an optical cavity, the radius and wavefront curvature of the beam has to match to a transversal eigenmode of the cavity. It is desirable to couple only to the TEM_{00} mode of the cavity since coupling to higher order

transversal modes would of-course lead to emission of those higher modes from the cavity. This is a problem since the higher orders might spectrally coincide with and thus transmit comb frequencies which we want to filter out. Also consequent laser beam coupling to the rest of the setup via a single mode fiber would be extremely inefficient. To obtain clean Gaussian beam or TEM_{00} as the cavity output, two achromatic lenses are used to mode-match the laser beam to the cavity mode. The laser beam parameters, i.e. the position of the beam focus and the Rayleigh range are set by an achromatic collimator at the output of a single mode fiber which brings the light from the frequency comb. The parameters can be found by measuring the $1/e$ electric field radius W of the beam at two different distances z_1, z_2 from an arbitrary reference point and solving the system of equations

$$\begin{aligned} W(z_1) &= \sqrt{\frac{\lambda z_0}{\pi}}\left[1+\left(\frac{x+z_1}{z_0}\right)^2\right]^{-1/2} \\ W(z_2) &= \sqrt{\frac{\lambda z_0}{\pi}}\left[1+\left(\frac{x+z_2}{z_0}\right)^2\right]^{-1/2}, \end{aligned} \tag{5.1}$$

where z_0 is the Rayleigh range of the beam waist and x is the distance from the reference point to the beam waist. The parameters of cavity TEM_{00} mode can be obtained from the ABCD matrix [67] , which describes one cavity round trip starting in the center of the cavity

$$\begin{aligned} \begin{pmatrix} A & B \\ C & D \end{pmatrix} &= \begin{pmatrix} 1 & \frac{L_c}{2} \\ 0 & 1 \end{pmatrix}\begin{pmatrix} 1 & 0 \\ -\frac{2}{r} & 1 \end{pmatrix}\begin{pmatrix} 1 & L_c \\ 0 & 1 \end{pmatrix}\begin{pmatrix} 1 & 0 \\ -\frac{2}{r} & 1 \end{pmatrix}\begin{pmatrix} 1 & \frac{L_c}{2} \\ 0 & 1 \end{pmatrix} \\ &= \frac{1}{r^2}\begin{pmatrix} 2L^2-4Lr+r^2 & L(L^2-3Lr+2r^2) \\ 4(L-r) & 2L^2-4Lr^2 \end{pmatrix}. \end{aligned} \tag{5.2}$$

The TEM_{00} eigenmode of the cavity is described by the q-parameter whose real part contains information about the position of the beam waist and the imaginary part is the Rayleigh range

$$q(z) = z - iz_0. \tag{5.3}$$

This parameter is calculated from the ABCD matrix by

$$q = \frac{Aq+B}{Cq+D}. \tag{5.4}$$

As the fiber output coupler we choose achromatic collimator *PAFA X-4-B* from *Thorlabs* and we set the distance between the collimator and the cavity to 30 cm to keep dimensions of the setup mountable on a transportable breadboard. With known parameters of the cavity and beam eigenmodes there are still many possibilities for selecting the positions and focal lengths of the lenses. Therefore we limit the focal lengths to values for which AR coated achromatic lenses are available in the *Thorlabs* catalog. Positions for given set of focal lengths are calculated using *MATLAB* genetic algorithm tool, which enables to search for ideal result in many randomly generated generations of positions. An example of resulting mode-matching optics configuration for cavity FSR= 10 GHz and also with two lenses for the cavity output beam expansion and collimation is in Fig. 5.5 and the used components and their positions are listed in table 5.1.

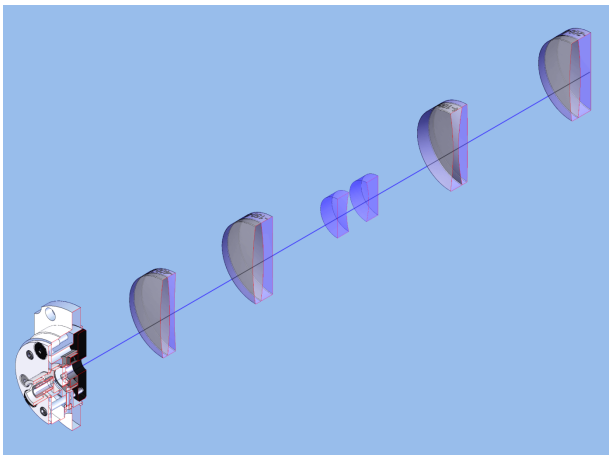

FIGURE 5.5: Isometric cross section of optical scheme of the filter cavity and mode-matching optics for cavity with FSR = 10 GHz. The cavity output beam is expanded and collimated.

Component (Item#)	**Description**	**Focal length**	**Position**
PAFA X-4-B	AR achr. collimator	4 mm	0 mm
AC254-400-B	AR achr. doublet lens	400 mm	108 mm
AC254-125-B	AR achr. doublet lens	125 mm	208,5 mm
#103239	AR coated cavity mirror	-100 mm ; 25 mm	292,5 mm
#103239	AR coated cavity mirror	-100 mm; 25 mm	307,5 mm
AC254N-100-B	AR achr. negative doublet lens	-100 mm	398,6 mm
AC254-200-B	AR achr. doublet lens	200 mm	548,7 mm

TABLE 5.1: Optical components for mode matching laser beam output from a single mode optical fiber into the free space cavity with FSR = 10 GHz as pictured in Fig. 5.5. The mirrors have two focal lengths because they act as a focusing mirror and as a diverging lens.

Adjustment of mode-matching optics to proper coupling of the laser beam into the cavity TEM_{00} mode is done by a beam profile characterization after the cavity. Output beam is after collimation directed onto a CCD camera. An useful way to achieve the signal on the camera is at first to shine the beam directly from the collimator onto the camera without any optics. Then the lenses at their positions and a pin hole at the position of the cavity waist are placed and collimated beam with the signal at the same spot on the camera is achieved. After this step, the pin hole is removed, the second (in the direction of the laser beam propagation) mirror is placed and reflection in the counter propagating direction is achieved. The same step is then done with the first mirror. After this procedure, fine adjustment mainly of the cavity mirrors is needed to achieve the TEM_{00} mode of the output beam, however scanning the cavity length with the piezoelectric stack during this process might be also necessary.

5.1.3 Cavity-comb locking

After successful coupling of the laser beam to the cavity TEM_{00} mode, the behavior of the cavity is tested by measurement of the cavity transmission with respect to the cavity length. The cavity length is roughly adjusted by the z-axis translation stage close to the length corresponding to requisite FSR (e.g. 10 GHz) and scanned around

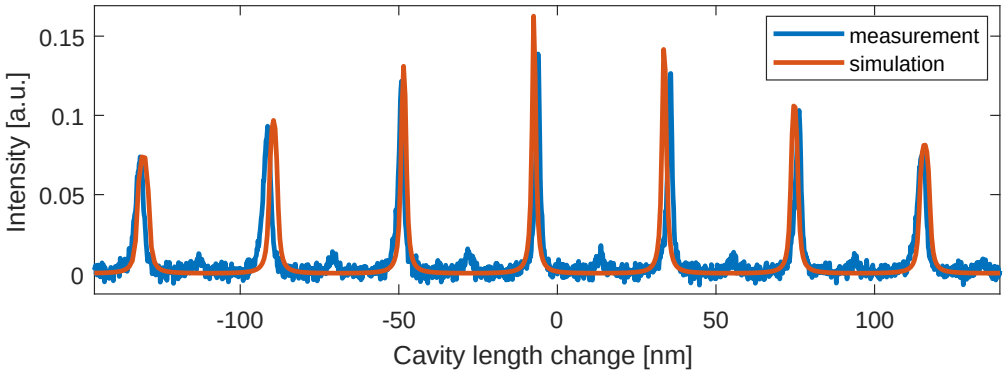

FIGURE 5.6: Measured cavity transmission – blue as a function of cavity length compared to simulation – red. Small peaks in between the predicted ones correspond the higher order modes and suggest yet imperfect mode matching adjustment.

this position by the long piezoelectric actuator. The scanning is done rather fast, in tens of milliseconds, to prevent from the cavity length drift caused by environmental perturbations. Collimated laser beam after the cavity is split by a beam sampler and 10% of light is directed into a photodetector for transmitted intensity measurement. The cavity transmission occurs for cavity lengths $L_c = c/(2mf_{rep})$ as an envelope, where within each envelope is underlying series of transmission peaks separated by $\Delta L_c = cf_{rep}/(2FSR)$, Fig 5.6. Each envelope has its central peak with maximum transmission intensity and for cavity with finesse $F = 300$ this peak have the FWHM linewidth in the cavity length of 1.4 nm.

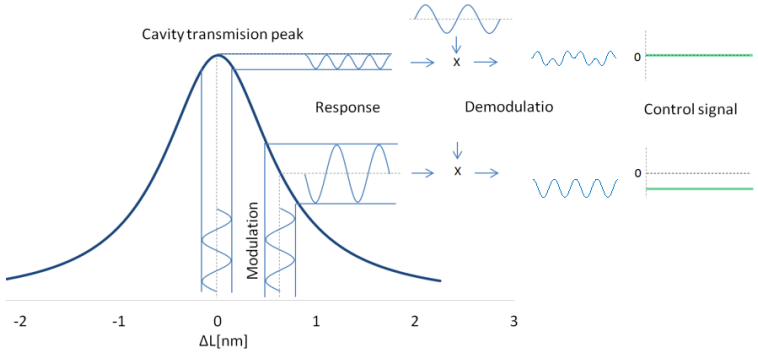

FIGURE 5.7: Cavity transmission as a function of the cavity length and the scheme of cavity length modulation and control signal generation.

To keep continuous transmission and filtering of frequency comb modes, it is necessary to stabilize the cavity length by electronic servo-loop onto the position of required transmission peak of the cavity. The stabilization is performed by deriving a control signal from a photodiode that monitors the intensity of the 10% laser light sample after the light has passed the cavity. The control signal is derived from the photodiode response after modulating the transmission of the cavity by periodically changing the position of the cavity mirror with small piezochip, schematically shown in Fig. 5.7. By demodulating the response of the photodiode signal,

generated control signal can drive the mirror towards the position of the intensity maximum. Control signal corresponds to the first order derivative i.e. local slope of the transmission peak intensity profile. The sign and intensity of the control signal depends on the slope as well as on the phase between the modulation signal and the response signal. Demodulation, phase correction and control signal is provided by digital signal processor (DSP) *ADwin Gold* system, whose electronic block diagram is in Fig. 5.8. Because of *ADwin Gold* maximum voltage output is 10 V, piezoelectric actuator for tuning and stabilization is powered through high voltage amplifier (HV).

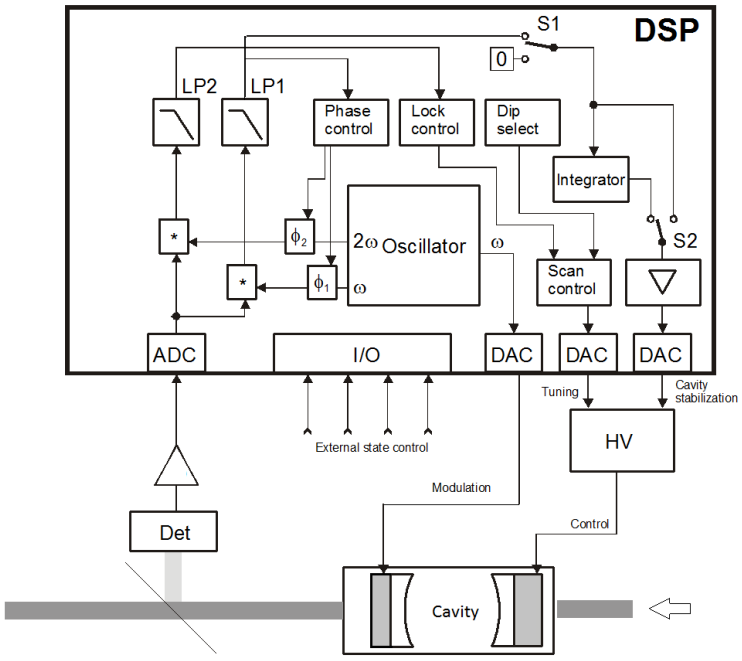

FIGURE 5.8: Block diagram of the cavity locking digital signal processor *ADwin Gold*. The internal oscillator runs at an angular frequency ω and provides both the modulation and demodulation signals. The left part represents the lock-in amplifier with the demodulation stages and low pass filters. The system uses the second harmonic response for various internal settings like the phase and lock control of the controller. The first harmonic is used to derive the control signal for the cavity stabilization.

The 90% rest of the cavity output is coupled to a single mode fiber circulator, since the Michelson interferometer is in other room than the rest of the setup. The circulator allows to send the comb beam from the cavity via 10 m long single mode fiber to the interferometer and also to send the interference signal through the same fiber back to the circulator which directs it to the spectrometers.

5.2 Interferometer and spectrometer

5.2.1 Interferometer

The interferometer is located at the VSL long distance measurement laboratory. The laboratory is equipped with 50 m long rail bench. A commercial He-Ne laser fringe counting interferometer head (*Agilent*) is also part of the experimental setup and

serves for the distance measurement comparison. The Michelson interferometer for frequency comb has common measurement arm with the counting interferometer. The interferometer is built with 2 inch sized optics, using a non-polarizing beam-

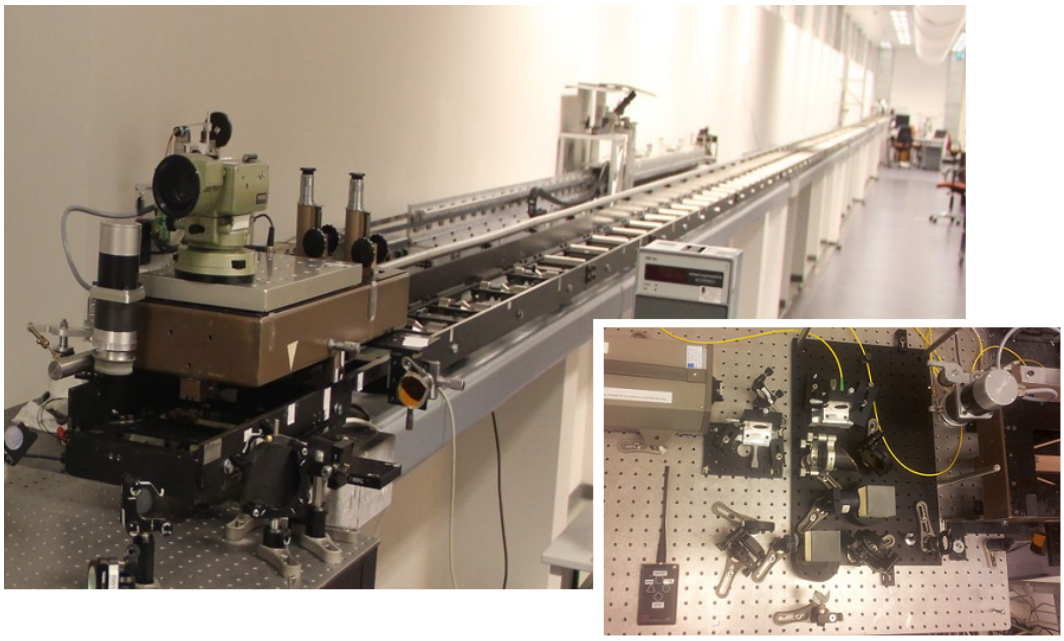

FIGURE 5.9: Large image: Long bench - the Michelson interferometer measurement arm with electronic carriage. Small image: interferometric head based on two inch sized optics.

splitter and gold coated hollow retroreflectors. The measurement arm has a maximum length of 50 m and consists of a long rail with electric carriage carrying the retroreflector, see Fig. 5.9. The large sized optics is used due to intention to have the laser beam wide and collimated even for measurements up to few hundred meters in the possible filed applications. Large beam divergence would lead to decrease of interferometric beam–fiber coupling efficiency. Another reason is a few millimeter off axis movement of the electric carriage as it moves in the measurement axis. This movement causes spatial fluctuations of the returning beam. The beams being wide relative to the off-axis movement satisfy good overlapping of the beams from both interferometer arms. The comb beam is collimated directly from the single mode fiber ferrule into the interferometer with an off-axis parabolic mirror. The 5 μm mode field diameter of the fiber, numerical aperture 0.13, with 101.6 mm focal length of the parabolic mirror leads to 26 mm $1/e^2$ intensity beam diameter. The hollow retroreflectors have an effective diameter of about 35 mm. After the non-polarizing beamsplitter the comb beam is in the measurement arm mixed with the He-Ne beam. A dichroic mirror reflects the comb beam at 820 nm wavelength while it transmits the continuous-wave beam of the He-Ne laser at 633 nm. As a result, both beams largely propagate through the same volume of air having the shared measurement arm. The reference arms for the comb and the He-Ne laser are different, since the He-Ne laser interferometer is based on measurements requiring a polarizing beam splitter. The He-Ne laser beam with $\approx$ 1 cm diameter is, before it enters the interferometer, also 3$\times$ expanded with a two lens telescope in order to have similar width as the comb beam. After propagation through the Michelson interferometer, the light from the He-Ne laser propagates back through the same path

to the He-Ne laser head which contains a detector for fringe counting. The comb interferometric output propagates back into the circulator via the same optical path and optical fiber. The fiber circulator directs the light towards the spectrometers.

5.2.2 Spectrometers

The VIPA interferometer is implemented in the setup for diagnostic purposes. Returning beam from the interferometer is directed by the circulator to a detection selector, which consists of a flip mirror and two sets of fiber couplers. Flipping of the mirror sends the comb interferometric output via single mode fibers towards either the grating spectrometer or the VIPA spectrometer. Both spectrometers are mounted on transportable breadboards and for the experiments the breadboards are on the frequency comb optical table together with the filter cavity setup, pictured on Fig. 5.10. The grating spectrometer uses the source fiber connector ferrule as an

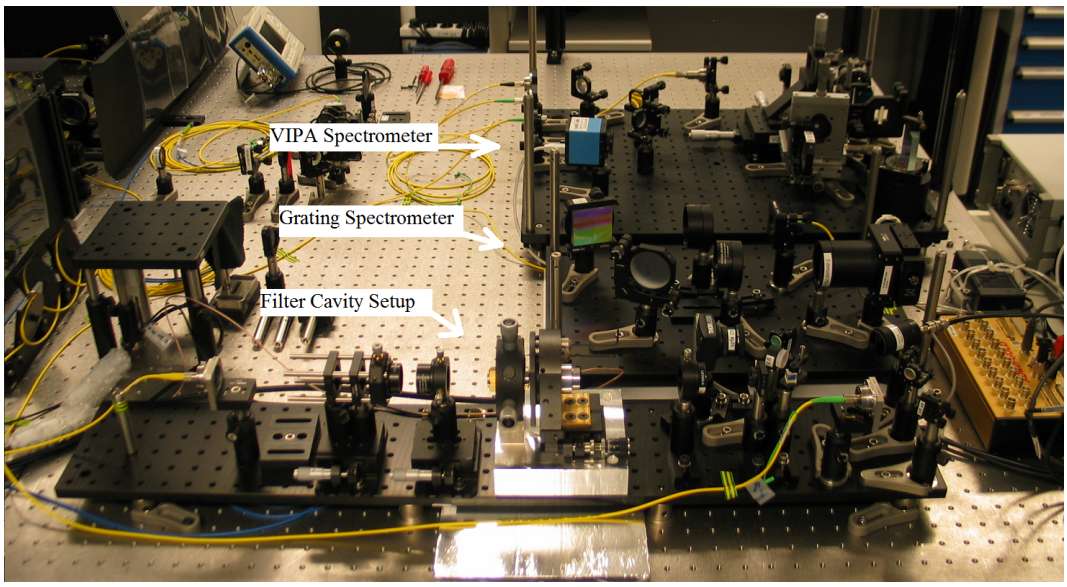

FIGURE 5.10: Three transportable breadboards, one with filter cavity setup and one for each of the spectrometers.

entrance slit with 5 μm mode field diameter. The light is collimated by an achromatic lens with 100 mm focal length directly in grazing incidence onto a 50 mm wide reflective holographic diffraction grating with 1800 grooves/mm. The first order diffraction is focused with a 200 mm focal length achromatic lens on a sensor of CCD line camera. The camera has 3000 pixels, 7 μm pixel pitch and 200 μm pixel height. This configuration provides sufficient resolution to distinguish 20 GHz separated filtered comb modes, while capturing the full 20 nm wide spectral range of the comb spectrum.

The VIPA spectrometer is based on a VIPA etalon with 53 GHz free spectral range and surface reflectances of $\approx$ 100% and 99.5%. The comb interferometric output is collimated by a fiber collimator and its polarization is cleaned by a polarizer. A cylindrical lens with 100 mm focal length focuses the beam on the VIPA 99.5% surface. VIPA then disperse the light in vertical direction towards a blazed diffraction grating with 1200 grooves/mm, which disperse the light in horizontal direction. A 400 mm focal length achromatic lens images the light on a CCD camera. For calibration of this spectrometer a reference diode laser is also incorporated into the setup.

The diode laser has a tunable wavelength range of 817.0±1.1 nm. The diode laser beam is mixed with the comb beam at a polarization beamsplitter placed before the single mode fiber that brings the light to the filter cavity. The second output of the diode mixing beamsplitter brings the light to a wavemeter for wavelength control.

Chapter 6

Measurements

This chapter in the first section describes the performance of the filter cavity by means of imaging the filtered frequency comb with the VIPA spectrometer. The second part is dedicated to measurements of distances using the filtered frequency comb and the grating spectrometer.

6.1 Cavity filtration performance

When cavity length is scanned in the μm range its transmission shows many envelopes of transmission peaks. Each envelope corresponds different parameters i and m in the Vernier filtering condition $i \cdot FSR = m \cdot f_{rep}$. As an example, the second derivative of the cavity transmission is shown for cavity length scan with scanning range of about 1 μm showing the envelope for FSR = 20 GHz and approximately 100 μm scanning range around FSR ~20.15 GHz with many envelopes.

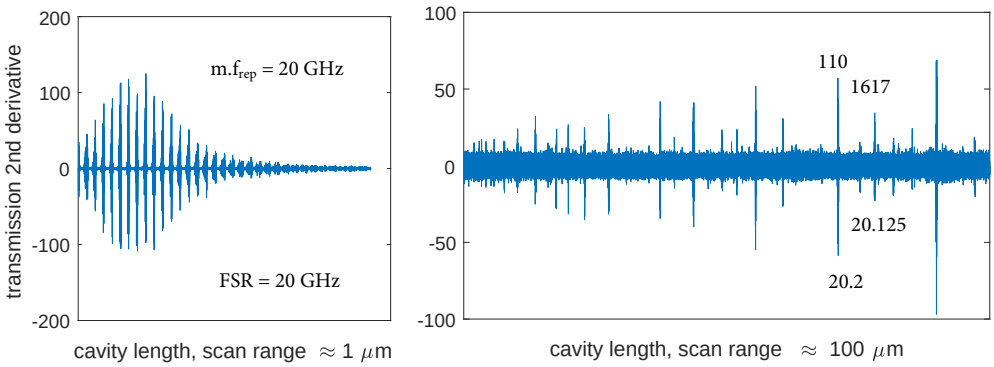

FIGURE 6.1: The second derivative of the cavity transmission as a function of cavity length. The transmission envelope for FSR=20 GHz – left, many envelopes within a 100 μm scanning range – right. The second derivative is used to enhance the visibility of the envelopes. Values of the cavity FSR and corresponding multiplied repetition rate $m \cdot f_{rep}$ are shown below respectively above envelopes.

Each envelope consists of a series of transmission peaks, as described in the chapter 4.1.2. Locking the cavity to one of the peaks, ideally the highest one, represents a stable frequency comb filtration with a filter ratio m. Changing the ratio m multiple times in the Vernier configuration can be done by a fractional change of the cavity length. As can be seen in Fig. 6.1 in the vicinity of FSR = 20 GHz, there are visible transmission envelopes for $m \cdot f_{rep}$ in the THz range. Theoretically the filter ratio can

be adjusted to infinity, however the practical limit is the 1/2 cavity finesse which is proportional to the largest filter ratio m sufficiently filtering unwanted comb modes.

6.1.1 Filtered comb VIPA spectra

The high resolution VIPA spectrometer is used here for diagnostic purposes. It resolves all the modes of the Ti:Sapphire frequency comb laser, separated by $f_{rep} \approx$ 1.012 GHz, and creates a 2D image of dotted VIPA pattern. Note that the f_{rep} value is often rounded to 1 GHz in this text. Each dot is an individual comb mode. In the vertical direction, dot to dot distance represents the f_{rep}, in the horizontal direction dot-to-dot distance represents the FSR of the VIPA etalon.

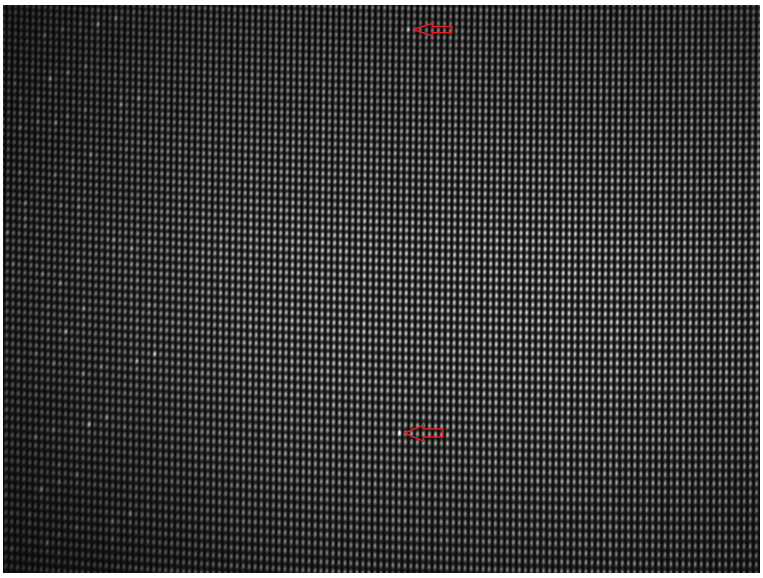

FIGURE 6.2: VIPA spectrum of the unfiltered frequency comb mixed with the diode laser. Each column of dots represents one order of the VIPA etalon transmission. Adjacent orders of transmission are shifted in the vertical direction by 53 GHz to each other and dispersed in the horizontal direction by the diffraction grating. The diode laser mode can be seen in the middle part of the image as two bright spots. They are in two adjacent columns and 53 rows from each other. The bright dots on the left side comes from the frequency comb laser and are its short lived cw modes caused by small coupling of the diode laser into the frequency comb laser cavity.

Since the VIPA etalon has FSR of 53 GHz and the VIPA image has in the vertical direction more than 53 GHz span, there are dots which corresponds to the same laser mode. To calibrate the VIPA image in the frequency domain a continuous wave diode laser is used as the reference. Although the distance measurements does not need the frequency calibration, spectrum of the diode laser is shown in Fig. 6.2 together with the frequency comb spectrum to manifest the pattern of repeating position of a mode in the spectrum. The spectrum is measured at once as a combined laser beam of the comb and diode beams. The diode laser mode can be seen in the middle part of the image as two bright spots. They are in two adjacent columns and 53 rows from each other. The bright dots on the left side comes from the frequency comb laser and are its short lived CW modes or mode-not-matched modes. They are caused by small coupling of the diode laser into the frequency comb laser cavity.

With the diode laser blocked, they vanishes. They also appears in the spectrum of the frequency comb laser when it is not in the mode locked regime.

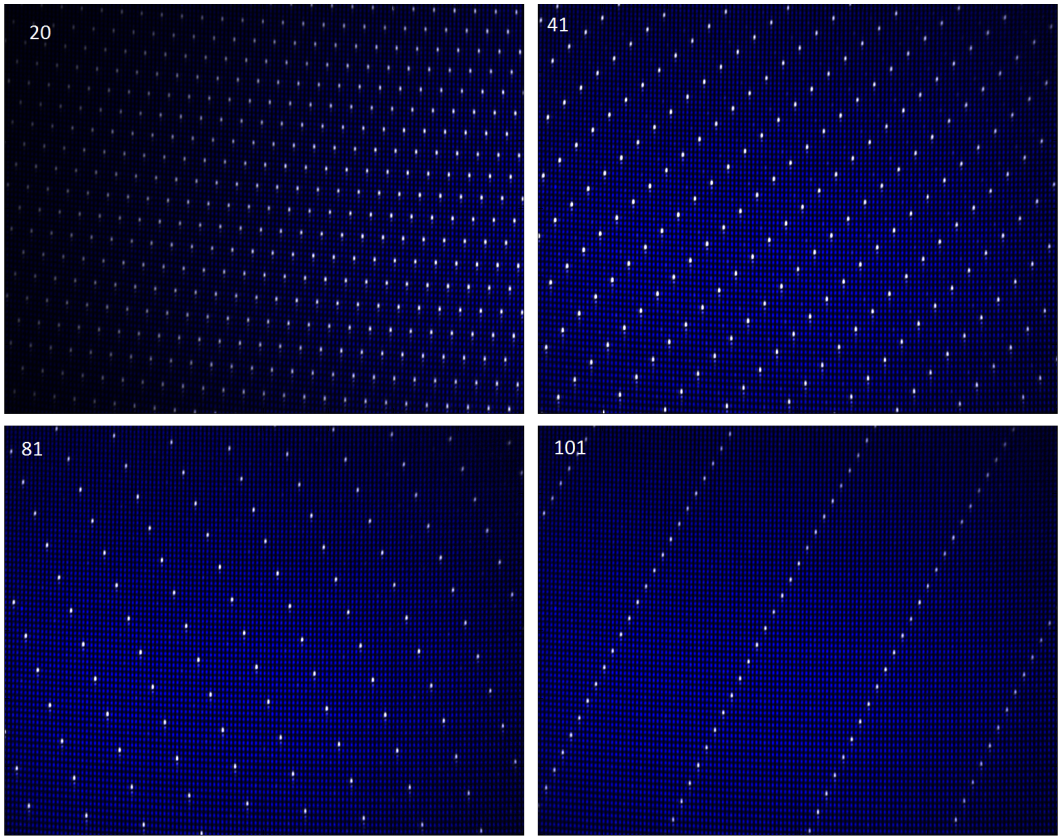

FIGURE 6.3: Composite VIPA spectra of the filtered frequency comb for four resulting values of $m \cdot f_{rep}$ = [20, 41, 81, 101] GHz (white dots) laying over the original unfiltered spectrum (blue dots)

As described earlier, the filter cavity can be comfortably set to a desired filter ratio. This is done by a coarse manual adjustment of the cavity length with a micrometer precision and fine piezostack tuning. Since the cavity length changes are small relatively to its length, there is no need for change in the mode matching optics. The performance of the comb mode filtering is shown in Fig. 6.3 for four settings of the cavity FSR described in Table 6.1, note that an approximation of f_{rep}=1 GHz is taken in the table.

L_{cavity} [mm]	7.50	7.43	7.41	7.32
FSR [GHz]	20	20.2	20.25	20.5
i	1	5	4	2
$m \cdot f_{rep}$ [GHz]	20	101	81	41

TABLE 6.1: Table of cavity settings fulfilling the vernier condition $i \cdot FSR = m \cdot f_{rep}$ for presented VIPA spectra.

6.1.2 Locking performance

It has been shown that the cavity can perform sufficient filtering of unwanted comb modes in a wide range of filter ratios. For the distance measurements, cavity has to

remain locked for a long time period. During this time, an environmental perturbation can cause unlocking and the subsequent re-locking to another lateral transmission peak. For the presented method of distance measurements, such event is not an issue. Re-locking to different peak results in transmission of a different set of comb modes, however with the same filter ratio. Moreover, re-locking to adjacent peak will lead to transmission adjacent set of comb modes. This can be used to reconstruction of the original comb spectrum from the filtered spectra.

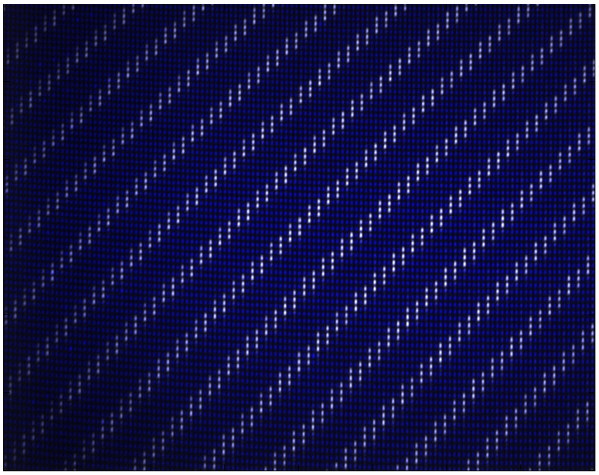

FIGURE 6.4: Example of combined VIPA spectrum of three filtered frequency comb spectra for adjacent transmission peaks with $m \cdot f_{rep}$ = 41 GHz (white dots) laying over the original unfiltered spectrum (blue dots).

Figure 6.4 shows partially reconstructed original frequency comb spectrum from three spectra of filtered comb with $m \cdot f_{rep}$ = 41 GHz with the cavity locked to three adjacent transmission peaks. It can be seen that all three spectra has similar intensity of their components across the spectrum. The cavity transmission bandwidth, for peaks around the transmission envelope maximum, can be thus considered the same.

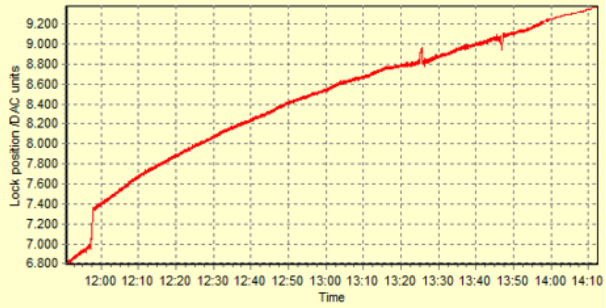

FIGURE 6.5: A record of the cavity locking voltage for 150 minute performance with voltage jumps corresponding to re-locking the cavity length onto cavity transmission peaks.

The performance of the cavity locking mechanism itself was sufficient for the laboratory distance measurements, however it was not tested outside the laboratory. In the record in Fig. 6.5 the piezostack voltage which keeps the cavity length locked

to the transmission peak is shown as a function of time. Visible voltage jump at the beginning of the measurement corresponds to the re-locking to another peak. Small voltage peaks at the end of the measurements correspond to re-locking to the same transmission peak. Parameters of the lock are modulation amplitude at piezochip of 1.8 V and modulation frequency of 1600 Hz.

6.2 Distance measurements

In this section a procedure and results of distance measurements using spectral interferometry with mode filtered frequency comb and diffraction grating spectrometer are presented. The distance measurements are performed quasi-simultaneously with the He-Ne laser fringe counting method, which serves as a comparison. The results are then presented as a difference between these two methods [56].

6.2.1 Cavity setting

The length of the filter cavity is set at 8.0 mm, corresponding to a $FSR = 18.\bar{6} f_{rep}$, which due to Vernier selection, results in a filter ratio $m = 56$. This corresponds to a pulse-to-pulse distance $L_{pp} = 5.3$ mm. The cavity resonance linewidth is $\Delta\nu \approx$ 100 MHz (FWHM). In order to obtain a clean Gaussian beam profile, a single mode optical fiber is used to couple the comb light to the cavity. After the cavity the laser beam is collimated with another achromatic lens and 10% of the light is directed with a beam-sampler into a photodetector for the cavity stabilization. The rest of the light is coupled into a fiber and propagates through an optical fiber circulator into the measurement section in a neighboring laboratory. Typically about 400 μW of the comb power is available after the filter cavity, providing about 100 μW to the setup for distance measurement after propagation through the fiber circulator. The filter cavity is shielded by a foam cover to keep it thermally stable and to suppress coupling of an acoustic noise into the cavity.

Correct setting of the filter ratio m is confirmed by measuring the change of piezo voltage, corresponding to the cavity length change, when the cavity is locked on successive transmission peaks, as calculated from Eq. (4.13). In practice it is more accurate to measure the piezo voltages for locking to n-th peak and the n+10th peak, which provides enough accuracy to estimate the filter ratio. Verification of the filter ratio m is done by measuring the distance with the He-Ne interferometer between two successive positions of the carriage with zero interference fringes on the camera. Since the distance between the pulses is reduced by mode filtering, the requirements on the a priori knowledge of the distance get tighter, but still a measurement accuracy of a few mm is sufficient to overcome the ambiguity.

6.2.2 Measurement procedure

Initially, the carriage of the measurement arm is positioned at the beginning of the bench and the counting He-Ne interferometer is set to zero. Five line camera pictures are taken, corresponding to five comb measurements of the zero position. Then the carriage is moved to a position roughly at 10 m, and again back to a position at zero m. This is done also for 20 m, 30 m, 40 m and 50 m positions. To be able to normalize the data, not only the interference signal is measured for each position, but also the signals from the reference and measurement arms individually, obtained with the other arm blocked. For each position, five comb measurements and five readings of the counting interferometer are recorded.

The measurement positions are selected arbitrarily, but positions very close to $L = 0$ and $L = L_{pp}/4$ are avoided, as will be discussed later. Due to environmental perturbations, the contrast of the comb interference pattern tends to diminish for too long integration time of the CCD array. Optical path length variations of only $\lambda/4 \approx 200$ nm are sufficient to wash out the fringes. For this reason it is required that the carriage is fixed during the measurement. The method can thus not be used for measuring while the target is being moved. In practice, a 0.4 ms acquisition time of the camera is an optimal value. The refractive index of air is determined from data of environmental conditions (temperature, air pressure and humidity) using the Edlén formula [68]. The temperature is measured at several positions along the measurement bench, simultaneously with the distance measurements.

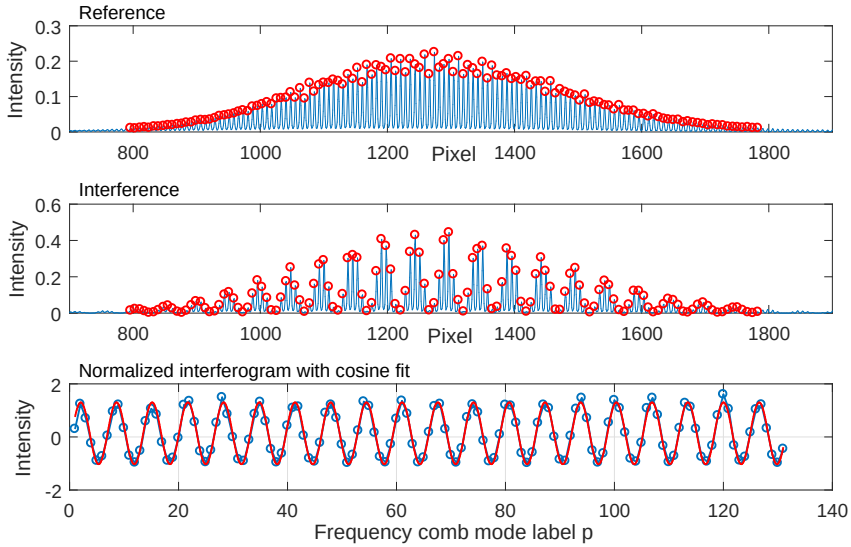

FIGURE 6.6: Top: typical reference measurement-blue, I_{ref} intensities - red circles. It is used for correct finding of the comb mode positions at CCD and also for the interference normalisation. Middle: interference measurement - blue, with values of $I(f)$ intensities - red circles. Bottom: normalized intensities $I(f)$ - blue circles and cosine fit - red.

The reference data from the measurement I_{meas} and reference I_{ref} arms are used for intensity normalization of interference spectrum I as shown in Fig. 6.6

$$\cos(\Phi) = \frac{I - I_{ref} - I_{meas}}{2\sqrt{I_{meas} I_{ref}}}. \tag{6.1}$$

From its cosine fit the distance L was calculated using Eq. (3.15) and the method mentioned in Section 3.1.3 is used for determining its sign. The distance measurements by the He-Ne counting interferometer are used for determining the integer j in Eq. (3.18) for the comb measurement. However, since the requirements on these measurements are mild, a simple electronic distance meter can also be used to overcome the non-ambiguity.

6.2.3 Results

The results in Fig. 6.7 show the differences between the individual measurements done by frequency comb and the average distance as measured with the He-Ne counting interferometer. The zero position is based on the average of the five zero

measurements. For each individual measurement the agreement between the frequency comb and the He-Ne laser counting interferometer is within 0.8 μm. When averaged over five measurements, the largest difference is 250 nm. The standard deviation doesn't show a clear distance dependence and is on average 0.33 μm. The comparison measurement shows that the mode-filtered frequency comb is a suitable tool for distance measurements, with a relative difference $< 10^{-8}$ with the He-Ne laser reading for a distance of 50 m. The observed differences between both methods for a single measurement are caused by environmental effects, like turbulence and vibrations. These effects are not perfectly canceled because of small timing differences between the simultaneous He-Ne and comb measurements. When averaging all measurements and all distances, the agreement between both methods even reduces to below 100 nm.

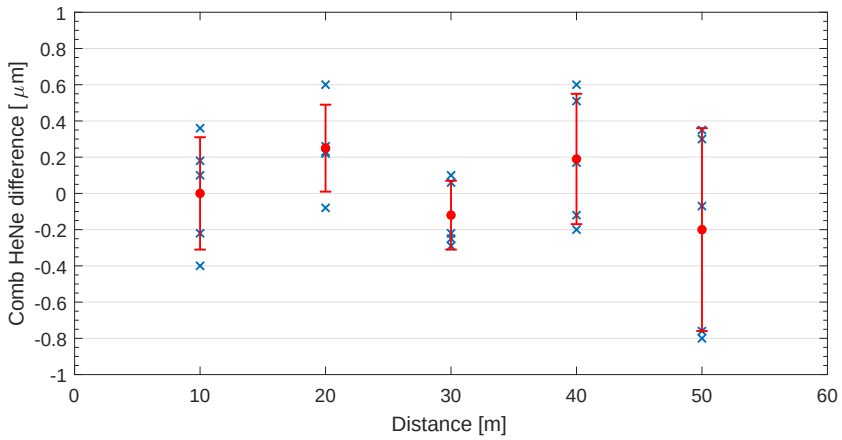

FIGURE 6.7: Measured differences between distance measurement with a filtered frequency comb and a He-Ne laser counting interferometer for distances up to 50 m. The error bars show the standard deviation of the measurements.

The measurement uncertainty on the comparison measurement contains several contributions, originating from the He-Ne uncertainty, the uncertainty on the comb measurement and the uncertainty due to environmental conditions. The relative uncertainty of the He-Ne laser, resulting from wavelength uncertainty and the fringe-counting system is estimated to be 3×10^{-9}. The uncertainty of the comb measurement contains a contribution of the frequency stability (10^{-10} for a measurement time in the ms range), plus an uncertainty of 50 nm, which comes from the uncertainty of the fitting parameter C. This contributions occurs twice, for both the start and the stop position of the carriage. The uncertainty on the refractive index *difference* for the comb and He-Ne wavelengths is estimated to be 1.7×10^{-9}. This value is based on the uncertainty in the environmental measurements, being 0.3 °C for air temperature, 7 Pa for pressure and 1.3 % for relative humidity. Finally, there is a contribution to the measurement uncertainty which results from vibrations coupling to the carriage on the measurement bench. Since the comb and He-Ne measurements have different integration times and are not perfectly synchronized, timing differences between the measurements of typically 0.1 s occur. As a result path length changes due to vibrations that occur on this time scale do not cancel. This contribution was quantified by performing a time-resolved measurement with the He-Ne laser. The He-Ne measurement shows a standard deviation of 0.22 μm for a sampling time of 0.1 s, which can be considered as the uncertainty due to vibrations

on the comparison measurement. These uncertainties occur at both the start point and the end point of the measurement, leading to a total uncertainty estimate due to vibrations of 0.31 μm. When combining the relative and absolute uncertainty contributions mentioned above as a quadratic sum, a total uncertainty of 0.36 μm for a distance of 50 m is found. For a coverage factor $k = 2$, corresponding to a 95 % coverage interval, the uncertainty equals 0.72 μm.

The uncertainty on the measurement of an absolute distance with either comb or He-Ne laser will be dominated by the uncertainty in the refractive index of air. For the uncertainties of the environmental parameters (temperature, pressure, humidity) mentioned above, the relative uncertainty on the refractive index becomes 3.1×10^{-7}. The agreement between both methods is thus much better than the achievable uncertainty on the absolute distance. Since the wavelengths of the Ti:Sapphire laser and the He-Ne laser are relatively close and the measurements arms are common path, the uncertainty due to environmental conditions largely drops out in the comparison.

As mentioned above, arbitrary distances were chosen, but path length differences very close to $L = 0$ m or $L = L_{pp}/4$ were avoided. At $L = 0$ m all wavelengths have the same phase (neglecting nonlinear air dispersion), so a typical cosine dependence like in Fig. 6.6 is not observed. Close to $L = L_{pp}/4$ the Nyquist frequency is approached and each period of the cosine is only determined by 2 datapoints. There are several ways to overcome this issue. A simple solution is to slightly changing f_{rep}, which will change L_{pp} and thus L. Alternatively, a multiplex scheme could be envisaged with two reference retro-reflectors, positioned with a mutual path length difference of about half of the non-ambiguity range. By using a beamsplitter and two shutters the reference path can be always selected such that the path length differences close to $L = 0$ m or $L = L_{pp}/4$ do not occur.

Chapter 7

All fiber filter cavity approach

This chapter briefly describes an alternative method of frequency comb mode filtering based on a single mode optical fiber cavity. The aim for the development of such a tool is its simplified implementation into an optical setup. No requirement for any mode-matching optics allows for plug-n-play by simple connecting the fiber cavity to an input and output optical fibers. Different fiber based comb mode filtering has been published, with use of a fiber coupled free space cavity [69], ring fiber resonator [70] and cascade Mach-Zhender fiber interferometer [71] or more recently a few meter long single optical fiber [72].

7.1 Fiber cavity design

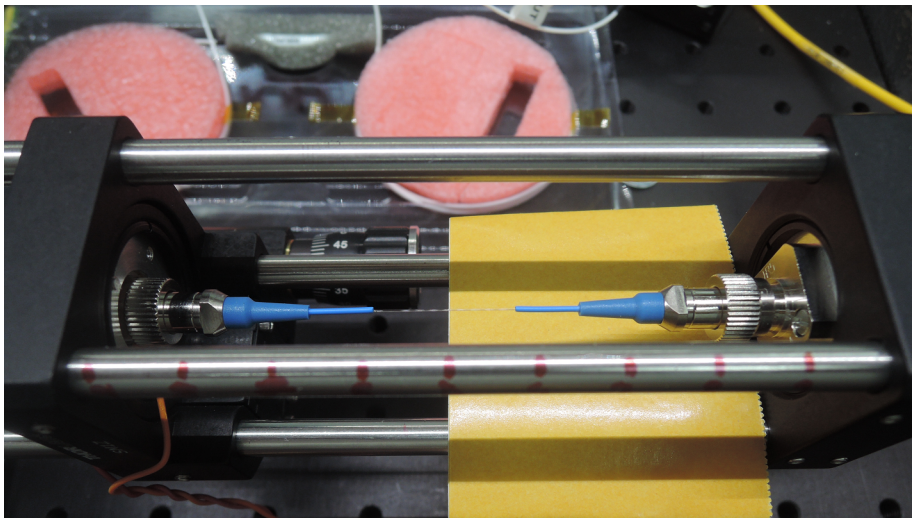

FIGURE 7.1: Picture of the experimental fiber cavity setup. An fiber optical isolator brings the light into the cavity from the left side, the output is on the right side. The piezo-equipped fiber connector is on the input side.

A principle of the construction of presented fiber cavity is the same as of a free space cavity. There are two reflecting surfaces ideally with only one transversal optical mode in between. Lateral cavity modes are tuned by changing the cavity length — an easy task for a free space cavity. In the case of an optical fiber one, changing its length is also possible since it can be stretched without any damage. The maximal amount of reversible stretching is not precisely known but approx. 0.5% of the fiber length is considered as safe.

7.1.1 Optical design

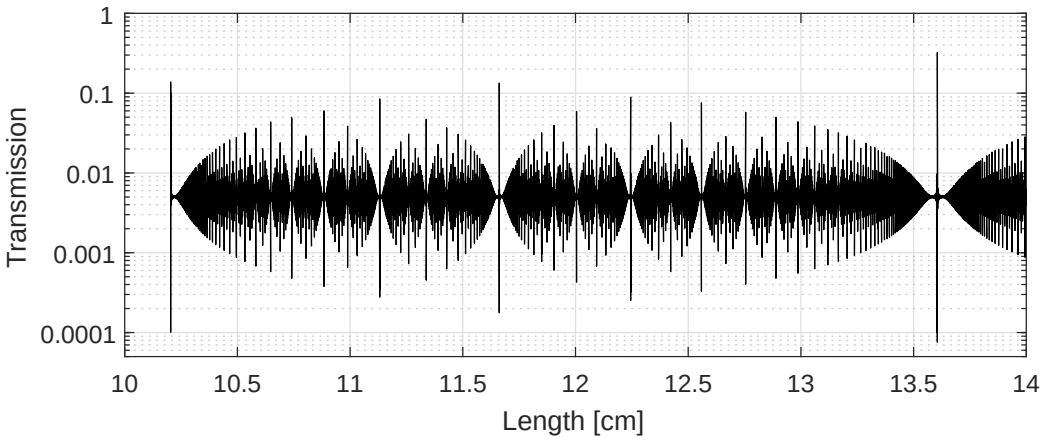

FIGURE 7.2: Silver-coated-fiber cavity transmission of a 100 MHz frequency comb as a function of length. Theoretically, infinite number of transmission envelopes is available.

The fiber cavity transmission of frequency comb modes is calculated using the method described in section 4.1.2. Although a fiber cavity cannot be stretched in order of cm, Fig. 7.2 shows data for such range in order to highlight the amount and positions of the Vernier transmission envelopes.

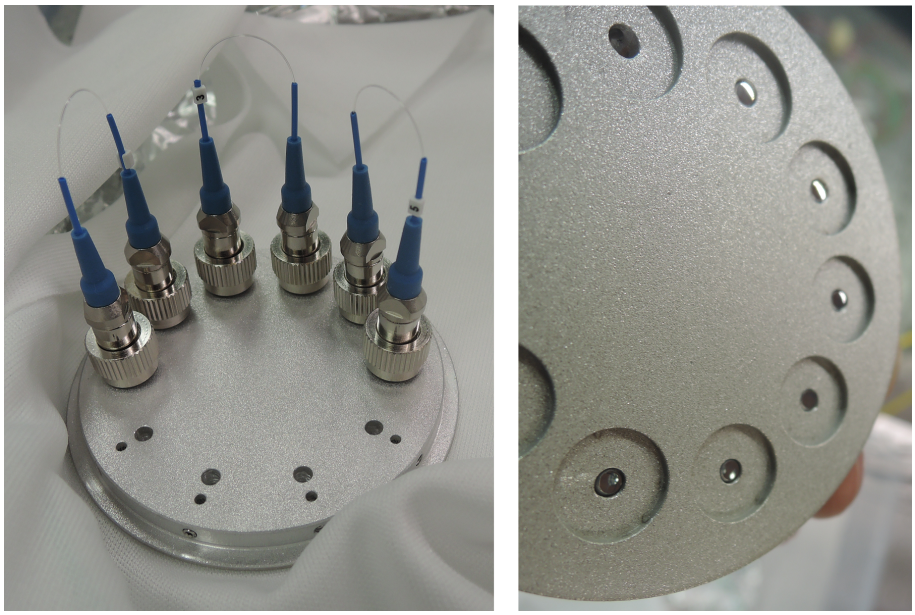

FIGURE 7.3: Fiber patchcords with length 101.8 mm mounted onto a sputtering machine adapter. Patchcord ends with finished reflective coatings are on the left image.

The first generation of a fiber cavity is designed to work with an Er^3+ fibre based frequency comb with central wavelength at 1550 nm. Its free spectral range is designed to be FSR=1 GHz. Fiber with near zero dispersion $DCF3$ from *Thorlabs* is used for fiber patchcord manufacturing. The fiber dispersion is -4.30 to -1.60 ps/nm·km and refractive index of its core is n = 1.469. The fiber length corresponding to FSR = 1 GHz is L_{fiber}=102.1 mm but the actual length of fiber patchcords is designed to

be 101.8 mm. The production process has been carried out by *SQS Vláknová Optika a.s.*, where the fiber was cut to predefined length and equipped with FC/PC type ceramic ferrules and connectors, see Fig. 7.3. Cavity mirrors are created by sputtering

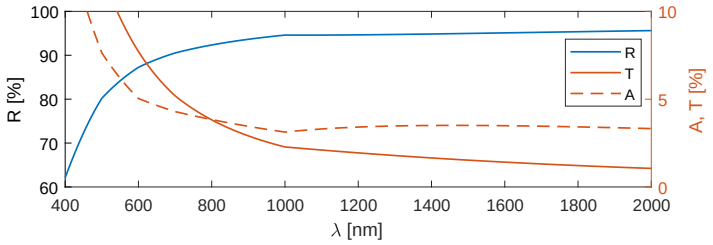

FIGURE 7.4: Optical properties of 40 nm thick Ag layer between two thick glass layers computed by *FilmStar Design* software.

of a reflective material directly on the fiber patchcord ends. Silver is chosen as the mirror material. It has zero chromatic dispersion and sufficient optical properties. A 40 nm thin layer of Ag has ∼95% reflectivity and ∼1.5%transmission, the rest of light ∼3.5% is absorbed, Fig. 7.4. Reflective layers are created by magnetron sputtering deposition at my home institute ISI Brno by the Thin Layers group.

7.1.2 Electro-mechanical design

A cage mounting system is used for holding the fiber cavity and to adjust its length, see Fig 7.1. Two standard fiber connectors are mounted to the cage, one with help of a custom made adapter, the other is attached to a manual translation mount via a custom made adapter with a ring piezochip, see Fig.7.5. The second adapter pulls the connector with a four leaf spring against the ring piezochip placed in between. In this way the fiber length can be stretched and electronically locked to a required transmission peak. The cavity length is determined by the spacing between the two fiber connectors and is stabilized with the same locking technique as the free space cavity, however using only one piezochip for both, modulation and stabilization.

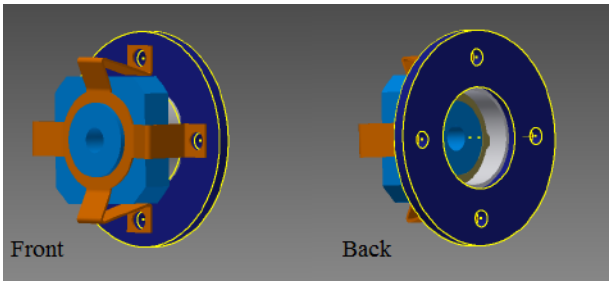

FIGURE 7.5: Schematic view of the crucial electro-mechanical part of the fiber filter cavity. The fiber connector–light blue is pulled by four leaf copper spring–orange against ring piezochip–gray. Large adapter–dark blue holds the whole system in a manual translation stage, small adapter–yellow electrically isolates the piezochip from the the fiber connector.

7.2 Results

The cavity transmission occurs for stretched fiber since its original length is designed to be 0.3 mm shorter than the length corresponding to $FSR = 1$ GHz. Coarse stretching is done manually by translations stage and fine length tuning is done by the piezochip. Working in stretched state secures possibility to shorten the cavity length if necessary. An example of the fiber cavity transmission as a function of the pizochip voltage is in figure 7.6. The cavity is scanned back and forth across three lateral transmission peaks and then is locked onto the most intense one.

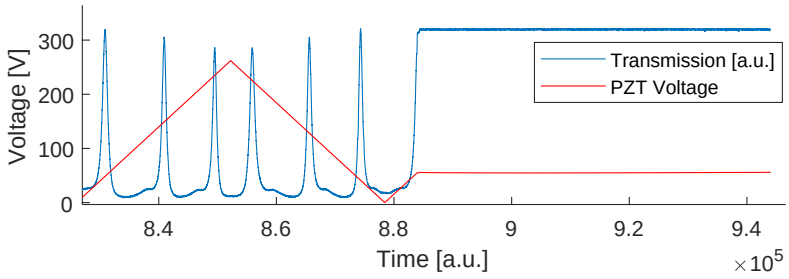

FIGURE 7.6: An example of time record of the fiber cavity transmission within an envelope as the piezo voltage is scanned and then locked.

The cavity filter properties were tested at the TU Delft, The Department of Imaging Physics. The fiber frequency comb they possess has repetition rate $f_{rep} = 100$ MHz. The cavity multiply the original f_{rep} to $m \cdot f_{rep} = 1$ GHz, in a normal configuration $i \cdot FSR = FSR$ (not Vernier, $i > 1$). The cavity comb mode filtering is observed with a TU Delft VIPA spectrometer. The VIPA spectrometer is not able to resolve modes of the fiber frequency comb. In the VIPA spectral image the modes merges into lines. However it is able to resolve less dense modes of the filtered frequency comb which are observable as dots, see figure 7.7. The presented result shows that an optical

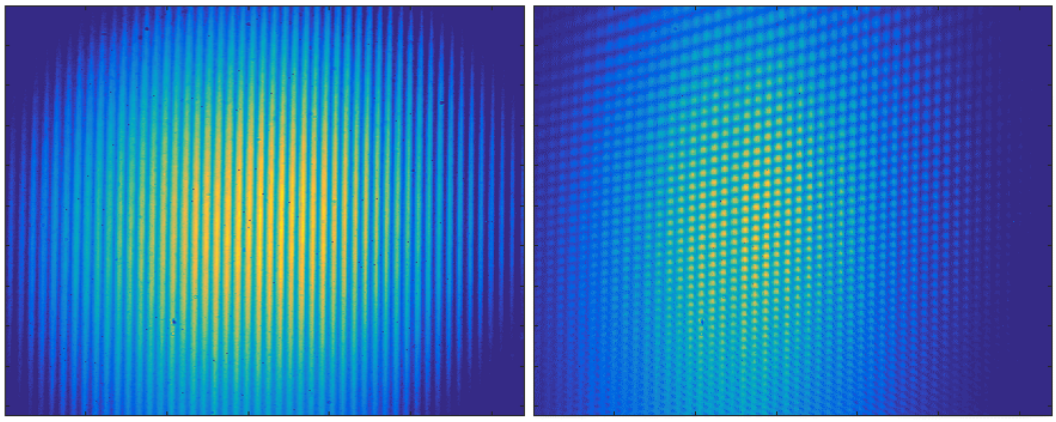

FIGURE 7.7: VIPA images for frequency comb with $f_{rep} = 100$ MHz - left and fiber cavity multiplied $f_{rep} = 1$ GHz - right.

frequency comb can be filtered by a fiber based filter cavity. Further development of this method has been started. Fiber patchords in the Vernier configurations has been designed using dielectric layers with zero chromatic dispersion and reflectivity of more than 99% instead of the silver reflective coatings. However, this second generation of the fiber cavity has to be yet properly tested.

Part II

Analysis of fluorescence from single trapped ion at frequency modulated dark state

Chapter 8

Ion trapping and interaction of an ion with external fields

The aim of the experiment discussed in the second part of the thesis is to analyse the fluorescence response of a calcium ion stored in a radio frequency trap to modulation of frequency detuning of two excitation laser fields. We are particularly interested in the characterization of fluorescence sensitivity to laser frequency detunings mediated by the ion in a dark state. This measurement is explored as a method for optical frequency analysis using the ion as a convertor of the relative optical frequency difference to the intensity of emitted fluorescence from the ion. The main goal is to provide a characterization and point out limits of this method. The dark resonance not only enhances the spectral sensitivity but, it allows for optical frequency beating of two optical fields separated by hundreds of THz, which corresponds to a frequent task in many metrological applications [32, 33, 73]. This is typically realized indirectly via an optical frequency comb. The presented method provides an alternative to these methods within limited spectral range, however the frequency comb serves here as a stable optical reference for the excitation lasers.

This chapter in the first section gives the quantum mechanical description of the $^{40}Ca^{+}$ ion and its interaction with the laser light fields, the second section describes the principles of the ion trapping in the radio frequency trap and of the ion laser cooling.

8.1 $^{40}Ca^{+}$ ion and its interaction with external fields

Calcium is an alkaline earth metal and its singly ionized ion has the energy level scheme similar to atomic hydrogen. The $^{40}Ca^{+}$ ground state is formed by the $4S$ state and the two higher orbitals D and P are split by spin-orbit coupling into four fine structure components. Levels relevant for the experiments are $D_{3/2}$ and $P_{1/2}$, their natural lifetimes are ~ 1 s respectively ~ 7 ns [74]. The ground state with these levels form a lambda system with dipole-allowed transitions $S_{1/2} \Leftrightarrow P_{1/2}$ and $D_{3/2} \Leftrightarrow P_{1/2}$ with corresponding wavelengths 397 nm and 866 nm. The diagram of five lowest energy levels is shown in Figure 8.1.

The description of an atom interacting with light fields is due to its complexity rather complicated, therefore for simplicity certain approximations are taken. The basics steps towards the calculation of atom fluorescence are discussed. Quantum mechanical model of only a three level atom is considered and its interaction with two lasers is described [75]. The atom states $|1\rangle$, $|2\rangle$ and $|3\rangle$ form a Λ system. They represent the energy levels $S_{1/2}$, $P_{1/2}$ and $D_{3/2}$. The $|3\rangle$ level is considered as a stable energy level and the spontaneous photon emission from $|2\rangle$ due to the atom interaction with the vacuum field is treated as decay rate Γ_{21} from $|2\rangle$ to $|1\rangle$ and

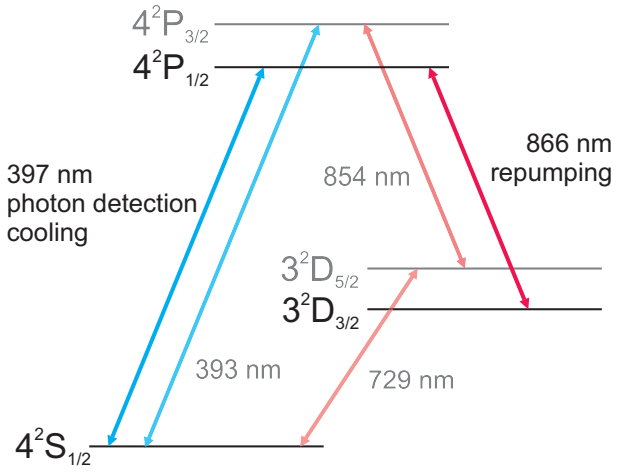

FIGURE 8.1: Scheme of the five lowest levels of $^{40}Ca^+$ with transition wavelengths and purposes of the two transitions used in presented experiment. Dashed transitions are not used.

Γ_{23} from $|2\rangle$ to $|3\rangle$. The two lasers are treated as classical coherent light waves with frequencies ω_b and ω_r, where indices indicates the *blue* - 397 nm and the *red* - 866 nm transitions:

$$\vec{E}(t) = \vec{E}_{b,r} e^{-i(\omega_{b,r} t + \varphi)}. \tag{8.1}$$

The spatial dependence of the electric field $\vec{E}$ over the ion positions $\vec{r}$ is neglected. The laser linewidths are Γ_b and Γ_r. The strength of the coupling between the atom and the electric field is described by population oscillations called Rabi frequencies:

$$\hbar\Omega_{12} = \vec{D}_{12} \cdot \vec{E}_b \tag{8.2}$$

$$\hbar\Omega_{32} = \vec{D}_{32} \cdot \vec{E}_r \tag{8.3}$$

where $\vec{D}_{12}$ and $\vec{D}_{32}$ are electric dipole matrix elements for the corresponding transitions. The strength of the excitations is also described by saturation parameters $S_r = \Omega_{32}/\Gamma_r$ and $S_b = \Omega_{12}/\Gamma_b$. The atom-light interaction is assumed to be only in the dipole order. The three state atomic Hamiltonian can be written as

$$\hat{H}_{atom} = \sum_{a=1}^{3} \hbar\omega_a |a\rangle \langle a| \tag{8.4}$$

where ω_a are atomic Bohr frequencies. The interaction Hamiltonian can be with above assumptions and with rotating wave approximation [76] written as

$$\begin{aligned} \hat{H}_{int} = &-\vec{D}_{12} \cdot \vec{E}_b i \left(|2\rangle \langle 1| e^{-i\omega_b t} - |1\rangle \langle 2| e^{i\omega_b t} \right) \\ &-\vec{D}_{32} \cdot \vec{E}_r i \left(|2\rangle \langle 3| e^{-i\omega_r t} - |3\rangle \langle 2| e^{i\omega_r t} \right). \end{aligned} \tag{8.5}$$

In matrix representation the atom Hamiltonian can be written with basis $|a\rangle$

$$\begin{pmatrix} c_1 \\ c_2 \\ c_3 \end{pmatrix} \equiv \sum_{a=1}^{3} c_a |a\rangle \tag{8.6}$$

as

$$H_{atom} = \hbar \begin{pmatrix} \omega_1 & 0 & 0 \\ 0 & \omega_2 & 0 \\ 0 & 0 & \omega_3 \end{pmatrix}. \tag{8.7}$$

Choosing the zero point energy at the level $|2\rangle$ we get

$$H_{atom} = \hbar \begin{pmatrix} \omega_1 - \omega_2 & 0 & 0 \\ 0 & 0 & 0 \\ 0 & 0 & \omega_3 - \omega_2 \end{pmatrix}. \tag{8.8}$$

The interaction Hamiltonian represented by matrix is

$$H_{int} = \hbar \begin{pmatrix} 0 & \frac{\Omega_{12}}{2} e^{+i\omega_g t} & 0 \\ \frac{\Omega_{12}}{2} e^{-i\omega_g t} & 0 & \frac{\Omega_{32}}{2} e^{-i\omega_g t} \\ 0 & \frac{\Omega_{32}}{2} e^{+i\omega_g t} & 0 \end{pmatrix} \tag{8.9}$$

and the complete Hamiltonian is

$$H = \hbar \begin{pmatrix} \omega_1 - \omega_2 & \frac{\Omega_{12}}{2} e^{+i\omega_g t} & 0 \\ \frac{\Omega_{12}}{2} e^{-i\omega_g t} & 0 & \frac{\Omega_{32}}{2} e^{-i\omega_g t} \\ 0 & \frac{\Omega_{32}}{2} e^{+i\omega_g t} & \omega_3 - \omega_2 \end{pmatrix}. \tag{8.10}$$

Density operator

To describe mixed states of the system we write the density operator $\hat{\rho}$ in the defined basis as

$$\hat{\rho} = \sum_{a,b=1}^{3} \rho_{a,b} |a\rangle \langle b|. \tag{8.11}$$

Its diagonal elements $\rho_{11} = \langle 1 |\hat{\rho}| 1\rangle$, ρ_{22} and ρ_{33} are the expectation values for finding the ion in its states $|1\rangle$, $|2\rangle$ and $|3\rangle$. The trace of the density operator $\mathrm{Tr}(\hat{\rho}) = \rho_{11} + \rho_{22} + \rho_{33} = 1$ and its diagonal elements $\langle a |\hat{\rho}| b\rangle$ represents superpositions of the states. Its time evolution is determined by the Liouville equation

$$\frac{d\hat{\rho}}{dt} = -\frac{i}{\hbar} \left[\hat{H}, \hat{\rho}\right] + \boldsymbol{L}_{damp}(\hat{\rho}), \tag{8.12}$$

where the first term represents the Schrödinger equation and the second term includes damping caused by photon decay and finite laser linewidths [77]. Its general form can be written as

$$\boldsymbol{L}_{damp}(\hat{\rho}) = -\frac{1}{2} \sum_{m} \left[\hat{C}_m^{\dagger} \hat{C}_m \hat{\rho} + \hat{\rho} \hat{C}_m^{\dagger} \hat{C}_m - 2\hat{C}_m \hat{\rho} \hat{C}_m^{\dagger}\right] \tag{8.13}$$

where operators $\hat{C}_m$ describe dissipative processes, namely decay from $|2\rangle$ to $|1\rangle$

$$\hat{C}_{12} = \sqrt{\Gamma_{12}} |1\rangle \langle 2|, \tag{8.14}$$

decay from $|2\rangle$ to $|3\rangle$

$$\hat{C}_{32} = \sqrt{\Gamma_{32}}\,|3\rangle\langle 2| \tag{8.15}$$

and decoherence by finite laser linewidths

$$\hat{C}_b = \sqrt{2\Gamma_b}\,|1\rangle\langle 1| \tag{8.16}$$

$$\hat{C}_r = \sqrt{2\Gamma_r}\,|3\rangle\langle 3|\,. \tag{8.17}$$

We can rewrite the time evolution of the density operator as

$$\frac{d\hat{\rho}}{dt} = \boldsymbol{L}\hat{\rho}\,(t) = -\frac{i}{\hbar}\left[\hat{H},\hat{\rho}\right] + \boldsymbol{L}_{damp}\,(\hat{\rho}) \tag{8.18}$$

and express it in terms of $\hat{\rho}\,(0)$ at the time t

$$\hat{\rho}\,(t) = e^{\boldsymbol{L}t}\hat{\rho}\,(0)\,. \tag{8.19}$$

Now we define a matrix of transformation into rotating frame of the laser field as

$$U = \hbar\begin{pmatrix} e^{-i\omega_b t} & 0 & 0 \\ 0 & 0 & 0 \\ 0 & 0 & e^{-i\omega_r t} \end{pmatrix}. \tag{8.20}$$

Transformed density and Hamiltonian operator are then

$$\hat{\rho}' = U\hat{\rho}U^{\dagger}. \tag{8.21}$$

$$\hat{H}' = U\hat{H}U^{\dagger} - i\hbar U\frac{dU^{\dagger}}{dt}. \tag{8.22}$$

Finally the resulting Hamiltonian is

$$H' = \hbar\begin{pmatrix} \Delta_b & \Omega_{12}/2 & 0 \\ \Omega_{12}/2 & 0 & \Omega_{32}/2 \\ 0 & \Omega_{32}/2 & \Delta_r \end{pmatrix}, \tag{8.23}$$

where the laser frequency detunings from the transition frequencies are

$$\Delta_b = \omega_b - (\omega_2 - \omega_1) \tag{8.24}$$

$$\Delta_r = \omega_r - (\omega_2 - \omega_3) \tag{8.25}$$

The Liouville equation (8.18) can be transformed into a system of linear optical Bloch equations

$$\frac{d\vec{\rho}_i}{dt} = \sum_j M_{ij}\vec{\rho}_j, \tag{8.26}$$

where $\vec{\rho}_i := (\rho_{11}, \rho_{12}, .., \rho_{32}, \rho_{33})$ and $\rho_{ab} = \langle a|\hat{\rho}|b\rangle$. The matrix M contains all information relevant for the evolution of the system and it is determined by $\boldsymbol{L}$ in Eq. (8.18). When the initial condition $\vec{\rho}\,(0)$ is given, the time evolution is

$$\vec{\rho}\,(t) = e^{Mt}\vec{\rho}\,(0)\,. \tag{8.27}$$

The normalization condition sets the trace of the density matrix to equals one

$$\sum_i \rho_{ii}(t) = 1. \tag{8.28}$$

To numerically calculate the steady-state solution $(d\rho/dt = 0)$, one of the optical Bloch equations has to be replaced by the normalization condition 8.28. The probability of finding the ion in the excited state $|2\rangle$ is then $\rho_{22} = \rho_{22}(\infty)$. The atom fluorescence at blue wavelengths i.e. average rate of atom deexcitation to the state $|1\rangle$ is

$$R_b = \Gamma_{21}\rho_{22}. \tag{8.29}$$

8.1.1 Zeeman splitting and dark resonances

Without a magnetic field each of the fine structure levels of an ion consists of $(2J+1)$ sublevels, where J is the total angular momentum of the valence electron. With a non-zero static magnetic field $\vec{B}$ applied to the ion, the degeneracy of the sublevels is lifted. Each of the sublevels is described by the magnetic quantum number m_j and its corresponding energy shift from the degenerated level is

$$\Delta E = m_j g_j \mu_B \left|\vec{B}\right| \tag{8.30}$$

where μ_B is the Bohr magnetron and g_j is the Landé g-factor. This results in the case of $^{40}Ca^+$ ion levels $S_{1/2}$, $P_{1/2}$ and $D_{3/2}$ the Zeeman splitting into an 8-level system shown in Fig. 8.2.

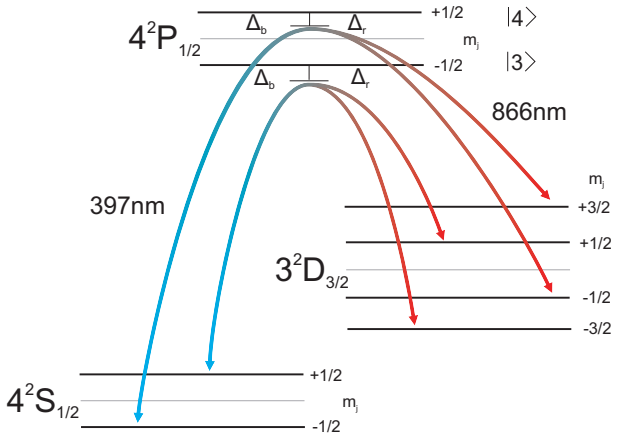

FIGURE 8.2: Scheme of $^{40}Ca^+$ three-level system splitted by magnetic field to the eight-level system. The two light fields with the polarizations perpendicular to the magnetic field leads to four coherent transitions between states $S_{1/2}$ and $D_{3/2}$ without occupation of $P_{1/2}$ states.

The model of 3-level atom-light interaction can be extended to an 8-level system, see [78]. Calculated fluorescence spectrum i.e. the stationary values of the probability of ion to be in one of the excited P states $|3\rangle$, $|4\rangle$as a function of the red laser detuning is in Fig. 8.3. When both laser detunings relative to certain Zeeman sublevels are equal

$$\Delta_r = \Delta_b \tag{8.31}$$

resonant transitions between the ground states $S_{1/2}$ and $D_{3/2}$ appears. This results in fluorescence quenching called dark resonance. In ideal case this leads to zero population of the excited state $P_{1/2}$, which corresponds to 100% population of so-called dark state. In practice, the dark state population is limited by the finite linewidth of the two involved lasers or thermal population of atomic motional states. If the angle between polarization of laser fields is chosen to be perpendicular to the magnetic field, only transitions with $\Delta m_j = \pm 1$ are coupled, which leads to excitation of four resonant Raman transitions and appearance of four dark resonances. In this case the perfect superposition of $S_{1/2}$ and $D_{3/2}$ is not perturbed by phase fluctuations of laser detunings, i.e. the common laser linewidths $\Gamma_l = \Gamma_b + \Gamma_r = 0$ and the fluorescence completely vanishes. Non-zero linewidths cause the depth of dark resonances to increases. The shape and positions of dark resonances in the fluorescence spectrum thus can be used to calculate parameters of laser and magnetic fields interacting with the trapped ion.

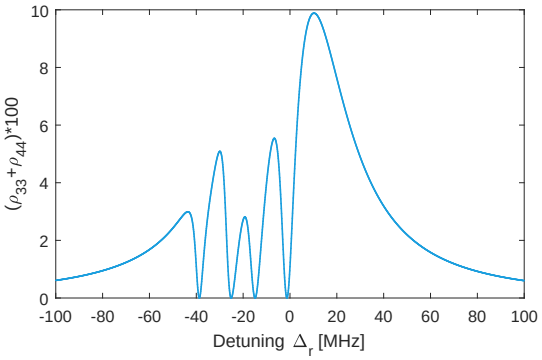

FIGURE 8.3: Resonance fluorescence or the P states occupation probability as function of frequency detuning Δ_r with corresponding Raman transitions $S_{1/2} \Leftrightarrow D_{3/2}$ manifested as four fluorescence decreases, calculated using the optical Bloch equations with parameters: the magnetic field: $\vec{B}$= 10 Gauss, the detuning of the blue laser Δ_b = -20 MHz, angle between the light fields and the magnetic field $\alpha = 90°$, saturation parameters S_b=1, S_r=4 and common linewidth of the two lasers Γ_l= 0 Hz.

8.2 Ion trapping with Paul trap

In the previous section we described the interaction of a free ion with light. This is adequate with respect to the experiments since description of ion quantum motional states is not necessary. Therefore this section briefly describes classical motion of a charged particle such as an ion in a linear Paul trap. More detailed description of the trap used in the experiments can be found in [79]. We consider geometry of the trap given in Fig 8.4. To confine the particle position in the radial x, y directions, one pair of the quadrupole electrodes is grounded while on the other pair is applied radio-frequency harmonic potential $V = V_0 \cos(\Omega_{RF} t)$. Near the trap center the potential is given by

$$V(x, y, t) = \frac{V_0}{2}\left(1 + \frac{x^2 - y^2}{r_0^2}\right)\cos(\Omega_{RF} t) \tag{8.32}$$

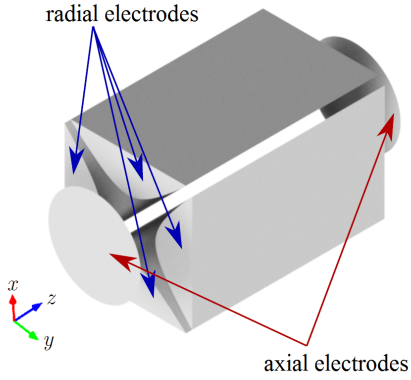

FIGURE 8.4: An example of ideal Paul trap geometry with hyperbolic-shaped radial electrodes [79].

where r_0 is half the distance between paired electrodes. To confine also particle position along the trap axial direction z a static potential U_0 is applied to the trap axial electrodes, which results to contribution

$$U(x,y,z) = \frac{\kappa U_0}{z_0^2}\left(z^2 - \frac{1}{2}\left(x^2+y^2\right)\right) \tag{8.33}$$

where κ is a geometrical constant and z_0 is $1/2$ of the distance between the endcap electrodes. The electric field near the trap center is then

$$\begin{aligned}\vec{E}(x,y,z,t) &= -\vec{\nabla}(V+U) \\ &= V_0\left(\frac{x\hat{e}_x - y\hat{e}_y}{r_0^2}\right)\cos(\Omega_{RF}t) - \frac{\kappa U_0}{z_0^2}\left(2z\hat{e}_z - x\hat{e}_x - y\hat{e}_x\right)\end{aligned} \tag{8.34}$$

where $\hat{e}_i$ $i = x,y,z$ are unit vectors. The motion of a particle with charge q, mass m and displaced from the trap center by u_i in this field can be described by Mathieu equations

$$\frac{d^2u_i}{dt^2} + u_i\left(a_i + 2q_i\cos(2\Omega_{RF}t)\right)\frac{\Omega_{RF}^2}{4} = 0 \tag{8.35}$$

where we introduced dimensionless variables

$$a_x = a_y = -\frac{1}{2}a_z = -\frac{4q\kappa U_0}{mz_0^2\Omega_{RF}^2} \tag{8.36}$$

$$q_x = -q_y = \frac{2qV_0}{mr_0^2\Omega_{RF}^2}, q_z = 0. \tag{8.37}$$

The exact solution of Eq. (8.35) can be seen in *ref.vadlej 4*, here we can approximate motion for $|a_i|, |q_i| \ll 1$ to the lowest order solution

$$u_i = u_0\cos(\omega_i t)\left(1 + \frac{q_i}{2}\cos(\Omega_{RF}t)\right). \tag{8.38}$$

The result separates the particle motion into two distinct time and amplitude scales. The fast and small motion called the *micromotion* is unharmonic motion at the trap driving frequency Ω_{RF}. Slower harmonic motion with amplitude u_0 is called the

secular motion and its frequency is

$$\omega_i = \Omega_{RF}/2\sqrt{a_i + q_i^2/2}. \tag{8.39}$$

In the rest frame of the oscillating ion, the laser field interacting with the ion appears to be frequency modulated with the trap frequencies, or equivalently from the laser point of view, the Bohr frequencies of the oscillating ion appears to have motional sidebands spaced by the trap frequencies.

8.3 Ion cooling

The spontaneous decay of the ion excited P state can be effectively used to cool down the ion motion [80]. Each emitted photon carries momentum $\vec{p}$ and since the spontaneous-emission pattern is isotropic, the net momentum given to the ion by the emitted photons is thus zero. By letting the ion to absorb photons only with momentum smaller than have the emitted ones i.e. to absorb only when the ion moves towards the photon beam, its kinetic energy is reduced. Such laser cooling techniques takes an advantage of the Doppler effect and can be divided into two categories according to the decay rate of the cooling transition Γ and frequency of the secular motion ω_i:

$\omega_i \ll \Gamma$ Doppler cooling. In this case the linewidth of the transition is much larger than the spacing of the motional sidebands or equivalently the timescale Γ^{-1} on which the ion absorb or emits photons is much faster than the timescale ω_i^{-1} on which the ion can change its kinetic energy.

$\omega_i \gg \Gamma$ Sideband cooling. The motional sideband are in this case resolvable because their spacing is much larger than the transition linewidth. The cooling laser thus can be tuned to a specific motional sideband which allows for ion cooling to the motion ground state.

For $^{40}Ca^+$ ion the Doppler cooling is performed on the $S_{1/2} \Leftrightarrow P_{3/2}$ transition by detuning the 397 nm laser to the red side from the transition frequency. For detuning by $\Gamma_b/2$, the difference of probability of absorbing the photon for the ion moving towards or away from the laser beam is maximized, and the cooling efficiency is the highest. There is 6% probability to decay from the excited state to the metastable $D_{3/2}$, thus the repumping laser at 866 nm is used simultaneously with the cooling laser [81]. The decay is however also a heating mechanism since there are random-direction momentum kicks associated with emitted photons. In steady state, where the rates for Doppler cooling and the heating due to photon emission are equal the Doppler temperature is reached:

$$T_D \approx \frac{\hbar\Gamma}{2k_B} \tag{8.40}$$

where k_B is the Boltzmann constant. T_D is the lowest temperature to which the ion can be cooled by Doppler cooling.

Chapter 9

Ion experimental setup

The experimental setup for ion trapping is newly build in the laboratories of the Institute of Scientific Instruments of CAS in Brno. On its set up cooperated colleagues from the ISI Brno and from the Department of Optic of Palacký University Olomouc. On the development of the vacuum apparatus was also involved Mesing company and the Paul trap was designed and fabricated at the University of Innsbruck. The ion setup is located in the neighboring laboratory to the laboratory equipped with a fiber optical frequency comb referenced to a hydrogen Maser. The ion lasers that needs highly stable optical frequency performance are guided with single mode optical fibers into this laboratory and here they are optically beated with the frequency comb for their phase stabilization.

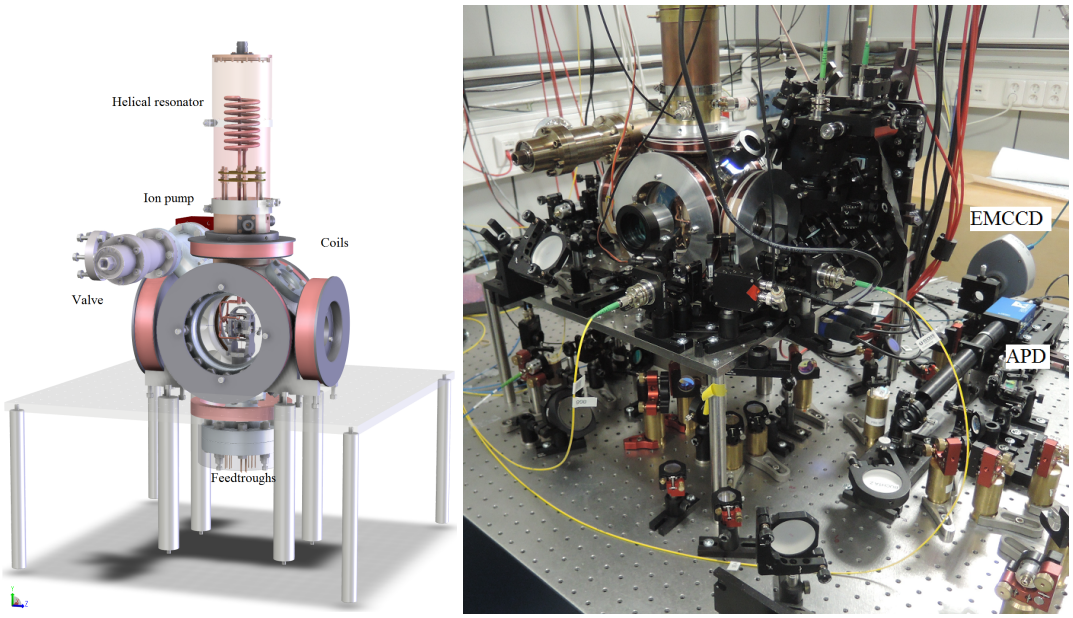

FIGURE 9.1: Scheme of the complete vacuum chamber setup with Paul trap inside – left. Snapshot of the vacuum chamber with optical components for ion interrogation – right.

9.1 Vacuum apparatus with linear Paul trap

The vacuum chamber is composed from ultra high vacuum (UHV) compatible materials and components. The body of the UHV chamber is spherical octagon with two large 100 mm and eight small 40 mm confocal flanges. The octagon with the flanges

together with a trap holder are made from low relative magnetic permeability stainless steel. The bottom flange is used for feed-throughs connecting the trap DC electrodes and for mounting the trap holder. The top flange is used for feed-through connecting trap quadrupole electrodes with a quarter wave helical resonator which amplifies resonant RF field from a frequency generator at 30.16 MHz. The input RF power before the helical resonator, usually 1-4 W, is pre-amplified by an amplifier. Two small feedthroughs at the $y = -z$ diagonal are used for vacuum management with a NEG pump and Ion pump. Both large and the four remaining small flanges are equipped with fused silica viewports with a broadband anti-reflective coating covering 397 to 870 nm range. Three Helmholtz coil pairs are placed outside the vacuum chamber around the flanges in x, y and z directions. Stabilized current sent through the selected coil pair allows for producing a nearly uniform magnetic field in the trap center and to define the quantization axis. The vacuum chamber is attached to a breadboard which lies on eight stainless steel pedestals holding it 22 cm above an optical table, see Fig. 9.1.

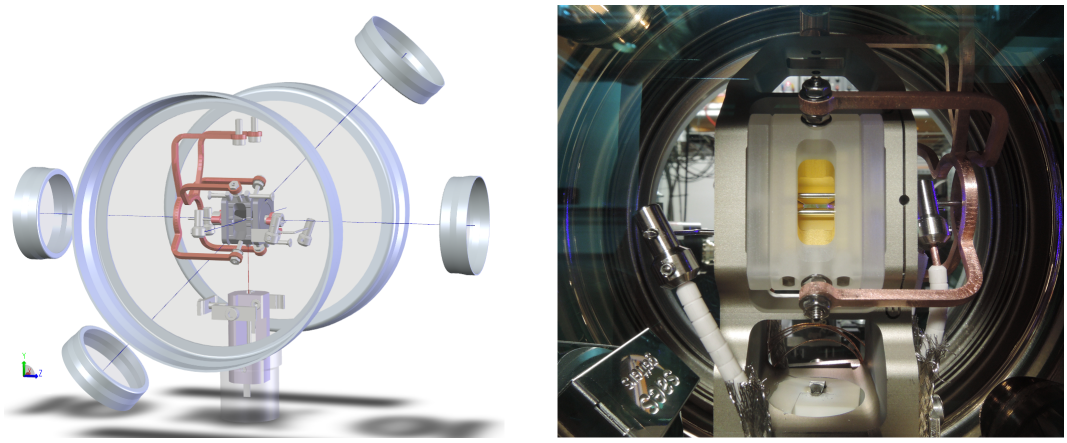

FIGURE 9.2: Front look on a scheme of the ion trap in the vacuum chamber with visible only the viewports, ion trap with electrode connections and the calcium oven. Picture on right is back side view into the vacuum chamber

The Paul trap of Innsbruck design is used [82]. It consists of six gold covered titanium electrodes, four blade-shaped electrodes are symmetrically placed in the radial plane and two ring electrodes are in the axial plane to confine the ions in this axis. The trapping pseudopotential in the radial direction is created by one pair of opposite blades kept grounded and the other pair connected to RF. The ring electrodes are held at a positive voltage and have inner diameter of 0.5 mm. Distance from the trap center to the blade electrode is 566 μm and to the ring electrode it is 2.25 mm. Additional two pairs of stainless steel rod-shaped electrodes are placed parallel to the trap axis to allow for compensation of stray electric fields. The source of calcium atoms, a resistively heated oven, is placed in the vacuum chamber below the trap. The schematic front side view of the trap with the viewports and the oven and the back side image are on Fig. 9.2.

9.1.1 Ion fluorescence detection

The light scattered by the trapped ion is detected in two ways, both filtering only on the 397 nm light by bandpass filters. The light emitted into the radial direction

of the trap towards front large viewport is gathered by an objective collecting $\sim$ 2% of the full solid angle. The light is focused towards a flip mirror which is used to select the detection way, either with a camera or with a single photon avalanche photodiode. The electron multiplying CCD (EMCCD) camera (*Luca-S, Andor*) is used for diagnostic purposes for example when ion loading and spatial analysis of the trapped ion crystal or during an optimization of the laser and the trap parameters. The free-spaced avalanche photodiode (APD) (*Count-Blue, Laser Components*) is used for delicate adjustments of the ion setup apparatus and for measurements where a photon count rate or a time of photon arrival has to be known. The APD can be connected to a frequency counter or to a fast time tagging module (*PicoHarp300, PicoQuant*) with 4 ps time resolution.

9.2 Laser setup

The trapped ions are interacting with only two laser fields during the measurements. Another two lasers are needed for calcium atom ionization. An optical fiber frequency comb is used for phase locking of the interrogation lasers. Two more lasers used for interaction with the Calcium forbidden $3D_{5/2}$ transition are also incorporated into the setup, however they are not used in the experiments thus are not described here. Except the frequency comb all the ion lasers are mounted on an optical table standing next to the table holding the vacuum apparatus. The ion lasers are directly at the laser outputs coupled to single mode optical fibers or fiber couplers. The frequency and intensity manipulation of the laser beams meant to be sent to the ion is done in free space on the same optical table, see Fig. 9.3. Transfer of all laser beams to the vacuum apparatus table is done via single mode optical fibers.

Laser	Wavelength	Application
ECDL + SHG	397 nm	Doppler cooling, fluorescence
ECDL	866 nm	Repumping
ECDL	422 nm	Photoionization
DL	377 nm	Photoionization
Optica frequency comb	600-900 nm	Phase locking

TABLE 9.1: Lasers and their corresponding wavelengths and applications.

Ionization lasers
The Ca^+ ions are loaded into the trap by evaporation of Ca atoms from the calcium oven heated by current of 4.7 A to the temperature of $\sim$ 800 K. Atoms which make their way to the center of the trap can be then photoionized in two step process. In the first step the transition $^1S_0 \leftrightarrow ^1 P_1$ at 422 nm is excited by an external cavity diode laser (ECDL), then the atom is excited above the ionization energy of 6.1 eV by a free running diode laser at 377 nm. The beams of both photoionizaton lasers are mixed by a dichroic beamsplitter at the vacuum chamber breadboard and then are focused by a lens with focal length of 150 mm into the trap center in the axial direction through a hole in the ring trap electrode. The 422 nm laser beam is split by a fiber coupler and 10% is sent through a fiber multiplexer into a wavemeter for a wavelength measurement and control.

Doppler cooling and repumping lasers
During the ion loading both cooling 794 nm and repumping 866 nm ECDLs are also

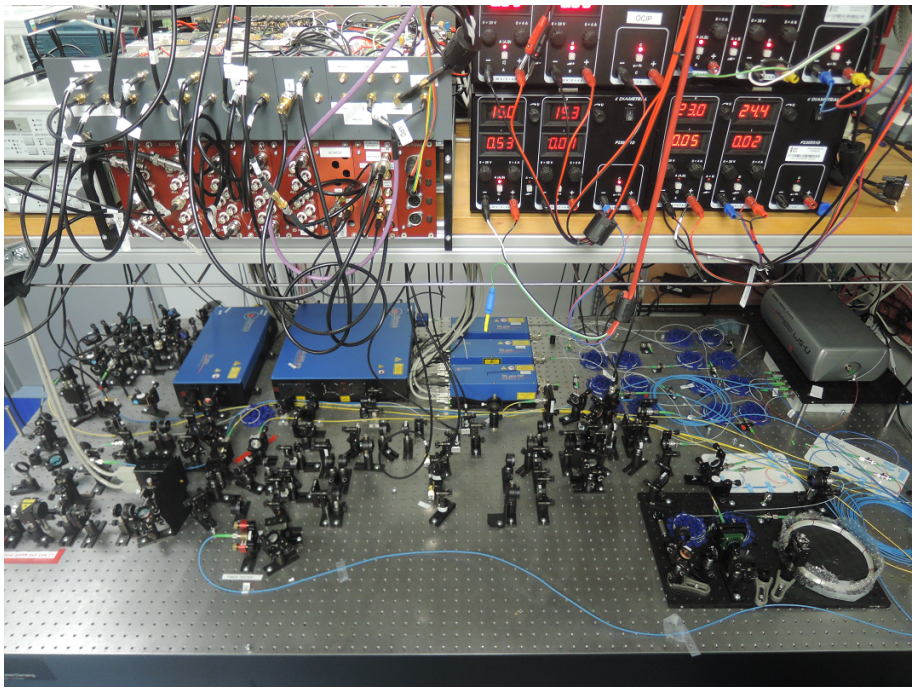

FIGURE 9.3: The optical table with ion lasers – blue boxes, frequency and intensity control optics and electronics. Lasers are from left 729 nm and 397 nm, from top 866 nm, 854 nm and 422 nm. Wavemeter–gray box is on the right side and 377 nm laser is hidden behind it.

present to start immediate ion Doppler cooling after the ionization. These lasers are polarization filtered and mixed by a dichroic beamsplitter at the vacuum chamber breadboard. Then they are focused by a lens with focal length of 150 mm into the trap center under 45° angle with respect to the trap axis and to the trap blade electrode directions. Wavelength control is done in two separate ways for both lasers, however the cooling laser is controlled at its fundamental wavelength at 794 nm. This laser unit has two output ports, one for 794 nm the other for 397 nm. The near infrared beam of this laser unit is split by a fiber coupler into two parts, one is sent to the fiber multiplexer and subsequently to the wavemeter, the other part is mixed in a 50:50 fiber coupler with 5% of 866 nm laser beam and sent to the neighboring laboratory with the optical frequency comb. The 866 nm laser is split by series of fiber couplers into three parts: 90% is dedicated to the ion, 5% to the wavemeter and 5% to the frequency comb.

The loading of the ions needs only coarse control of the 422 nm, 397 nm and 866 nm laser frequencies in a range of a few MHz. This is provided by a feedback to the piezo of the ECDL based on the wavemeter measurements. The fiber multiplexer periodically switch between the lasers and sends one beam to the wavemeter. A *LabVIEW* software calculates an error signal based on the measured laser frequency and a D/A converter generates a feedback voltage for the laser wavelength tuning.

Frequency comb

The fluorescence analysis described in this thesis requires more precise control of the 397 nm and 866 nm laser frequencies. For this reason both lasers are phase locked to a corresponding tooth of the optical frequency comb. A scheme of electronics and picture of optics for phase locking are in Fig. 9.4. The frequency comb

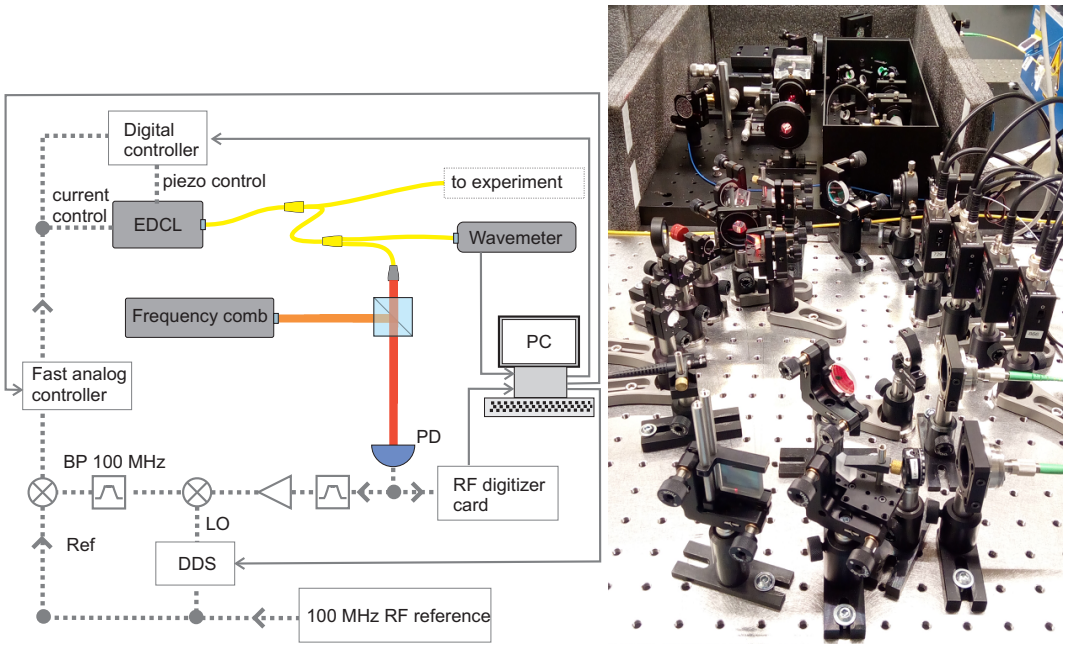

FIGURE 9.4: The Schematic view of the phase locking of an ECDL to frequency comb, however for simplicity shown only for one laser – left. The real optical part of the scheme for five lasers is shown in the picture on the right. Top of the picture shows supercontinuum generation. At the bottom is placed the diffraction grating separating mixed laser beams, which are then with mirrors on the left reflected to detectors on the right. (Only two of them are used for the experiment.)

with a center frequency at 1560 nm is frequency doubled by second harmonic generation (SHG) process in a periodically poled lithium niobate (PPLN) crystal and then broadened by a photonic crystal fiber to generate an optical supercontinuum ranging from about 600 to 900 nm. This broad spectrum is mixed with ECDL beams to create beat notes with a particular frequency comb tooth. The products of the mixing are spatially separated according to the wavelength by a diffraction grating and individually measured by a series of amplified silicone photodiodes. The frequency comb mode spacing is f_{rep} = 250 MHz, thus the beat note frequency is in usable range from 0 to 125 MHz. The beat note signal is used as an input for phase locked loop (PLL), which efficiently narrows the laser linewidth down to linewidth of a single component of the frequency comb. This method allows for stabilization of multiple lasers in near infrared and visible range to a single frequency reference within one optical setup. The two radio frequency parameters of the optical frequency comb - the repetition rate f_{rep} and the offset frequency f_{ceo} are referenced to the hydrogen maser, which is for the long-term stability disciplined by a GPS clock. Particular beat note signal between the comb tooth and the laser is amplified, filtered and mixed with a local oscillator (LO). This LO is generated by a direct digital synthesizer (DDS) referenced to the hydrogen maser, and has the value of the desired beat note frequency raised by 100 MHz. After bandpass filtering, the product of mixing is mixed once more with 100 MHz reference signal to generate a DC signal which has the phase information of the comb-laser beat note and serves as the error signal for laser phase-locked loop (PLL). The PLL is realized with fast analog control electronics. The target frequency of atomic transition is achieved by a fine

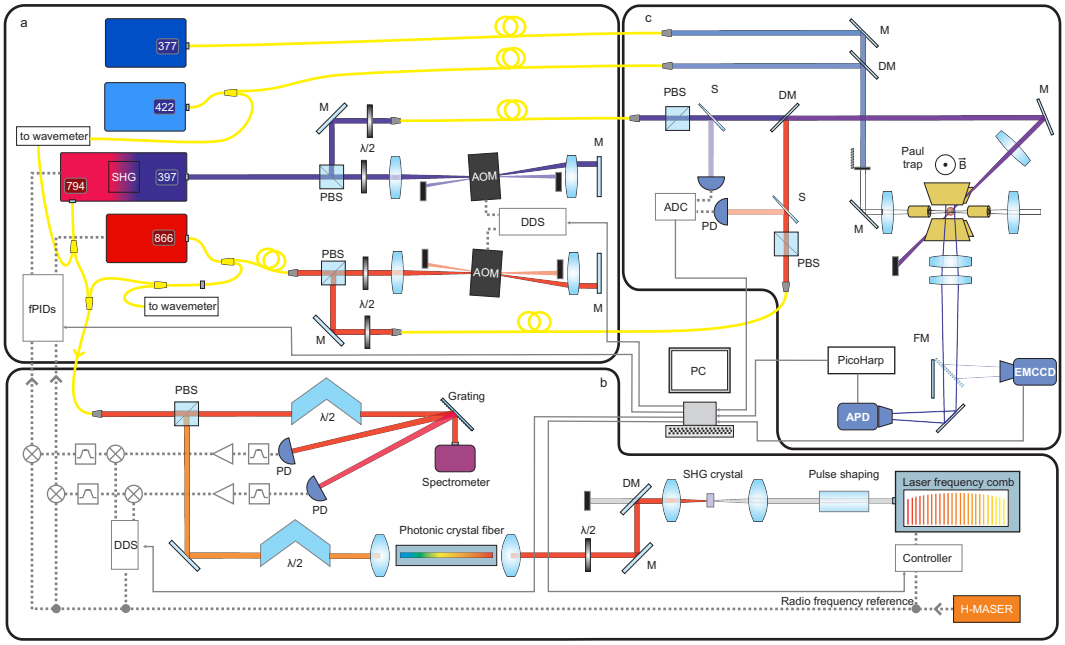

FIGURE 9.5: Scheme of the experimental setup distributed over three optical tables corresponding to parts a), b), c). All ion ECDLs are placed on table a). The cooling laser beam is generated by frequency doubling the 794 nm to 397 nm. The near infrared laser beams are send through an optical fiber to table b) where the optical frequency comb supercontinuum is optically mixed with lasers by use of broadband optical elements and the products are spatially separated for beat note detection. Individual beat notes are after filtering and amplification used for generating the control signals for frequency stabilization of the lasers. The 397 nm and 866 nm laser beams dedicated to the ion are led into AOMs in the double pass configuration for frequency and amplitude modulation and then sent to the ion trap positioned on the optical table c). The laser fields are set to particular desired polarization and are amplitude-monitored at the proximity of the ion chamber. The ionization laser are send directly to the ion only with 422 nm wavemeter-based control. A beam shutter blocks the ionization lasers after successful loading of desired number of ions. The ion fluorescence is collected by a lens with Numerical aperture of 0.2 and detected by the EMCCD camera or single photon avalanche photdiode. The detection signals including precise photon arrival times are recorded using fast time-tagging module or converted by an analog-digital card (ADC) for further processing.

frequency tuning with an AOM in double pass configuration. These AOMs are also used for amplitude stabilization of the laser intensities. An overview of the experimental setup is shown in Fig. 9.5. It is separated to the tree optical tables dedicated to the ion lasers, frequency comb and laser beating and the table with the ion trap.

Chapter 10

Analysis of fluorescence of ion at modulated dark state

This chapter describes measurements of fluorescence response of a single trapped $^{40}Ca^{+}$ ion at a dark state to optical frequency modulation of an excitation laser. The spectral sensitivity of the ion fluorescence is enhanced in the vicinity of dark resonance. The frequency modulation corresponds to the modulation of the dark state population, which results in fluorescence modulation along the spectral feature of dark resonance. This method is explored here as a method for optical frequency analysis using the Fourier analysis of the recorded modulated fluorescence.

A continuous measurement scheme on a $^{40}Ca^{+}$ ion with the transitions $4S_{1/2} \leftrightarrow 4P_{1/2}$ and $4P_{1/2} \leftrightarrow 3D_{3/2}$ excited by two lasers fields at wavelengths 397 nm and 866 nm is implemented. The 397 nm laser is also used for simultaneous Doppler cooling, while 866 nm repumps the ion from a long lived $3D_{3/2}$ manifold. Both lasers are phase locked to teeth of a fiber frequency comb referenced to a hydrogen maser. In this way they adopt known frequency linewidths and stability of the optical reference, which allows for precise calibration of the optical frequency analysis by deterministic modulation of the analyzed laser beam with respect to the reference beam. For this purpose, the repumping laser serves as an analyzed field to which a deterministic frequency modulation is applied, while the cooling laser is the reference field with fixed frequency. Properties of the presented scheme are analyzed in terms of the fluorescence response to imposed laser frequency characteristics, namely frequency deviation A and modulation frequency f_m [83].

In the first section of this chapter, the measurement principles of this method and a simple theoretical model of the fluorescence signal-to-noise ratio are described. The second section compares the theoretical model with measured fluorescence responses to a range of modulation frequencies and amplitudes and the final section presents the results in terms of the limits of the method.

10.1 Features of the measurements

10.1.1 Measurement configuration

The trapped and Doppler cooled ion is simultaneously driven by two laser fields at 397 nm and 866 nm. The target frequencies of atomic transition are achieved by fine frequency tuning with AOMs in double pass configuration as shown in Fig. 9.5. The beams are combined by a dichroic mirror and brought through a lens into the vacuum chamber and to the linear Paul trap with 45° angle relative to the trap axis. The ion is trapped in the radial x, y directions by harmonically oscillating electric field at frequency 31 MHz with amplitude corresponding to the radial secular motion frequency $f_{x,y} \approx 1.66$ MHz. The axial position is confined by voltage of $U_{tip} =$

500 V applied at trap tips, leading to the axial secular frequency $f_z \approx 780$ kHz. The magnetic field of 6.1 Gauss is applied at the position of the ion to lift the degeneracy of the Zeeman states, which results in effective internal energy level scheme with eight states, see Fig. 10.1*a*). The angle between polarization of the laser fields is chosen to be perpendicular to the magnetic field, therefore only transitions with $\Delta m_j = \pm 1$ are excited, which allows for efficient depopulation of the outermost states from the $3D_{3/2}$ manifold and leads to the observation of four dark resonances. From the observable four resonances, one corresponding to transition between electronic states $|S_{1/2}, -1/2\rangle$ and $|D_{3/2}, -1/2\rangle$ is selected since it is the closest one to global fluorescence maximum and has the longest resonance slope.

Fluorescence from the ion is collected in the direction of the magnetic field using objective lens with numerical aperture of 0.2 and focused onto the free spaced APD, with the overall detection efficiency of single photons emitted by the ion estimated as 0.15 %. Time tags of photon detections are recorded with fast time tagging module.

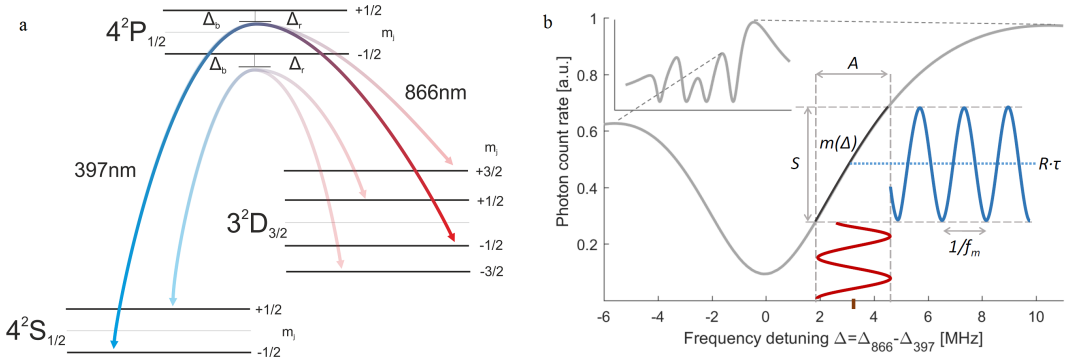

FIGURE 10.1: Scheme a) shows the employed energy level scheme of $^{40}Ca^+$. The two laser fields with polarizations perpendicular to the magnetic field lead to observation of four dark states between $S_{1/2}$ and $D_{3/2}$ manifolds. Scheme b) shows a simulation of the $P_{1/2}$ level occupation probability proportional to fluorescence intensity as a function of 866 nm laser frequency detuning Δ_{866}. Detailed zoom in the selected dark resonance depicts the fundamental parameters determining the performance of the spectral analysis including the detuning Δ_{866}, frequency deviation of the frequency modulation A, modulation frequency f_m, conversion through the slope with parameter m onto the fluorescence with average photon count rate per second R_s and measured with an APD gate time τ.

Tuning the 866 nm laser to a position at a slope of particular dark resonance, described by a slope parameter $m(\Delta_{866})$ representing the resonance gradient, allows to use the ion as a direct frequency deviation to fluorescence intensity convertor due to its high and quasi-linear dependence, see Fig. 10.1*b*) for schematic explanation.

10.1.2 Fluorescence spectra with phase locked ECDLs

To measure ion fluorescence dynamic response to the frequency detuning of the excitation lasers, it is necessary to narrow the linewidths and stabilize the frequencies of the lasers to the levels where they not interfere with the measurements as it is described in section 9.2. In this way the laser linewidths efficiently adopts linewidths of the frequency comb modes. The laser frequencies written in terms of the comb frequencies are then: $\nu_{866} = 2(n_{2\cdot866} f_{rep} + f_0) + f_b$ and $\nu_{397} = 2[2(n_{2\cdot794} f_{rep} + f_0) + f_b]$.

The frequency difference between lasers as seen by the ion is then $\Delta\nu = (4n_{2\cdot794} - 2n_{2\cdot866})f_{rep} + 2f_0 + f_{b794} - f_{b866}$, where $4n_{2\cdot794} - 2n_{2\cdot866}$ =1635856. Standard deviation of the comb RF frequencies are $\sigma(f_{rep})$= 1 mHz and $\sigma(f_0)$ < 1 Hz (100 s averaging time), which indicates standard deviation of laser frequency detuning below 1 Hz. We have measured linewidth of single comb tooth by beating it with a laser at 1540 nm with linewidth at the level of a few Hz and obtained FWHM = 40 kHz with 1 kHz resolution bandwidth setting. The main contribution to this linewidth comes from the f_0 and the f_{rep} contribution can be neglected. After each SHG process the linewidth is also doubled, however, since the noise source is common for both 397 nm and 866 nm lasers, a simple estimation of their mutual linewidth based on $\Delta\nu$ leads to 80 kHz. Figure 10.2 illustrates the enhancement of the dark resonance

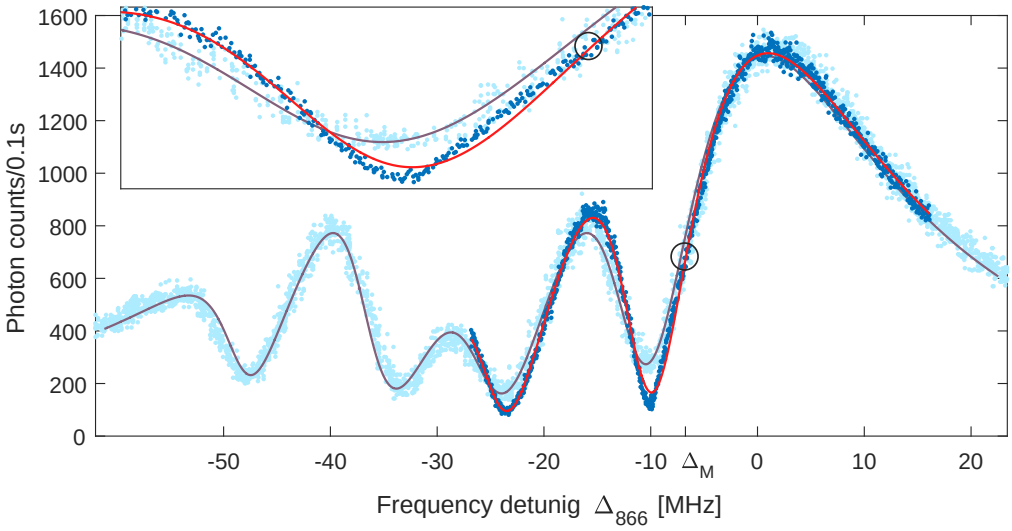

FIGURE 10.2: Dark blue fluorescence spectrum measured with both lasers phase-locked to the frequency comb with limited bandwidth due to PLL limited scanning range. Red line is the optical fit and black circle corresponds to the measurement point. Parameters of the fit are the magnetic field $\vec{B}$ = 6.1 Gauss, the detuning of the blue laser from the degenerate transition Δ_{397} = -16 MHz, angle between the light fields and the magnetic field α = 90°, saturation parameters S_{397} = 1, S_{866} = 4 and combined linewidth of the two lasers Γ =124 kHz.Light blue is fluorescence spectrum with all dark resonances visible, measured by scanning of free running 866 nm laser monitored by wavemeter. Purple line is its fit with the only parameter significantly different from the PPL scan being the lasers combined linewidth Γ = 250 kHz. The insertion shows the lower part of the resonance with the measurement point. Difference in the resonance depth for the two spectra is clearly visible. The shape of the PLL resonance also does not perfectly fit to the theory .

contrast and slope steepness by utilization of frequency stabilization of 397 nm and 866 nm lasers to the frequency comb. At this locking configuration the fluorescence spectrum is measured, however in narrow bandwidth limited by the PLL frequency scanning range of f_{beat} from 0 to 125 MHz. The whole spectrum containing all dark resonances is measured again, but with 866 nm laser frequency controlled utilizing only the wavemeter-based feedback. Both fluorescence spectra are fitted with the optical Bloch equations. A measurement point Δ_M is chosen in the middle of

the quasi-linear slope of the dark resonance, because this maximizes the measurable amplitudes of modulation. The slope parameter for the linear approximation is for all measurements at this measurement point $m(\Delta_M)$ = 1.78 counts·s^{-1}·kHz^{-1}, with corresponding photon count rate per second R_s = 6800 cps. The frequency detunings of the analyzed and reference lasers from their corresponding transition frequencies are Δ_{866} = -7 MHz and Δ_{397}= -10 MHz, respectively. The fits of optical Bloch equations to the measurements does not perfectly follows the measured florescence curve. Particularly at the measurement point Δ_M its gradient corresponds to $m_{Bloch}(\Delta_M)$ = 2.21 counts·s^{-1}·kHz^{-1}, which is 24% above the gradient of a numerical fit. For this reason, we use instead of the optical fit a polynomial fit as the slope function m_{nl}, as will be explained in the next section. The optical fit parameters are: the magnetic field $\vec{B}$ = 6.1 Gauss, the detuning of the blue laser from the degenerate transition Δ_{397} = -16 MHz, angle between the light fields and the magnetic field α = 90°, saturation parameters S_{397} = 1, S_{866} = 4 and combined linewidth of the two lasers Γ = 250 kHz and Γ =124 kHz for the PLL spectrum.

10.1.3 Fluorescence signal-to-noise ratio

The frequency spectrum of the analyzed 866 nm laser deviations is measured by keeping the reference 397 nm laser at constant detuning Δ_{397} and modulating the frequency detuning $\Delta_{866}(t)$. To determine the dynamic response of the ion as a detector of mutual frequency shifts of the two lasers, a controlled frequency modulation is introduced to the system followed by fluorescence signal processing. The modulation is applied to the 866 repumping laser as harmonic frequency modulation with specific modulation frequency f_m and peak frequency deviation A (frequency deviation). The modulation results in a periodic signal on fluorescence, which can be considered as harmonic due to quasi-linearity of the slope close to our modulation point Δ_M.

The fluorescence is recorded as arrival times of detected photons with 4 ps time resolution. This time tag record is processed by a *Matlab* script to data of photon count rate in units of number of photon counts per time bin τ (gate time). To determine the theoretical response function of the detected fluorescence to the introduced frequency modulation a natural fluorescence noise is compared to the observable signal in the evaluated frequency spectrum. Equation for the fluorescence signal-to-noise ratio SNR is derived as the ratio of function describing the amplitude of harmonically modulated fluorescence $S(f_m, A, \tau)$ to the amplitude of fluorescence noise $N(R, T, \tau)$. The signal part of the function converts 866 nm laser frequency deviation A to amplitude of fluorescence harmonic signal $S(f_m, A, \tau)$ according to the dark resonance slope parameter $m(\Delta_{866})$, modulation frequency f_m and the gate time τ. Although not necessary, a linear approximation of the slope parameter can simplify the evaluation and is defined as

$$m = \delta(\langle n \rangle \cdot s^{-1}) / \delta\Delta_{866} \tag{10.1}$$

at measurement detuning point Δ_{866}, where <n>·s^{-}1 is an average number of detected photons per second. In case of $(1/f_m) \ll \tau$ and the linear approximation of the slope parameter m, the fluorescence signal amplitude can be approximated as $S(f_m, A, \tau) \approx mA\tau$. The modulation frequency f_m and gate time τ affects effective fluorescence modulation amplitude A_{eff} by averaging the fluorescence over gate time τ.

$$A_{eff} = \frac{1}{\tau} \left| \int_0^{\tau} A \cos(f_m \tau) dt \right| = A \left| \mathrm{sinc}(f_m \tau) \right| \tag{10.2}$$

Then the amplitude S of the imposed signal is

$$S = mA\tau \left|\mathrm{sinc}(f_m\tau)\right|. \tag{10.3}$$

The SNR can be found by comparing the signal to the fluorescence noise amplitude without modulation. In ideal case, when noise contributions from laser and magnetic fields are negligible, noise of fluorescence emitted by ion corresponds to shot noise due to small overall detection efficiency. The amplitude of noise is then shot noise of average photon count rate over number of measurement samples $n_s = T/\tau$,

$$N = \sqrt{\frac{R\tau}{T}}, \tag{10.4}$$

where $R =< n > /\tau$ is the average count rate per gate time τ, and T is the measurement time. R_s symbol is used elsewhere in the text for photon count rate per one second. The SNR can be then expressed as

$$SNR = \frac{S}{N} = \sqrt{\frac{T}{R\tau}}mA\tau \left|\mathrm{sinc}(f_m\tau)\right|. \tag{10.5}$$

In case of large frequency deviations ($A \approx$ hundreds of kHz) it is important to include a function, which numerically gives a true response of the observable fluorescence rate to the relative frequency detuning of analyzed laser Δ_{866}. The nonlinear slope function $m_{nl}(\Delta_M)$ is taken from a polynomial fit of measured fluorescence spectrum around the measurement point. To obtain the signal amplitude, modulation amplitude factor mA is replaced with half of the fluorescence difference at the two extremes of modulated detuning frequency Δ_M + A and Δ_M - A. This yields

$$SNR = \frac{1}{2}\sqrt{\frac{T}{R\tau}}\sum_n \left[p_n\left(\Delta_M + A\right)^{n-1} - p_n\left(\Delta_M - A\right)^{n-1}\right]\left|\mathrm{sinc}(f_m\tau)\right|. \tag{10.6}$$

where p_n are coefficients of nth degree polynomial fit $m_{nl}(\Delta_M)$. An example of measured fluorescence data used for further fluorescence analysis are in Fig. 10.3 for two values of frequency deviation A = 0 and 300 kHz.

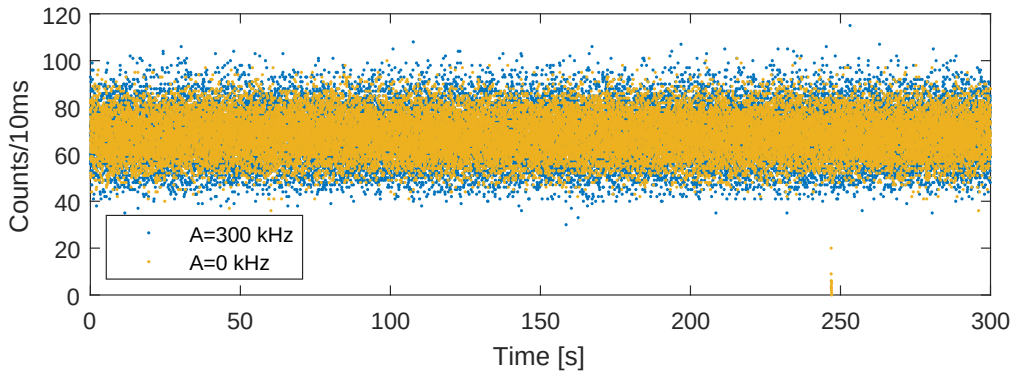

FIGURE 10.3: Ion fluorescence record at measurement point Δ_M for modulated and stable laser frequency detuning Δ_{866}. Modulation frequency is f_m = 12 Hz, gate time τ = 10 ms. Notice a drop-out at T $\sim$ 250 s.

10.2 Measurements of fluorescence response

The measurements of fluorescence response are done for various sets of modulation frequencies f_m, frequency deviations A, measurement time T and also measurement points Δ_M. The goal is not attempt to cover whole accessible modulation frequency spectral range and modulation depths, but rather illustrate the working mechanism of the presented scheme and show its intrinsic limits. A fluorescence time tag measurement is processed into set fluorescence data in units of photon counts per τ, where τ has values from a certain range simulating a variable gate time or sampling frequency $FS = 1/\tau$ of a photodetector. These data are then individually analyzed in terms of their frequency spectrum evaluated by the FFT algorithm. The values of signal-to-noise ratio are then $SNR = S_{meas}/N_{meas}$, where S_{meas} is the frequency component at the modulation frequency f_m (or component with maximal amplitude) and N_{meas} is the average amplitude of the whole FFT spectrum. The natural unmodulated fluorescence has Poissonian distribution, thus its spectrum has the character of white noise and can be averaged as a whole. The minimum of τ is chosen such that $\mathrm{sinc}(f_m\tau) > 0.99$ and the maximum is chosen always much higher than $1/f_m$. The data processing ca be summed as:
Time tag data $\Rightarrow$ Set of count rate data $\Rightarrow$ Set of FFT spectra $\Rightarrow$ Set of $SNR(\tau)$
This process is used for all the measurements except the measurements with variable measurement point Δ_M, where the SNR is calculated for values of τ for which condition $\mathrm{sinc}(f_m, \tau) > 0.99$ is fulfilled.

For gate time lower than the period corresponding to modulation frequency f_m, the modulation component is aliased in the spectrum at aliased frequencies $f_{alias} = |b \cdot FS/2 - f_m|$, where folding factor b is the closest even integer of ratio $2f_m/FS$. Any periodic signal, analyzed by FFT, will suffer from spectral leaking, if its length is not an integer multiply of $1/f_m$ [84]. To prevent this, and consequent decrease of signal amplitude, all measured data are shortened by a few ms to match the measurement time frame with frequency modulation periodicity. This method is preferred over using a window function, since the measurements are made with single modulation frequency. Relatively low photon count rate theoretically does not place any fundamental limit on detectable modulation frequency. When sampling frequency is chosen much higher than count rate (counts/s), most of the gate time bins contains zero counts and the rest contains one or more counts. The information about frequency modulation is still preserved even when the average number of counts per bin is below one and it is obtained from the modulation of photon counts in the time bins. Note, that this should not be confused with frequency detuning out of dark resonance slope, e.g. detuning into the bottom of the dark resonance where count rate could eventually drop to zero. As mentioned above, the slope function m_{nl} is defined in certain region of count rate (2000 counts$\cdot$s^{-1} to 15000 counts$\cdot$ s^{-1}). This boundaries obviously scale with the gate time. A control if fluorescence has not crossed these boundaries, due to e.g. laser-locking dropout or ion vacuum impurity kick, has been made for all measurements at τ = 10 ms. Dropouts in shorter time scales are considered negligible.

The results of frequency response measurements are summarized in four figures. Three of them emphasize the $SNR(\tau)$ dependence on the critical measurement and evaluation parameters, in particular: modulation frequency, frequency deviation, and measurement time with respect to the gate time τ. The last figure compares the $SNR(\Delta_M)$ for two modulation frequencies with respect to the measurement point Δ_M which corresponds to different values of count rate R_s and slope parameter m.

10.2.1 Modulation frequency

From the frequency point of view, $SNR(f_m, \tau)$ data from five measurements with varying modulation frequencies and constant frequency deviation are compared in Fig. 10.4. This evaluates the frequency bandwidth of the presented method. The total length of all measurements is T = 300 s and the frequency deviation is set to A = 300 kHz to be well within the employed resonance slope. The range of modulation frequencies is from f_m = 66, to 120 kHz. The analysis shows high attainable SNR in the whole measured spectral range. The observed $SNR(f_m, \tau)$ ratios are well reproduced by the theoretical predictions of equation 10.6 up to high modulation frequencies comparable or higher than count rate of the measurements of 6800 cps. For the two highest f_m of 66 and 120 kHz, values of $SNR(f_m, \tau)$ follows the predicted shape of the theoretical predictions, with respect to τ, but have values lower than theory.

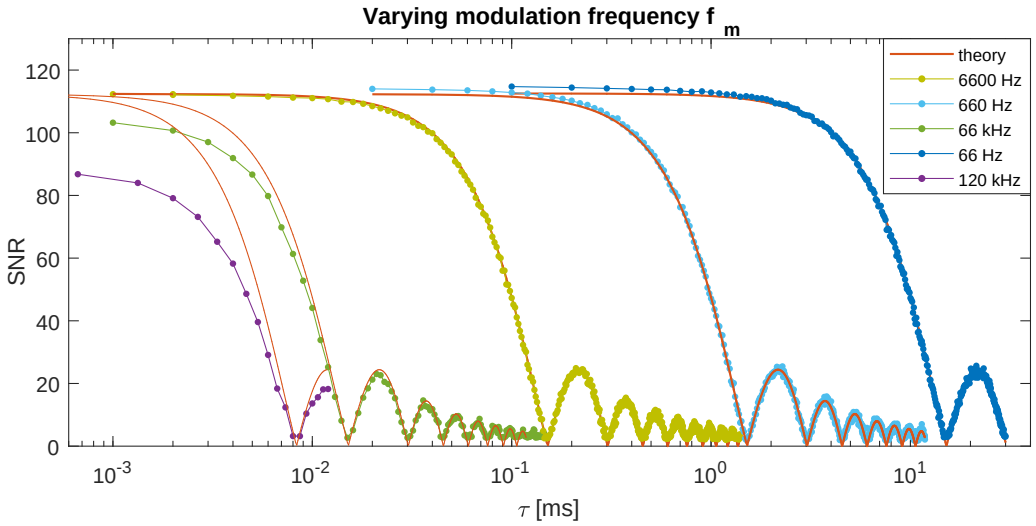

FIGURE 10.4: signal-to-noise data for five 300 s long measurements of the fluorescence with modulated detuning Δ866. Frequency deviation is kept at 300 kHz and modulation frequency varies (dots). Red lines are theoretical signal-to-noise ratio calculated using nonlinear slope function $m_n l$. Note that mean time between two successive photon detections is $\sim$ 0.15 ms.

10.2.2 Frequency deviation

The potential of the presented spectrometry method with respect to capturing the frequency deviation A is explored within this measurement case. The SNR dependence on the frequency deviation A is measured for low modulation frequency f_m = 66Hz to avoid any effect of fast modulation on the observability of high modulation amplitudes. The expectable upper limit will be given by the spectral width of the dark resonance slope, while the lowest detectable frequency deviations will depend on the amount of the detection noise. Equivalently, the lowest detectable signal in the frequency spectrum has its limit given by frequency amplitudes of shot noise. This detectable limit is defined here as variable SNR_{lim}. The limit is obtained by simulating data of shot noise with Poissonian distribution. The simulated data represents pure fluorescence without modulation and have the same count rate R and

measurement length T as the real data. This simulated fluorescence is analyzed in the same way as the measured data: $SNR_{shotnoise}$ is calculated, with exception that the signal part S is obtained as the highest amplitude component of its whole frequency spectrum without the DC component. 500 simulations of shot noise data and an average of corresponding values of $SNR_{shotnoise}$ is used for estimation of the detection limit $SNR_{lim}(\tau) = < SNR_{shotnoise}(\tau) >_{500}$. This limit can be also roughly viewed as the ratio of 3σ confidence interval of amplitude distribution in the pure shot noise frequency spectrum with its mean value N. Obtaining amplitudes from particular frequency positions f_m or f_{alias} in the frequency spectrum is the reason why there are visible "sinc" fringes even below the limit of SNR_{lim}, as can be seen in Fig. 10.5.

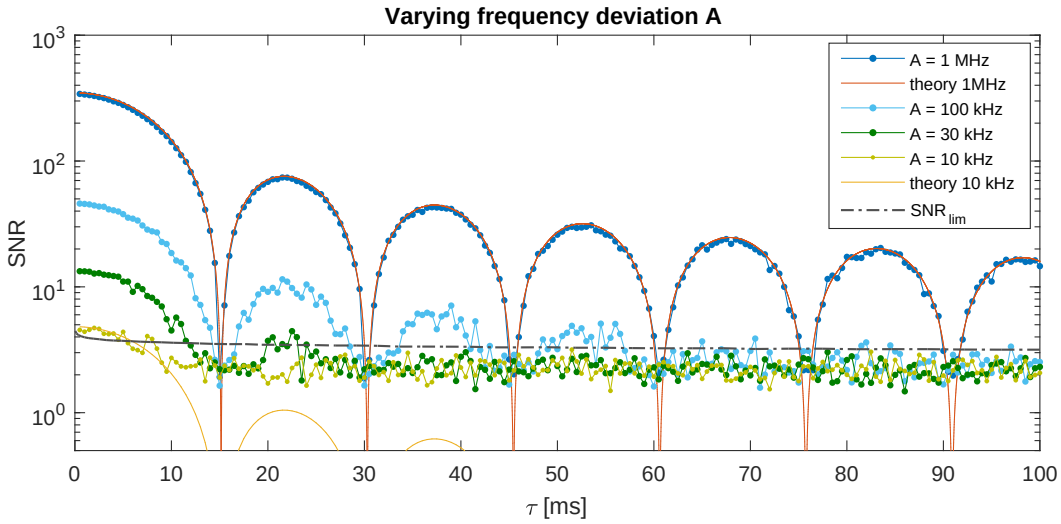

FIGURE 10.5: signal-to-noise measurements of fluorescence with harmonically modulated detuning of analyzed laser field Δ_{866} with modulation frequency set to 66 Hz. The measured data for different frequency deviations are shown with dots with lines. Full lines show the theoretical simulation of SNR for the highest and lowest frequency deviations, respectively. Dash-dotted gray line represents a numerical limit given by pure signal with Poisson distribution evaluated as maximal amplitude of shot noise. Amplitude levels for signals are taken from known frequency position in the spectrum, thus the fringe pattern is slightly visible even below the limit.

10.2.3 Measurement time

For a general task of estimation of amplitude of unknown frequency components, the whole frequency spectrum has to be searched, not only positions of f_m or f_{alias}, and thus there is always a spectral component with amplitude at least on the level of SNR_{lim}. I.e. if there is an unknown frequency, it is possible to detect it, only if its amplitude is higher than SNR_{lim}. Figure 10.6 shows two measurements with f_m = 66 Hz, A = 300 kHz and measurement times T equal to 3 and 300 s. Corresponding $SNR(T, \tau)$ data follows theoretical curves in all regions above the SNR_{lim} limit curve. The figure also shows the effect of the measurement length T on the observed $SNR(T, \tau)$ and also on the limit SNR_{lim}. The limit is not constant and actually increases with measurement time T – as there is higher probability for a higher noise

amplitude in a longer measurements. For the two measurements and 1 ms gate time the lowest detectable SNR corresponds to the levels of SNR_{lim}(3 s,1 ms) = 3.16 respectively SNR_{lim}(300 s,1 ms) = 3.97. The rise of SNR_{lim} is compensated by decrease of noise mean vale N_{meas}. This ensures higher SNR and better detection sensitivity for longer measurements.

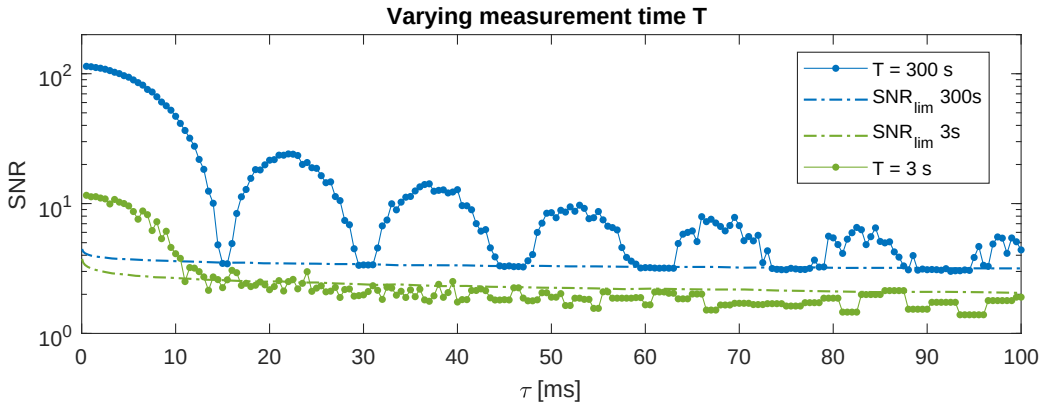

FIGURE 10.6: SNR data for 3 s and 300 s long measurement of fluorescence with harmonically modulated laser detuning Δ_{866}. Modulation frequency and frequency deviation are fixed to 66 Hz and 300 kHz, respectively. The signal amplitudes are found as the maximum of whole frequency spectrum except the DC component. The dots show the measured data, dashed lines represent numerical limits given by simulated fluorescence with Poisson distribution SNR_{lim}.

10.2.4 Measurement point

The reciprocal dependence of the SNR on the count rate R is shown by measuring at different measurement points in the vicinity of the dark resonance. Scan of the measurement points is shown in Fig. 10.7. Measurements of $SNR(R)$ for two modulation frequencies f_m = 12 Hz and 120 kHz with A = 300 kHz are realized along the dark resonance spectrum by changing the detuning frequency Δ_{866}. Gate time τ is chosen such that $\mathrm{sinc}(f_m, \tau) > 0.99$, thus it does not affect the fluorescence response. At each measurement point the average SNR of ten measurements with T = 10 s are compared with theoretical SNR values for whole dark resonance calculated using the slope parameter m directly obtained from measured fluorescence scan. Furthermore the ratio between the measured SNR of the two f_m sets shows that for the set with $f_m > R_s$ there is a decrease of SNR proportional to $\sim 1/R_s$.

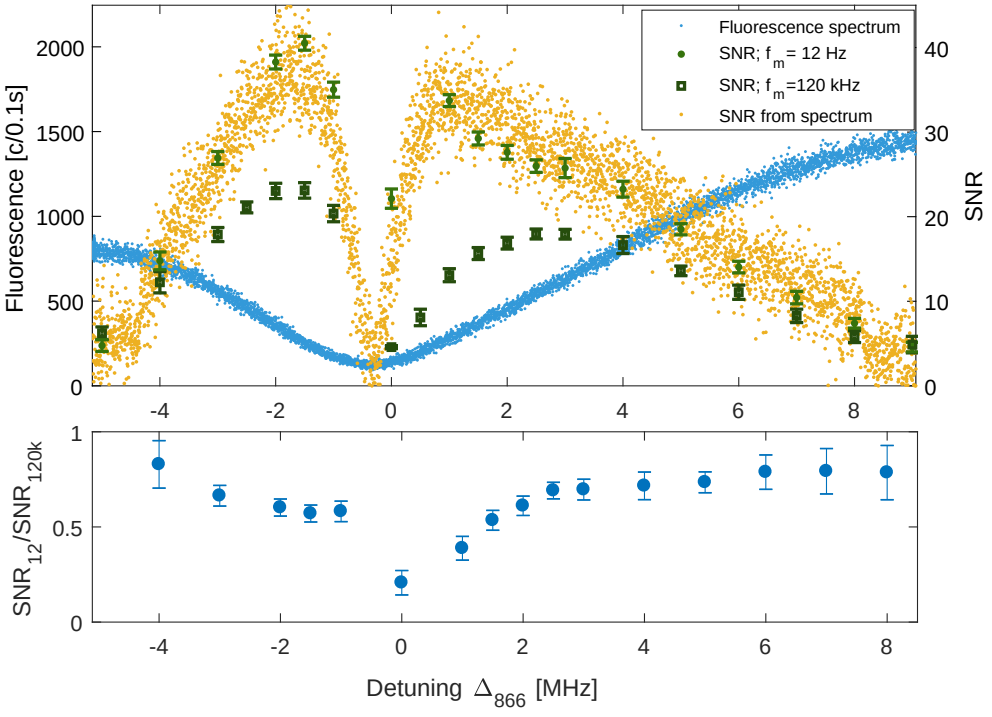

FIGURE 10.7: Upper graph shows theoretical data of SNR (orange dots) calculated on basis of measured fluorescence spectrum. Average SNR of ten measurements with T = 10 for two modulation frequencies 12 Hz (green circle) and 120 kHz (green square) are measured along the dark resonance. Errorbars corresponds to two standard deviations. Ratio between measured SNR for the two f_m data sets is shown on the lower graph.

10.3 Results and discussion

The results of presented measurements are interpreted in here in terms of fundamental limits of the proposed method. Fluorescence sensitivity to frequency deviation A is given by the slope function of the dark resonance m, which depends on the parameters of applied magnetic and laser fields. The measurement point used for the measurements with variables A, T and f_m is no worse (in terms of fluorescence gradient) than $1/2$ of the steepest slope of any dark resonance achievable by tuning the parameters of applied fields to the ion. It however stands on the slope, whose length in the axis of frequency detuning, has been set by the parameters to $\sim$ 8 MHz. This gives a fundamental upper limit of the presented method on the optical frequency bandwidth which does not cause 866 nm laser to detune out of the resonance slope. The width of the employed dark resonance slope and the measurement position on the slope thus limits the frequency deviation and modulation frequency. According to the Carson rule for frequency modulation bandwidth with 98% of modulation energy [85, 86], combined frequency deviation A and modulation frequency f_m has to satisfy condition $2(A + f_m)$ = 8MHz. This condition is well satisfied in the measurements. The smallest detectable modulation amplitudes are given by fluorescence noise at given photon count rate and total length of the measurement. This limit is defined as SNR_{lim} and corresponds to ratio of maximal amplitude in a pure shot noise frequency spectrum with its mean value N. Scale up in the measurement time

T leads to raise of the SNR_{lim} limit value, however the mean level of amplitudes of shot noise frequency spectrum N is proportional to $\sqrt{R\tau/T}$, thus the lowest detectable frequency deviation can be scaled down with longer measurement times or by measuring in the lower part of the resonance slope with smaller photon count rates. Specifically for measurement at point Δ_M with the linear slope parameter m = 1.78 cps/kHz, count rate R_s = 6800 cps, measurement time T = 300 s, gate time τ = 1 ms and modulation frequency f_m = 66 Hz, the limit of detectable frequency deviation is $A_m in$ = 2 kHz.

Detectable modulation frequency is according to the presented theory in Eq. (10.6) unlimited, however, the presented measurements show decrease of $SNR(f_m, \tau)$ for high modulation frequencies. In our particular case, the decrease has been observed for modulation frequencies on the order comparable to photon count rate R_s, where signals start to be undersampled. Comparisons of SNR for two modulation frequencies f_m = 12 Hz and f_m = 120 kHz along the dark resonance indicate correlation of the decrease with fluorescence intensity, however the theoretical simulation of modulated fluorescence shows that the undersampling itself should not limit the observable modulation frequency detection bandwidth. Simulation results did not show any decrease of SNR, even for the order of magnitude higher modulation frequencies then what was observed with the same photon rate. Other possible effects, including leaking of the spectral modulation sidebands out of the resonance slope or the frequency response of the AOM were also investigated and do not explain the observable decrease of SNR. The bandwidth of spectral modulation sidebands is given by the Carson rule, as described earlier. The response of the AOM was measured up to modulation frequency f_m = 1 MHz, but we measured flat response. At this point we thus leave the attainable frequency bandwidth limit of the presented method for further investigation, including studies of possible excitation of first or higher order motional sidebands within the employed Raman excitation scheme might play a role.

The sensitivity of the fluorescence to frequency detuning can be further improved. First option is to increase the fluorescence detection efficiency, which has been in our case mostly limited by the numerical aperture of the collection optics to 0.15% of the total emission rate. The other option is to increase the number of trapped ions. Both options will linearly enhance fluorescence intensity and thus also the steepness of the dark resonance slope.

Chapter 11

Conclusion

In the first part of this thesis I have demonstrated that long distances can be measured with high accuracy using a mode-filtered frequency comb and a simple linear array spectrometer based on a diffraction grating. In comparison to a HeNe laser a relative agreement below 10^{-8} has been shown. The method of cavity mode filtering opens up the possibility to use a low repetition rate frequency comb, like a fiber comb, for many-wavelength homodyne interferometry. Since fiber combs are smaller, easier to operate and less sensitive to the environment than Ti:Sapphire-based combs, this could be of interest for potential field applications of this method using fiber combs. When using a filter cavity to generate repetition rates of several 10s of GHz, it is possible to replace the complicated VIPA spectrometer with a linear array spectrometer. This not only simplifies the experimental setup, it also simplifies data processing and analysis.

The filter cavity constructed for the purpose of the distance measurements has been designed to work in a Vernier configuration, which allows for a large tuning of filter ratio with fractional change of the cavity length. This also enables to obtain high repetition rates of hundreds of GHz with relatively large cavity lengths, which simplifies its construction. Even easier operation of a filter cavity has been investigated using all fiber approach. A fiber filter cavity has been designed and constructed to work with fiber frequency combs at 1550 nm. The performance of the silver coated fiber cavity to multiply f_{rep} from 0.1 to 1 GHz was successfully tested using the VIPA spectrometer.

In general, the availability of frequency combs having a mode spacing that is sufficiently large to be resolved by an array spectrometer, will be a step forward towards practical applications of many-wavelength homodyne interferometry for absolute distance measurement.

In the second part of this thesis I have used a frequency comb as the optical reference for investigation of a method of optical frequency analysis using fluorescence emitted from a single Doppler cooled $^{40}Ca^{+}$ ion trapped in a Paul trap. The method is based on enhanced fluorescence sensitivity to optical frequency fluctuations due to the probing of the ion close to a dark state in a lambda-like three level system. The ion's dark resonance represents a convertor of the relative optical frequency difference to the intensity of fluorescence. The characterization of this method has been carried out by deterministic modulation of relative frequency detuning of the two excitation laser at 397 and 866 nm which have been phase locked to the frequency comb. In this way they adopt known frequency linewidths and stability of the optical reference.

For the analysis of the ion fluorescence response to the laser frequency modulation a simple theoretical model of fluorescence signal-to-noise ratio has been developed. Its comparison with signal-to-noise data obtained by the Fourier analysis of

measured fluorescence showed a good agreement, however also certain limits of this method have been identified. I have shown that for applied measurement settings, the fundamental upper limit for optical frequency bandwidth is 8 Mhz and the lowest detectable laser frequency deviation is 2 kHz. The comparison of the theory with the presented measurements have also shown a decrease of the signal-to-noise ratio for modulation frequencies on magnitudes higher than the photon count rate. The measurements also showed a correlation of the decrease with fluorescence intensity, however I have not proved that the signal undersampling is the cause. Other possible effects have been also investigated and do not explain the observable decrease of signal-to-noise ratio, thus I had left the attainable frequency bandwidth limit of the presented method for further investigation.

The presented feasible bandwidths, which are in good agreement with theoretical model, can be further improved by increasing the fluorescence detection efficiency or by increasing the number of trapped ions, what would also led to improved sensitivity of the fluorescence to frequency deviations.

Appendix A

Distance measurement data

c	299792458 m/s										
f_rep	1,0115191 GHz		Lambda_synt		0,005292472 m						
f_filter	56										
	n_phase (633)	n_group (820 nm)		L_laser (vacuum)	Corrected for sign (m)	Corrected for n: physical distance (m)	Phase		L_phase (m)	Integer times Lpp	Ln (m)
pos0_10	1,000274207	1,000277269		0,0001	0,0000001	9,99726E-08		8,34	0,000317051	0	0,000317051
pos10	1,000274486	1,000277551		10016,06022	10,01606022	10,01331171	6,552515817		0,000403738	3785	10,01362826
	1,000274486	1,000277551		10016,06022	10,01606022	10,01331171	6,549668981		0,000403914	3785	10,01362844
	1,000274486	1,000277551		10016,06022	10,01606022	10,01331171	6,543120589		0,000404318	3785	10,01362884
	1,000274486	1,000277551		10016,06022	10,01606022	10,01331171	6,544508705		0,000404232	3785	10,01362876
	1,000274486	1,000277551		10016,06022	10,01606022	10,01331171	6,540260062		0,000404495	3785	10,01362902
pos0_20	1,000274186	1,000277247		-0,0616	0,0000616	6,15831E-05		6,99	0,000378381	0	0,000378381
pos20	1,00027455	1,00027762		-20090,3345	20,0903345	20,08482012	5,415759929		0,000488482	7592	20,08513717
	1,00027455	1,00027762		-20090,3342	20,0903342	20,08481982	5,41525014		0,000488528	7592	20,08513722
	1,00027455	1,00027762		-20090,3344	20,0903344	20,08482002	5,417145482		0,000488357	7592	20,08513705
	1,00027455	1,00027762		-20090,3345	20,0903345	20,08482012	5,419466775		0,000488148	7592	20,08513684
	1,00027455	1,00027762		-20090,3346	20,0903346	20,08482022	5,415102468		0,000488541	7592	20,08513723
pos0_30	1,000274119	1,000277179		-0,0921	0,0000921	9,20748E-05		6,47	0,000408712	0	0,000408712
pos30	1,000274541	1,000277606		30034,9216	30,0349216	30,02667805	4,806547948		0,000550395	11350	30,02699479
	1,000274541	1,000277606		30034,9228	30,0349228	30,02667925	4,799508804		0,000551203	11350	30,02699559
	1,000274541	1,000277606		30034,9231	30,0349231	30,02667955	4,793803885		0,000551859	11350	30,02699625
	1,000274541	1,000277606		30034,9234	30,0349234	30,02667985	4,793604553		0,000551882	11350	30,02699627
	1,000274541	1,000277606		30034,9235	30,0349235	30,02667995	4,793044674		0,000551946	11350	30,02699634
pos0_40	1,000274084	1,000277144		0,0666	0,0000666	6,65818E-05		6,91	0,000383072	0	0,000383072
pos40	1,000274556	1,000277622		40040,2166	40,0402166	40,02922632	5,789239915		0,000456969	15131	40,02954269
	1,000274556	1,000277622		40040,2168	40,0402168	40,02922652	5,787732391		0,000457088	15131	40,02954281
	1,000274556	1,000277622		40040,217	40,040217	40,02922672	5,780516747		0,000457658	15131	40,02954338
	1,000274556	1,000277622		40040,2168	40,0402168	40,02922652	5,778670559		0,000457805	15131	40,02954353
	1,000274556	1,000277622		40040,2163	40,0402163	40,02922602	5,783865981		0,000457393	15131	40,02954311
pos0_50	1,000274033	1,000277093		0,066	0,000066	6,59819E-05		6,92	0,000382502	0	0,000382502
pos50	1,000274573	1,000277639		50021,7804	50,0217804	50,00804954	5,888862232		0,000449238	18903	50,0083664
	1,000274573	1,000277639		50021,781	50,021781	50,00805013	5,886404914		0,000449426	18903	50,00836659
	1,000274573	1,000277639		50021,782	50,021782	50,00805113	5,882898049		0,000449694	18903	50,00836686
	1,000274573	1,000277639		50021,7822	50,0217822	50,00805133	5,87986058		0,000449926	18903	50,00836709
	1,000274573	1,000277639		50021,7817	50,0217817	50,00805083	5,87249731		0,00045049	18903	50,00836765
pos0_0	1,000273987	1,000277046		0,06678	0,00006678	6,67617E-05		6,90	0,000383395	0	0,000383395

Relative to zero measured before long displacement					Relative to zero measured after long displacement					Average over both directions	
comb displacement (m)	HeNe displacement (m)	comb minus Hene (micrometer)	Average Deviation micrometer or relati	std. Dev micrometer and relative:	comb displacement (m)	HeNe displacement (m)	comb minus Hene (micrometer)	Average Deviation micrometer or relati	std. Dev micrometer relative:	comb minus Hene (micrometer)	Relative difference
10,0133112	10,0133116	-0,40	0,00	0,31	10,0132499	10,0132501	-0,24	0,16	0,31	0,08	8,1E-09
10,0133114	10,0133116	-0,22			10,0132501	10,0132501	-0,07				
10,0133118	10,0133116	0,18	relative:	relative:	10,0132505	10,0132501	0,34	relative:	relative:		
10,0133117	10,0133116	0,10	4,9E-10	3,1E-08	10,0132504	10,0132501	0,25	1,6E-08	3,1E-08		
10,0133120	10,0133116	0,36			10,0132506	10,0132501	0,51				
20,0847588	20,0847585	0,26	0,25	0,24	20,0847285	20,0847280	0,42	0,41	0,24	0,33	1,6E-08
20,0847588	20,0847582	0,60			20,0847285	20,0847277	0,76				
20,0847587	20,0847584	0,23	relative:	relative:	20,0847283	20,0847279	0,39	relative:	relative:		
20,0847585	20,0847585	-0,08	1,2E-08	1,2E-08	20,0847281	20,0847280	0,08	2,0E-08	1,2E-08		
20,0847588	20,0847586	0,22			20,0847285	20,0847281	0,38				
30,0265861	30,0265860	0,10	-0,12	0,19	30,0266117	30,0266115	0,25	0,03	0,19	-0,05	-1,5E-09
30,0265869	30,0265872	-0,29			30,0266125	30,0266127	-0,15				
30,0265875	30,0265875	0,06	relative:	relative:	30,0266132	30,0266130	0,21	relative:	relative:		
30,0265876	30,0265878	-0,22	-4,0E-09	6,2E-09	30,0266132	30,0266133	-0,07	9,1E-10	6,2E-09		
30,0265876	30,0265879	-0,25			30,0266133	30,0266134	-0,10				
40,0291596	40,0291597	-0,12	0,19	0,36	40,0291602	40,0291603	-0,15	0,16	0,36	0,18	4,4E-09
40,0291597	40,0291599	-0,20			40,0291603	40,0291605	-0,23				
40,0291603	40,0291601	0,17	relative:	relative:	40,0291609	40,0291607	0,14	relative:	relative:		
40,0291605	40,0291599	0,51	4,8E-09	9,1E-09	40,0291610	40,0291605	0,48	4,1E-09	9,1E-09		
40,0291600	40,0291594	0,60			40,0291606	40,0291600	0,57				
50,0079839	50,0079836	0,35	-0,20	0,56	50,0079830	50,0079828	0,23	-0,31	0,56	-0,25	-5,1E-09
50,0079841	50,0079842	-0,07			50,0079832	50,0079834	-0,18				
50,0079844	50,0079852	-0,80	relative:	relative:	50,0079835	50,0079844	-0,91	relative:	relative:		
50,0079846	50,0079854	-0,76	-3,9E-09	1,1E-08	50,0079837	50,0079846	-0,88	-6,2E-09	1,1E-08		
50,0079852	50,0079849	0,30			50,0079843	50,0079841	0,19				
			average difference over all distances					**average difference over all distances**		**average difference over all measurements**	
			25 nm					**89 nm**		**57 nm**	
			1,9,E-09 relative					**7,0,E-09 relative**		**4,4,E-09 relative**	

References

[1] Yves Salvade et al. “High-accuracy absolute distance measurement using frequency comb referenced multiwavelength source”. In: *APPLIED OPTICS* 47.14 (2008), 2715–2720. ISSN: 1559-128X. DOI: 10.1364/AO.47.002715.

[2] Sangwon Hyun et al. “Absolute length measurement with the frequency comb of a femtosecond laser”. In: *MEASUREMENT SCIENCE AND TECHNOLOGY* 20.9 (2009). ISSN: 0957-0233. DOI: 10.1088/0957-0233/20/9/095302.

[3] K Minoshima and H Matsumoto. “High-accuracy measurement of 240-m distance in an optical tunnel by use of a compact femtosecond laser”. In: *APPLIED OPTICS* 39.30 (2000), 5512–5517. ISSN: 1559-128X. DOI: 10.1364/AO.39.005512.

[4] J Ye. “Absolute measurement of a long, arbitrary distance to less than an optical fringe”. English. In: *OPTICS LETTERS* 29.10 (2004), 1153–1155. ISSN: 0146-9592. DOI: 10.1364/OL.29.001153.

[5] M. Cui et al. “High-accuracy long-distance measurements in air with a frequency comb laser”. In: *OPTICS LETTERS* 34.13 (2009), 1982–1984. ISSN: 0146-9592. DOI: 10.1364/OL.34.001982.

[6] Dong Wei et al. “Time-of-flight method using multiple pulse train interference as a time recorder”. English. In: *OPTICS EXPRESS* 19.6 (2011), 4881–4889. ISSN: 1094-4087. DOI: 10.1364/OE.19.004881.

[7] Petr Balling et al. “Femtosecond frequency comb based distance measurement in air”. In: *OPTICS EXPRESS* 17.11 (2009), 9300–9313. ISSN: 1094-4087. DOI: 10.1364/OE.17.009300.

[8] Joohyung Lee et al. “Time-of-flight measurement with femtosecond light pulses”. In: *NATURE PHOTONICS* 4.10 (2010), 716–720. ISSN: 1749-4885. DOI: 10.1038/NPHOTON.2010.175.

[9] Ki-Nam Joo and Seung-Woo Kim. “Absolute distance measurement by dispersive interferometry using a femtosecond pulse laser”. In: *OPTICS EXPRESS* 14.13 (2006), 5954–5960. ISSN: 1094-4087. DOI: 10.1364/OE.14.005954.

[10] S. A. van den Berg et al. “Many-Wavelength Interferometry with Thousands of Lasers for Absolute Distance Measurement”. In: *PHYSICAL REVIEW LETTERS* 108.18 (2012). ISSN: 0031-9007. DOI: 10.1103/PhysRevLett.108.183901.

[11] I. Coddington et al. “Rapid and precise absolute distance measurements at long range”. In: *NATURE PHOTONICS* 3.6 (2009), 351–356. ISSN: 1749-4885. DOI: 10.1038/NPHOTON.2009.94.

[12] Joohyung Lee et al. “Absolute distance measurement by dual-comb interferometry with adjustable synthetic wavelength”. In: *MEASUREMENT SCIENCE AND TECHNOLOGY* 24.4 (2013). ISSN: 0957-0233. DOI: 10.1088/0957-0233/24/4/045201.

[13] Steven A. van den Berg, Sjoerd van Eldik, and Nandini Bhattacharya. "Mode-resolved frequency comb interferometry for high-accuracy long distance measurement". English. In: *SCIENTIFIC REPORTS* 5 (2015). ISSN: 2045-2322. DOI: 10.1038/srep14661.

[14] M. J. Thorpe and J. Ye. "Cavity-enhanced direct frequency comb spectroscopy". In: *APPLIED PHYSICS B-LASERS AND OPTICS* 91.3-4 (2008), 397–414. ISSN: 0946-2171. DOI: 10.1007/s00340-008-3019-1.

[15] M. T. Murphy et al. "High-precision wavelength calibration of astronomical spectrographs with laser frequency combs". In: *MONTHLY NOTICES OF THE ROYAL ASTRONOMICAL SOCIETY* 380.2 (2007), 839–847. ISSN: 0035-8711. DOI: 10.1111/j.1365-2966.2007.12147.x.

[16] T. Steinmetz et al. "Fabry-Perot filter cavities for wide-spaced frequency combs with large spectral bandwidth". In: *APPLIED PHYSICS B-LASERS AND OPTICS* 96.2-3 (2009), 251–256. ISSN: 0946-2171. DOI: 10.1007/s00340-009-3374-6.

[17] Chih-Hao Li et al. "A laser frequency comb that enables radial velocity measurements with a precision of 1 cm s(-1)". In: *NATURE* 452.7187 (2008), 610–612. ISSN: 0028-0836. DOI: 10.1038/nature06854.

[18] D. A. Braje et al. "Astronomical spectrograph calibration with broad-spectrum frequency combs". In: *EUROPEAN PHYSICAL JOURNAL D* 48.1 (2008), 57–66. ISSN: 1434-6060. DOI: 10.1140/epjd/e2008-00099-9.

[19] Tilo Steinmetz et al. "Laser frequency combs for astronomical observations". In: *SCIENCE* 321.5894 (2008), 1335–1337. ISSN: 0036-8075. DOI: 10.1126/science.1161030.

[20] S. A. Diddams et al. "Improved signal-to-noise ratio of 10 GHz microwave signals generated with a mode-filtered femtosecond laser frequency comb". In: *OPTICS EXPRESS* 17.5 (2009), 3331–3340. ISSN: 1094-4087. DOI: 10.1364/OE.17.003331.

[21] G ALZETTA et al. "EXPERIMENTAL-METHOD FOR OBSERVATION OF RF TRANSITIONS AND LASER BEAT RESONANCES IN ORIENTED NA VAPOR". In: *NUOVO CIMENTO DELLA SOCIETA ITALIANA DI FISICA B-GENERAL PHYSICS RELATIVITY ASTRONOMY AND MATHEMATICAL PHYSICS AND METHODS* 36.1 (1976), 5–20. ISSN: 0369-3554. DOI: 10.1007/BF02749417.

[22] A ASPECT et al. "LASER COOLING BELOW THE ONE-PHOTON RECOIL ENERGY BY VELOCITY-SELECTIVE COHERENT POPULATION TRAPPING". English. In: *PHYSICAL REVIEW LETTERS* 61.7 (1988), 826–829. ISSN: 0031-9007. DOI: 10.1103/PhysRevLett.61.826.

[23] G Morigi, J Eschner, and CH Keitel. "Ground state laser cooling using electromagnetically induced transparency". In: *PHYSICAL REVIEW LETTERS* 85.21 (2000), 4458–4461. ISSN: 0031-9007. DOI: 10.1103/PhysRevLett.85.4458.

[24] D. T. C. Allcock et al. "Dark-resonance Doppler cooling and high fluorescence in trapped Ca-43 ions at intermediate magnetic field". In: *NEW JOURNAL OF PHYSICS* 18 (2016). ISSN: 1367-2630. DOI: 10.1088/1367-2630/18/2/023043.

[25] CF Roos et al. "Experimental demonstration of ground state laser cooling with electromagnetically induced transparency". In: *PHYSICAL REVIEW LETTERS* 85.26, 1 (2000), 5547–5550. ISSN: 0031-9007. DOI: 10.1103/PhysRevLett.85.5547.

[26] C Lisowski et al. "Dark resonances as a probe for the motional state of a single ion". In: *APPLIED PHYSICS B-LASERS AND OPTICS* 81.1 (2005), 5–12. ISSN: 0946-2171. DOI: 10.1007/s00340-005-1867-5.

[27] J. Rossnagel et al. "Fast thermometry for trapped ions using dark resonances". In: *NEW JOURNAL OF PHYSICS* 17 (2015). ISSN: 1367-2630. DOI: 10.1088/1367-2630/17/4/045004.

[28] Thorsten Peters et al. "Thermometry of ultracold atoms by electromagnetically induced transparency". In: *PHYSICAL REVIEW A* 85.6 (2012). ISSN: 1050-2947. DOI: 10.1103/PhysRevA.85.063416.

[29] T Udem, R Holzwarth, and TW Hansch. "Optical frequency metrology". In: *NATURE* 416.6877 (2002), 233–237. ISSN: 0028-0836. DOI: 10.1038/416233a.

[30] J Reichert et al. "Phase coherent vacuum-ultraviolet to radio frequency comparison with a mode-locked laser". In: *PHYSICAL REVIEW LETTERS* 84.15 (2000), 3232–3235. ISSN: 0031-9007. DOI: 10.1103/PhysRevLett.84.3232.

[31] SA Diddams et al. "Direct link between microwave and optical frequencies with a 300 THz femtosecond laser comb". In: *PHYSICAL REVIEW LETTERS* 84.22 (2000), 5102–5105. ISSN: 0031-9007. DOI: 10.1103/PhysRevLett.84.5102.

[32] H Schnatz et al. "First phase-coherent frequency measurement of visible radiation". In: *PHYSICAL REVIEW LETTERS* 76.1 (1996), 18–21. ISSN: 0031-9007. DOI: 10.1103/PhysRevLett.76.18.

[33] Seung-Woo Kim. "Combs rule". English. In: *NATURE PHOTONICS* 3.6 (2009), 313–314. ISSN: 1749-4885. DOI: 10.1038/nphoton.2009.86.

[34] R Holzwarth et al. "Optical frequency synthesizer for precision spectroscopy". In: *PHYSICAL REVIEW LETTERS* 85.11 (2000), 2264–2267. ISSN: 0031-9007. DOI: 10.1103/PhysRevLett.85.2264.

[35] M Hentschel et al. "Attosecond metrology". In: *NATURE* 414.6863 (2001), 509–513. ISSN: 0028-0836. DOI: 10.1038/35107000.

[36] A Baltuska et al. "Attosecond control of electronic processes by intense light fields". In: *NATURE* 421.6923 (2003), 611–615. ISSN: 0028-0836. DOI: 10.1038/nature01414.

[37] Adam Lesundak et al. "THE FEMTOSECOND OPTICAL FREQUENCY COMB BASED TOOL FOR SPECTRAL ANALYSIS OF MOLECULAR ABSORBTION GASES". In: *NANOCON 2012, 4TH INTERNATIONAL CONFERENCE*. 4th International Conference on NANOCON, Brno, CZECH REPUBLIC, OCT 23-25, 2012. Tanger Ltd; Czech Soc New Mat & Technologies; Reg Ctr Adv Technologies & Mat; Mat Res Soc Serbia; Norsk Materialteknisk Selskap. 2012, 836–841. ISBN: 978-80-87294-35-2.

[38] Christoph Gohle et al. "Frequency comb vernier spectroscopy for broadband, high-resolution, high-sensitivity absorption and dispersion spectra". In: *PHYSICAL REVIEW LETTERS* 99.26 (2007). ISSN: 0031-9007. DOI: 10.1103/PhysRevLett.99.263902.

[39] ST Cundiff and J Ye. "Colloquium: Femtosecond optical frequency combs". In: *REVIEWS OF MODERN PHYSICS* 75.1 (2003), 325–342. ISSN: 0034-6861. DOI: 10.1103/RevModPhys.75.325.

[40] *Optical Frequency Combs PDF document*. https://www.menlosystems.com/assets/documents-2/Optical-Frequency-Combs.pdf. Accessed: 2019-04-20.

[41] DJ Jones et al. "Carrier-envelope phase control of femtosecond mode-locked lasers and direct optical frequency synthesis". In: *SCIENCE* 288.5466 (2000), 635–639. ISSN: 0036-8075. DOI: 10.1126/science.288.5466.635.

[42] HR Telle et al. "Carrier-envelope offset phase control: A novel concept for absolute optical frequency measurement and ultrashort pulse generation". In: *APPLIED PHYSICS B-LASERS AND OPTICS* 69.4 (1999), 327–332. ISSN: 0946-2171. DOI: 10.1007/s003400050813.

[43] P Russell. "Photonic crystal fibers". In: *SCIENCE* 299.5605 (2003), 358–362. ISSN: 0036-8075. DOI: 10.1126/science.1079280.

[44] JK Ranka, RS Windeler, and AJ Stentz. "Visible continuum generation in air-silica microstructure optical fibers with anomalous dispersion at 800 nm". In: *OPTICS LETTERS* 25.1 (2000), 25–27. ISSN: 0146-9592. DOI: 10.1364/OL.25.000025.

[45] Parama Pal and Wayne H. Knox. "Self referenced Yb-fiber-laser frequency comb using a dispersion micromanaged tapered holey fiber". In: *OPTICS EXPRESS* 15.19 (2007), 12161–12166. ISSN: 1094-4087. DOI: 10.1364/OE.15.012161.

[46] BR Washburn et al. "Phase-locked, erbium-fiber-laser-based frequency comb in the near infrared". In: *OPTICS LETTERS* 29.3 (2004), 250–252. ISSN: 0146-9592. DOI: 10.1364/OL.29.000250.

[47] F SALIN, J SQUIER, and M PICHE. "MODE-LOCKING OF TI-AL2O3 LASERS AND SELF-FOCUSING - A GAUSSIAN APPROXIMATION". In: *OPTICS LETTERS* 16.21 (1991), 1674–1676. ISSN: 0146-9592. DOI: 10.1364/OL.16.001674.

[48] R SZIPOCS et al. "CHIRPED MULTILAYER COATINGS FOR BROAD-BAND DISPERSION CONTROL IN FEMTOSECOND LASERS". In: *OPTICS LETTERS* 19.3 (1994), 201–203. ISSN: 0146-9592. DOI: 10.1364/OL.19.000201.

[49] T BRABEC et al. "KERR LENS MODE-LOCKING". In: *OPTICS LETTERS* 17.18 (1992), 1292–1294. ISSN: 0146-9592. DOI: 10.1364/OL.17.001292.

[50] FX KARTNER and U KELLER. "STABILIZATION OF SOLITON-LIKE PULSES WITH A SLOW SATURABLE ABSORBER". In: *OPTICS LETTERS* 20.1 (1995), 16–18. ISSN: 0146-9592.

[51] K TAMURA et al. "SOLITON VERSUS NONSOLITON OPERATION OF FIBER RING LASERS". In: *APPLIED PHYSICS LETTERS* 64.2 (1994), 149–151. ISSN: 0003-6951. DOI: 10.1063/1.111547.

[52] LE Nelson et al. "Ultrashort-pulse fiber ring lasers". In: *APPLIED PHYSICS B-LASERS AND OPTICS* 65.2 (1997), 277–294. ISSN: 0946-2171. DOI: 10.1007/s003400050273.

[53] B. P. Abbott et al. "Observation of Gravitational Waves from a Binary Black Hole Merger". In: *PHYSICAL REVIEW LETTERS* 116.6 (2016). ISSN: 0031-9007. DOI: 10.1103/PhysRevLett.116.061102.

[54] R DANDLIKER, R THALMANN, and D PRONGUE. "2-WAVELENGTH LASER INTERFEROMETRY USING SUPERHETERODYNE DETECTION". English. In: *OPTICS LETTERS* 13.5 (1988), 339–341. ISSN: 0146-9592. DOI: 10.1364/OL.13.000339.

[55] R DANDLIKER et al. "HIGH-ACCURACY DISTANCE MEASUREMENTS WITH MULTIPLE-WAVELENGTH INTERFEROMETRY". In: *OPTICAL ENGINEERING* 34.8 (1995), 2407–2412. ISSN: 0091-3286.

[56] Adam Lesundak et al. "High-accuracy long distance measurements with a mode-filtered frequency comb". English. In: *OPTICS EXPRESS* 25.26 (2017), 32570–32580. ISSN: 1094-4087. DOI: 10.1364/OE.25.032570.

[57] Eugene Hecht. *Optics*. 4th ed. 1301 Samsone St., San Francisco, CA 94111: Addison Wesley, 2002. ISBN: 0-8053-8566-5.

[58] M Shirasaki. "Large angular dispersion by a virtually imaged phased array and its application to a wavelength demultiplexer". English. In: *OPTICS LETTERS* 21.5 (1996), 366–368. ISSN: 0146-9592. DOI: 10.1364/OL.21.000366.

[59] SJ Xiao and AM Weiner. "2-D wavelength demultiplexer with potential for >= 1000 channels in the C-band". In: *OPTICS EXPRESS* 12.13 (2004), 2895–2902. ISSN: 1094-4087. DOI: 10.1364/OPEX.12.002895.

[60] SJ Xiao, AM Weiner, and C Lin. "A dispersion law for virtually imaged phased-array spectral dispersers based on paraxial wave theory". In: *IEEE JOURNAL OF QUANTUM ELECTRONICS* 40.4 (2004), 420–426. ISSN: 0018-9197. DOI: 10.1109/JQE.2004.825210.

[61] A Vega, AM Weiner, and C Lin. "Generalized grating equation for virtually-imaged phased-array spectral dispersers". In: *APPLIED OPTICS* 42.20 (2003), 4152–4155. ISSN: 1559-128X. DOI: 10.1364/AO.42.004152.

[62] David Balslev-Clausen. "Broad band cavity enhanced direct frequency comb spectroscopy". MA thesis. University of Colorado, 2007.

[63] Andreas Hansel. "Applications of spectroscopy with multiwavelength sources". PhD thesis. TU Delft, 2018.

[64] Michael J. Thorpel. "Cavity-enhanced direct frequency combspectroscopy". PhD thesis. University of Colorado, 2009.

[65] Adam Lesundak et al. "Repetition rate multiplication of a femtosecond frequency comb". In: *PHOTONICS, DEVICES, AND SYSTEMS VI*. Ed. by Tomanek, P and Senderakova, D and Pata, P. Vol. 9450. Proceedings of SPIE. 8th International Conference on Photonics, Devices, and System VI, Prague, CZECH REPUBLIC, AUG 27-29, 2014. Czech & Slovak Soc Photon; Act M Agcy. 2015. ISBN: 978-1-62841-566-7. DOI: 10.1117/12.2074415.

[66] T. J. Hammond, Arthur K. Mills, and David J. Jones. "Simple method to determine dispersion of high-finesse optical cavities". In: *OPTICS EXPRESS* 17.11 (2009), 8998–9005. ISSN: 1094-4087. DOI: 10.1364/OE.17.008998.

[67] Anthony E. Siegman. *Lasers*. Susalito, California: Univesity Science Books, 1986. ISBN: 0-935702-11-3.

[68] KP BIRCH and MJ DOWNS. "AN UPDATED EDLEN EQUATION FOR THE REFRACTIVE-INDEX OF AIR". In: *METROLOGIA* 30.3 (1993), 155–162. ISSN: 0026-1394. DOI: 10.1088/0026-1394/30/3/004.

[69] Joohyung Lee, Seung-Woo Kim, and Young-Jin Kim. "Repetition rate multiplication of femtosecond light pulses using a phase-locked all-pass fiber resonator". In: *OPTICS EXPRESS* 23.8 (2015), 10117–10125. ISSN: 1094-4087. DOI: 10.1364/OE.23.010117.

[70] Miguel A. Preciado and Miguel A. Muriel. "Repetition-rate multiplication using a single all-pass optical cavity". English. In: *OPTICS LETTERS* 33.9 (2008), 962–964. ISSN: 0146-9592. DOI: 10.1364/OL.33.000962.

[71] A. Haboucha et al. “Optical-fiber pulse rate multiplier for ultralow phase-noise signal generation”. English. In: *OPTICS LETTERS* 36.18 (2011), 3654–3656. ISSN: 0146-9592. DOI: 10.1364/OL.36.003654.

[72] Yoshiaki Nakajima, Akiko Nishiyama, and Kaoru Minoshima. “Mode-filtering technique based on all-fiber-based external cavity for fiber-based optical frequency comb”. In: *OPTICS EXPRESS* 26.4 (2018), 4656–4664. ISSN: 1094-4087. DOI: 10.1364/OE.26.004656.

[73] ST Cundiff, J Ye, and JL Hall. “Optical frequency synthesis based on mode-locked lasers”. English. In: *REVIEW OF SCIENTIFIC INSTRUMENTS* 72.10 (2001), 3749–3771. ISSN: 0034-6748. DOI: 10.1063/1.1400144.

[74] J JIN and DA CHURCH. “PRECISION LIFETIMES FOR THE CA+ 4P 2P LEVELS - EXPERIMENT CHALLENGES THEORY AT THE 1-PERCENT LEVEL”. In: *PHYSICAL REVIEW LETTERS* 70.21 (1993), 3213–3216. ISSN: 0031-9007. DOI: 10.1103/PhysRevLett.70.3213.

[75] Christoph Raab. “Interference experiments with the fluorescence light of Ba+ ions”. PhD thesis. University of Innsbruck, 2001.

[76] M.O. Scully and M.S. Zubairy. *Quantum optics*. Cambridge University Press, 1997.

[77] C. Cohen-Tannoudji. *Frontiers in Laser spectroscopy*. Les Houches 1975, 1977.

[78] Hilmar Oberst. “Resonance fluorescence of single Barium ions”. MA thesis. University of Innsbruck, 1999.

[79] Daniel Vadlejch. “Výpočet průběhu potenciálů a simulace chování iontů vápníku v Paulově elektrické pasti”. MA thesis. VUT BRNO, 2018.

[80] Christian Felix Roos. “Controlling the quantum state of trapped ions”. PhD thesis. University of Innsbruck, 2000.

[81] R. Gerritsma et al. “Precision measurement of the branching fractions of the 4p P-2(3/2) decay of Ca II”. In: *EUROPEAN PHYSICAL JOURNAL D* 50.1 (2008), 13–19. ISSN: 1434-6060. DOI: 10.1140/epjd/e2008-00196-9.

[82] Michael Guggemos. “Precision spectroscopy with trapped $^{40}Ca^{+}$ and $^{27}Al^{+}$ ions”. PhD thesis. University of Innsbruck, 2017.

[83] Adam Lesundak et al. “Single trapped ion fluorescence response to frequency modualtion of dark state popupation”. to be submitted. 2019.

[84] *Exact signal measurements using FFT analysis*. https://kluedo.ub.uni-kl.de/frontdoor/deliver/index/docId/4293/file/exact_fft_measurements.pdf. Accessed: 2019-04-20.

[85] JR Carson. “Notes on the theory of modulation”. English. In: *PROCEEDINGS OF THE INSTITUTE OF RADIO ENGINEERS* 10.1 (1922), 57–64. ISSN: 0731-5996. DOI: 10.1109/JRPROC.1922.219793.

[86] RJ Pieper. “Laboratory and computer tests for Carson’s FM bandwidth rule”. In: *PROCEEDINGS OF THE 33RD SOUTHEASTERN SYMPOSIUM ON SYSTEM THEORY*. PROCEEDINGS - SOUTHEASTERN SYMPOSIUM ON SYSTEM THEORY. 33rd Southeastern Symposium on System Theory, OHIO UNIV, ATHENS, OH, MAR 18-20, 2001. Russ Coll Engn & Technol; Sch Elect Engn & Comp Sci; IEEE Control Soc; IEEE. 2001, 145–149. ISBN: 0-7803-6661-1. DOI: 10.1109/SSST.2001.918507.